Simulation numérique des interactions fluide-structure dans une fistule artério-veineuse sténosée et des effets de traitements endovasculaires

Iolanda Decorato

▶ To cite this version:

Iolanda Decorato. Simulation numérique des interactions fluide-structure dans une fistule artério-veineuse sténosée et des effets de traitements endovasculaires. Médecine humaine et pathologie. Université de Technologie de Compiègne, 2013. Français. NNT : 2013COMP2061 . tel-00832342

HAL Id: tel-00832342
https://theses.hal.science/tel-00832342v1

Submitted on 10 Jun 2013

Par **Iolanda DECORATO**

Simulation numérique des interactions fluide-structure dans une fistule artério-veineuse sténosée et des effets de traitements endovasculaires

Thèse présentée
pour l'obtention du grade
de Docteur de l'UTC

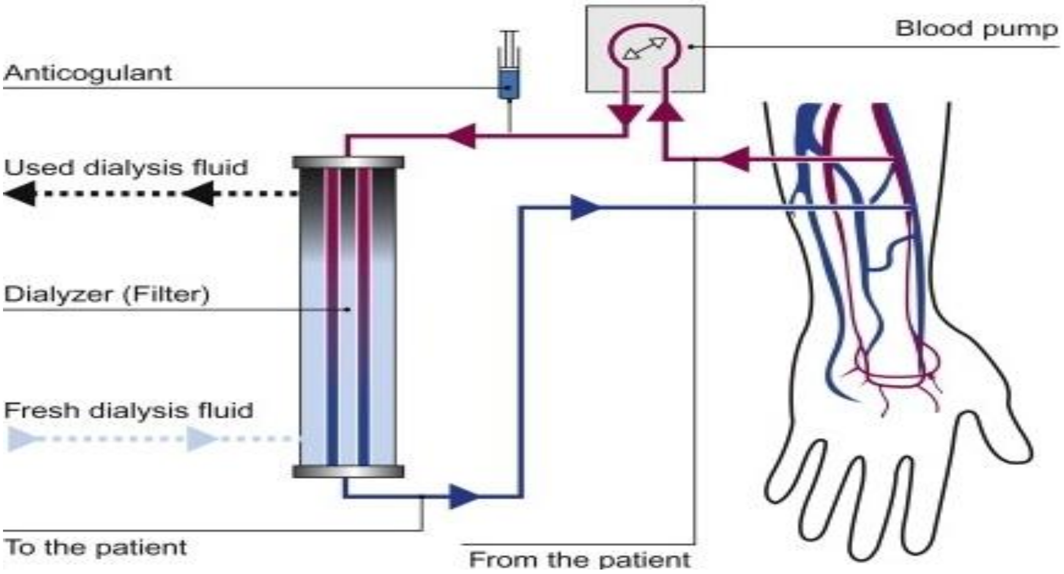

Soutenue le 05 février 2013
Spécialité : Bio-ingénierie, Biomécanique, Biomatériaux

D2061

Université de Technologie de Compiègne

THESE DE DOCTORAT

Intitulée

Simulation numérique des interactions fluide-structure dans une fistule artério-veineuse sténosée et des effets de traitements endovasculaires.

Présentée par

Iolanda DECORATO

Pour l'obtention du grade de
Docteur de l'Université de Technologie de Compiègne
Spécialité : Bio-Ingénierie Biomécanique Biomatériaux

Soutenue le 5 février 2013 devant le jury composé par

Rapporteur	Prof. Frans Van de VOSSE	Eindhoven University of Technology
Rapporteur	Prof. Stéphane AVRIL	Ecole Nationale Supérieure des Mines de St Etienne
Examinateur	Prof. Thierry PETITCLERC	Association pour l'Utilisation du Rein Artificiel, Paris
Examinateur	Dr. Cécile LEGALLAIS	Université de Technologie de Compiègne
co-Directeur	Dr. Anne-Virginie SALSAC	Université de Technologie de Compiègne
co-Directeur	Dr. Zaher KHARBOUTLY	Université de Technologie de Compiègne

To Michele
To my sister Sissi
To my parents

Acknowledgements:

A PhD thesis is a long walk, along non-traced paths, that a graduate student starts with his supervisor. I wont firstly to acknowledge Anne-Virginie Salsac, Zaher Kharboutly and Cécile Legallais: they have given me the possibility to start this way, despite I didn't know french language. Their advice during the PhD has been precious, and it has been my pleasure to work together. But Anne-Virginie deserves a special acknowledgment. She has been at each moment at my side, listening to my problems and ideas even late in the night, telling me once we finished "...mais tout cela attendra demain, rentre et passe une bonne soirée". Thank you to show me how to do my best without 'overdo'. Thank you, Anne-Virginie, also for the confidence you had in me when you decided to involve me in the supervision of Tommaso, this experience has made me improve different skills.

Thank you to the members of the jury, for the time you dedicated in reading the manuscript and for the advice you gave me to improve the definitive version.

Thank you as well to people who have help me in managing 'bureaucracy': I'm still suspicious of missions, invoices, and similar.

I also want to say thank you to all the people that have been in the 'Laboratoire de Biomécanique et Bioengénierie' during these three years. Thank you for the moment of pleasure we spent together at lunch time. Thank you for the advice and questions you gave and asked me when I had to present my work. And in particular thank you, Claire, to share all that with me. Thank you to be my friend, we have spent wonderful days together all over France, and I sincerely hope to show you how wonderful is Italy.

A sincere thank you to all people that have been part of my everyday life during the last three years. You have made me feel at home. You gave me a reason to be strong in bad days, and you have been always ready

to celebrate good days. You introduced me to french culture, and I am grateful for that.

Thank you to the European Union, founding the project, but particularly thank you to all people of the 'MeDDiCa board': your passion gave you a reason to build up this project, and I hope you can do it again in future. And how to forget the other students of the project MeDDiCa, all over Europe: Daria, Ben, Iwona, Claudia, Selim, Hannan, GuangLei, Li Yan, Santosh, Carlos, Rajeev, Brandis and Selim.

Thank you to all the friends that I have in Italy and who are waiting for me. Thank you to all the friends from Italy who are spending their life abroad, I hope to come to see you soon.

Thank you to my parents and my sister, who trust in me, whatever happens. Thank you to be happy when I am, and to show me how life is beautiful when I am not.

And, last but not least, thank you Michele. Thank you because you said me to go in Compiègne, because you thought it was important for me. Thank you to have spent your days here each time you had the opportunity. Thank you to have become, with me, the principal foundation for easyjet. Thank you to be with me.

Introduction générale:

Une fistule artérioveineuse (FAV) est un accès vasculaire permanent créé par voie chirurgicale en connectant une veine et une artère chez le patient en hémodialyse. Cet accès vasculaire permet de mettre en place une circulation extracorporelle partielle afin de remplacer les fonctions exocrines des reins. En France, environ 36000 patients sont atteint d'insuffisance rénale chronique en phase terminale, stade de la maladie le plus grave qui nécessite la mise en place d'un traitement de suppléance des reins : l'hémodialyse.

La création et présence de la FAV modifient significativement l'hémodynamique dans les vaisseaux sanguins, au niveau local et systémique ainsi qu'à court et à plus long terme. Ces modifications de l'hémodynamiques peuvent induire différents pathologies vasculaires, comme la formation d'anévrysmes et de sténoses. L'objectif de cette étude est de mieux comprendre le comportement mécanique et l'hémodynamique dans les vaisseaux de la FAV.

Nous avons étudié numériquement les interactions fluide-structure (IFS) au sein d'une FAV patient-spécifique, dont la géométrie a été reconstruite à partir d'images médicales acquises lors d'un précédent doctorat. Cette FAV a été créée chez le patient en connectant la veine céphalique du patient à l'artère radiale et présente une sténose artérielle réduisant de 80% la lumière du vaisseau. Nous avons imposé le profil de vitesse mesuré sur le patient comme conditions aux limites en entrée et un modèle de Windkessel au niveau des sorties artérielle et veineuse. Nous avons considéré des propriétés mécaniques différentes pour l'artère et la veine et pris en compte le comportement non-Newtonien du sang. Les simulations IFS permettent de calculer l'évolution temporelle des contraintes hémodynamiques et des contraintes internes à la paroi des vaisseaux. Nous nous sommes demandé aussi si des simulations non couplées des équations fluides et solides permettaient d'obtenir des résultats suffisamment précis tout en réduisant sig-

nificativement le temps de calcul, afin d'envisager son utilisation par les chirurgiens.

Dans la deuxième partie de l'étude, nous nous sommes intéressés à l'effet de la présence d'une sténose artérielle sur l'hémodynamique et en particulier à ses traitements endovasculaires. Nous avons dans un premier temps simulé numériquement le traitement de la sténose par angioplastie. En clinique, les sténoses résiduelles après angioplastie sont considérées comme acceptables si elles obstruent moins de 30% de la lumière du vaisseau. Nous avons donc gonflé le ballonnet pour angioplastie avec différentes pressions de manière à obtenir des degrés de sténoses résiduelles compris entre 0 et 30%.

Une autre possibilité pour traiter la sténose est de placer un stent après l'angioplastie. Nous avons donc dans un deuxième temps simulé ce traitement numériquement et résolu le problème d'IFS dans la fistule après la pose du stent. Dans ces simulations, la présence du stent a été prise en compte en imposant les propriétés mécaniques équivalentes du vaisseau après la pose du stent à une portion de l'artère.

Dans la dernière partie de l'étude nous avons mis en place un dispositif de mesure par PIV (Particle Image Velocimetry). Un moule rigide et transparent de la géométrie a été obtenu par prototypage rapide. Les résultats expérimentales ont été validés par comparaison avec les résultats des simulations numériques.

Mots clés:

Fistule artérioveineuse
Compliance vasculaire
Simulation des interaction fluide-structure
Sténose artérielle
Angioplastie par ballonnet
Positionnement d'un stent

Summary:

An arteriovenous fistula (AVF) is a permanent vascular access created surgically connecting a vein onto an artery. It enables to circulate blood extra-corporeally in order to clean it from metabolic waste products and excess of water for patients with end-stage renal disease undergoing hemodialysis. The hemodynamics results to be significantly altered within the arteriovenous fistula compared to the physiological situation. Several studies have been carried out in order to better understand the consequences of AVF creation, maturation and frequent use, but many clinical questions still lie unanswered. The aim of the present study is to better understand the hemodynamics within the AVF, when the compliance of the vascular wall is taken into account. We also propose to quantify the effect of a stenosis at the afferent artery, the incidence of which has been underestimated for many years.

The fluid-structure interactions (FSI) within a patient-specific radio-cephalic arteriovenous fistula are investigated numerically. The considered AVF presents an 80% stenosis at the afferent artery. The patient-specific velocity profile is imposed at the boundary inlet, and a Windkessel model is set at the arterial and venous outlets. The mechanical properties of the vein and the artery are differentiated. The non-Newtonian blood behavior has been taken into account. The FSI simulation advantageously provides the time-evolution of both the hemodynamic and structural stresses, and guarantees the equilibrium of the solution at the interface between the fluid and solid domains. The FSI results show the presence of large zones of blood flow recirculation within the cephalic vein, which might promote neointima formation. Large internal stresses are also observed at the venous wall, which may lead to wall remodeling.

The fully-coupled FSI simulation results to be costly in computational time, which can so far limit its clinical use. We have investigated whether uncoupled fluid and structure simulations can provide accurate results and

significantly reduce the computational time. The uncoupled simulations have the advantage to run 5 times faster than the fully-coupled FSI. We show that an uncoupled fluid simulation provides informative qualitative maps of the hemodynamic conditions in the AVF. Quantitatively, the maximum error on the hemodynamic parameters is 20%. The uncoupled structural simulation with non-uniform wall properties along the vasculature provides the accurate distribution of internal wall stresses, but only at one instant of time within the cardiac cycle. Although partially inaccurate or incomplete, the results of the uncoupled simulations could still be informative enough to guide clinicians in their decision-making.

In the second part of the study we have investigated the effects of the arterial stenosis on the hemodynamics, and simulated its treatment by balloon-angioplasty. Clinically, balloon-angioplasty rarely corrects the stenosis fully and a degree of stenosis remains after treatment. Residual degrees of stenosis below 30% are considered as successful. We have inflated the balloon with different pressures to simulate residual stenoses ranging from 0 to 30%. The arterial stenosis has little impact on the blood flow distribution: the venous flow rate remains unchanged before and after the treatment and thus permits hemodialysis. But an increase in the pressure difference across the stenosis is observed, which could cause the heart work load to increase. To guarantee a pressure drop below 5 mmHg, which is considered as the threshold stenosis pressure difference clinically, we find that the residual stenosis degree must be 20% maximum.

To correct arterial stenoses, another option is to place a stent after angioplasty. We have simulated the procedure of balloon-angioplasty with stenting numerically and solved for the fluid-structure interactions within the stented vessel. In the FSI simulation, we have accounted for the presence of the stent by imposing previously evaluated equivalent mechanical properties to the stented portion of the artery. Comparing the hemodynamic and structural stresses with the case of balloon-angioplasty alone, we have found no significant differences between the two treatments, except for the larger wall internal stresses observed locally at the stent loca-

tion. Still stenting has been shown to improve the patient's patency. One can therefore conclude that the stent has a favorable action in the long run by pertaining the vessel opening.

Keywords:

Arteriovenous fistula
Wall compliance
Fluid-structure interaction simulation
Arterial stenosis
Balloon-angioplasty
Stent positioning

Contents

Nomenclature

Latin symbols

A	Cross-sectional area of the vessel.
C	Equivalent compliance of the outflow vasculature.
C_{10}, C_{20}, C_{30}	Material constants of the 3^{rd}-order Yeoh model.
CFD	Computational Fluid Dynamics.
D_{eq}	Diameter of the disk with the same cross-section area of the vessel.
D_1, D_2, D_3	Incompressibility parameters of the 3^{rd}-order Yeoh model.
E	Young modulus.
E_{eq}	Equivalent Young modulus of the stented artery.
FSI	Fluid-Structure Interactions.
I_1	Deviatoric first principal strain invariant.
J	Jacobian (equal to 1 when the material is incompressible).
LDV	Laser Doppler Velocimetry.
MRV	Magnetic Resonance Velocimetry.
$\mathbf{n}$	Unit vector normal to the vascular wall.
OSI	Oscillatory shear index.
P	Blood pressure.
PI	Pulsatility index.
PIV	Particle Image Velocimetry.
Q	Blood flow rate.

R	Equivalent resistance of the outflow vasculature.
R_D	Displacement correlation peak of the cross correlation algorithm.
T	Time period of the cardiac cycle.
t_1, t_2	Time instant at which images 1 and 2 are taken during PIV.
t_{comp}	Computational time.
$\mathbf{v}$	Velocity vector.
v_s, v_d	Peak systolic and late diastolic velocity.
WSS	Modulus of τ_w.
$WSSG_t$	Temporal gradient of WSS.

Greek symbols

$\dot{\gamma}$	Blood shear rate.
Δl_{max}	Maximum mesh length.
ΔP	Pressure drop at the stenosis.
Δt	Time interval between t_1 and t_2.
κ	Consistency parameter in the non-Newtonian Casson model.
μ	Apparent dynamic viscosity of blood.
ρ	Density of the material.
σ_i $(i = 1, 2, 3)$	Principal components of the Cauchy stress tensor.
$\overline{\sigma}_{max}$	Time-averaged value of the maximum component of the Cauchy stress tensor.
τ_0	Yield stress in the non-Newtonian Casson model.
τ_w	Viscous stress acting tangentially to the vessel wall.

Chapter 1

Introduction

The kidneys are in charge of eliminating toxic metabolic products and excess of water from blood, as well as ensuring electrolyte and buffer balance. When these functions are altered, the kidneys cannot provide their exocrine functions, and metabolic waste products accumulate in the patient's tissues. Renal disease can either be acute or chronic. When acute the renal function needs to be supplied temporarily; if chronic the patient kidneys degenerate progressively and the only curing option is a renal transplantation.

Because of the lack of donors, two main techniques have been developed to supply the detoxification function of kidneys: peritoneal dialysis and hemodialysis. Both dialysis techniques use mass exchange across a membrane between blood and an artificial fluid, the dialysate, to filter waste products from blood, restore its physiological composition and remove the excess of water. They differ by the type of membrane used as filter. In the case of peritoneal dialysis, filtering occurs through the peritoneum, the membrane that envelops the intestine. The peritoneum is a tissue highly vascularized by capillaries for the portal system. Hemodialysis relies instead on an artificial membrane, whose structure and surface are designed to optimize mass exchanges. It is placed inside an external device called dialyzer or artificial kidney and separates two compartments. The patient blood is directed towards the lumen compartment of the dialyzer by an extra-corporeal circulation loop. At the same time the dialysate flows through the outer compartment in counter-current.

The remaining part of the chapter is focused on hemodialysis, which is the treatment option chosen in 85% of patients with chronic kidneys disease [1]. The objective is to review in particular what has been understood on the hemodynamics within the vascular access created to enable the partial extracorporeal circulation from the patient to the dialysis machine. We will summarize what is known on the treatment by hemodialysis and the evolution of the hemodynamics after the creation of the AVF. We will review potential flow-related complications and their treatment and see how in vitro and in silico models have contributed to the investigation of the hemodynamic consequences.

1 Hemodialysis

The principle of hemodialysis involves the diffusion and convection of solutes and water across a semi-permeable membrane. A schematic of the hemodialysis machine and constituents is shown in figure 1.1.

A membrane or dialysis filter separates blood from the dialysate fluid. The transfer of substances from blood to the dialysate is driven by concentration and pressure gradients. The dialysate has the physiological concentration in electrolytes to prevent unexpected removal from blood. The two fluids flow in counter-current, which optimizes mass transfer. The excess of water is removed from blood by adjusting the transmembrane pressure between blood and dialysate [2].

The hemodialysis treatment is adapted to each patient. The nephrologist decides on the frequency of hemodialysis sessions, their duration, the flow rate to be set for the blood and dialysate flows and the dialyzer size. The composition of the dialysate solution may also be adjusted in terms of its ionic and bicarbonate concentrations.

In general, three sessions are prescribed per week. Two weekly sessions are restricted to patients who have substantial residual kidney functions. Four weekly sessions are often prescribed in the case of overweight patients, since the larger the patient body size the longer the dialysis needs

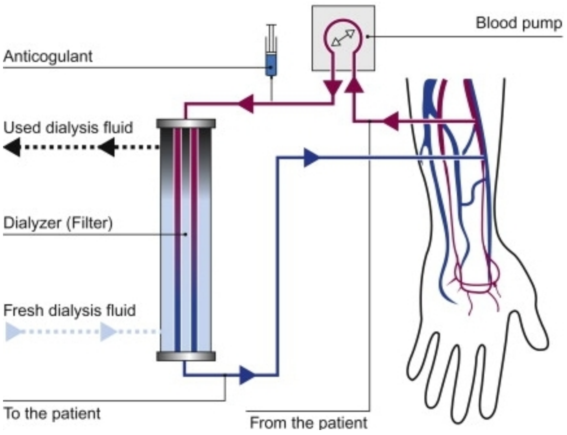

Figure 1.1: Schematic of the hemodialysis machine when connected to the patient [3].

to be. It is also used for patients with fluid overload. There is otherwise a growing interest in nocturnal dialysis, which consists in dialyzing a patient at night if possible at home. Three to six sessions of 8-10 hours are then required per week. Nocturnal in-center dialysis is offered at a handful of units in the United States.

2 Vascular accesses

A permanent vascular access is needed in chronic end-stage renal disease patients in order to treat blood extra-corporeally. Since the artificial membrane has an optimal exchange rate for blood flows larger than 250-300 ml.min^{-1}, the vascular access needs to provide a flow rate of at least 500 ml.min^{-1}. It needs to be easily accessible and able to bear frequent puncture. Such an access does not exist in the human body and needs to be created surgically. Permanent access can rely on a central venous catheter (CVC), an arteriovenous graft (AVG) or a native arteriovenous fistula (AVF).

2.1 Central venous catheter

The central venous catheter (CVC) access consists in the insertion of a two-lumen catheter inside a large vein (vena cava, jugular vein or femoral vein) as shown in figure 1.2. It is usually adopted when a rapid, sudden access to the patient vasculature is required. One such instance occurs in the case of acute renal failure, usually after an intoxication or an infection. The CVC can in some cases be the only viable option, when the vasculature of the patient is too degraded for the creation of an arteriovenous connection.

However CVCs are not systematically used because of the high risk of complications and bad tolerance by the patient [4]. In clinics it is preferred to use different access types: the arteriovenous graft or the arteriovenous fistula [5].

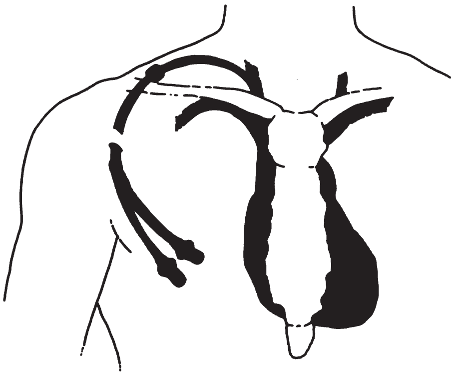

Figure 1.2: Schematic of a central venous catheter as access for hemodialysis [6].

2.2 Arteriovenous graft

An arteriovenous graft is created by connecting the arterial tree to the venous one with a conduct (graft) of appropriate caliber made in an artificial or biological material (figure 1.3). The suture of the graft onto the artery is called anastomosis. Synthetic grafts are usually in polytetrafluoroethylene (PTFE) or silicone. Biological grafts can either be made of one of the patient's vessel (i.e. an homologous vein), from a bovine or sheep vessel or from tissue engineering. Grafts entirely made with patient cells have recently been developed (Cytograft Tissue Engineering(1)) and are in clinical tests. Preliminary results on patients having a high risk of graft failure show a primary patency of 76% at 1 month after implantation and of 50% at 6 months [7].

---

(1) `http://www.cytograft.com/learn.html`

AVG have a high risk of aneurysm formation with an occurrence rate around 70-80% during the first year after creation [8]. Moreover, they present a large risk of stenosis and thrombosis occurrence [9]. Therefore grafts are used primarily when the quality of the native vessels is too poor. In Europe they are used in less than 10% of the patients [10]. Their main advantage is to be immediately available for puncture and to necessitate a relatively easy surgical procedure to be implanted. This explains why AVG are created in around 80% of the patients in the United States [11].

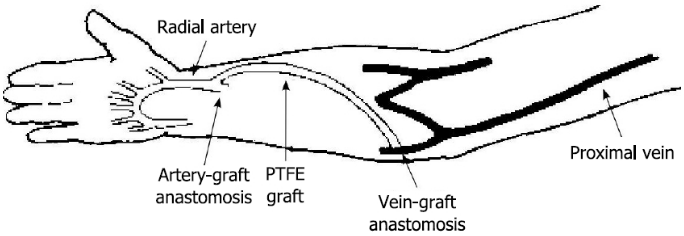

Figure 1.3: Schematic of an arteriovenous graft connecting an artery and a vein (modified from [12]).

2.3 Autologous arteriovenous fistula

An autologous AVF is created by connecting an artery and a vein directly onto one another bypassing the peripheral capillary circulation. AVF require smaller blood flow rates than the arteriovenous grafts: they are considered functional for venous flow rates larger than 500 ml.min^{-1}, which is to be compared to 650 ml.min^{-1} for grafts [8]. The creation of this type of permanent access is nowadays considered as a standard procedure [13, 14, 15, 16] because of its low complication rate [17]. The suture between the two vessels is called the anastomosis [18].

There exists four types of anastomosis [8]. The nomenclature follows the direction of the blood flow in the circulation:

- the end-to-end anastomosis, when the end of the artery is connected to the end of the vein (A in figure 1.4);
- the side-to-end anastomosis, when the side of the artery is connected

to the end of the vein (B in figure 1.4);

- the end-to-side anastomosis, when the end of the artery is connected to the side of the vein (C in figure 1.4);
- the side-to-side anastomosis, when the side of the artery is connected to the side of the vein (D in figure 1.4).

The nomenclature of the different regions next to the anastomosis is indicated in figure 1.5 [19]. One can distinguish the floor, which is the outer wall of the artery (**A**) in the side-to-end anastomosis; the toe is the region at the outer wall junction between the artery and the vein (**V**); the heel is the region at the inner wall between the artery and the vein; the anastomosis angle θ is the angle existing between the artery and the vein at the heel region.

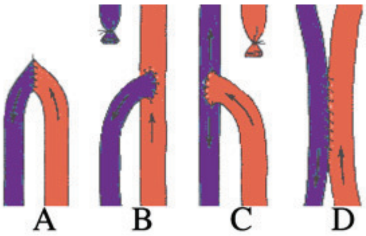

Figure 1.4: A) end-to-end anastomosis; B) side-to-end anastomosis; C) end-to-side anastomosis; D) side-to-side anastomosis [8].

Each configuration presents its own advantages and disadvantages. Chronologically the side-to-side anastomosis has first been created in 1966 [18]. The surgery has been improved in the following years. The end-to-end anastomosis, created for the first time in 1967, can be useful when the vessels have a small caliber. It however cuts off the distal circulation completely. The side-to-end anastomosis, created for the first time in 1968, has become the most commonly used technique. It is indicated when the artery and the vein are not close to one another [11].

The names of the vessels are preserved after the fistula creation: for instance, a side-to-end radio-cephalic fistula is created by connecting the side of the radial artery with the end of the cephalic vein. This fistula located in the forearm region is the first choice for fistula creation owing to its low complication rate [8]. At the elbow region the cephalic vein is superficial and therefore easy to puncture. Moreover, after the maturation period the blood flow inside the vein is usually satisfactory [20].

If the fistula cannot be created in the forearm because of poor vessel quality, the fistula can be placed at other locations in the body. The location is always chosen at the most distal available site, in order to preserve more central vessels in case of failure of the fistula [8, 21]. Surgeons prefer placing the fistula in the lower arm, in the elbow region or in the upper arm, as shown schematically in figure 1.6. But the lower extremities can also be chosen.

An innovative technique that has the potential to increase the amount of information collected during the pre-operative exam and therefore improve the success rate of fistulas is the high-resolution ultrasound technique for venous elastography [22]. Biswas *et al.* have in fact shown that this technique provides an accurate map of the stress-strain characteristic of the venous wall, quantifying the actual state of the vasculature. However, the method is still under study and is not yet ready to be used routinely.

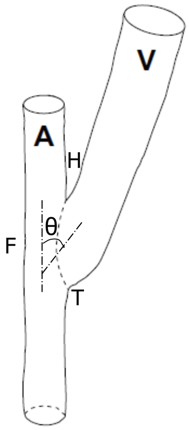

Figure 1.5: Nomenclature of the different AVG parts next to the anastomosis in an arteriovenous fistula: the floor (F), the toe (T), the heel (H), the anastomosis angle θ [19].

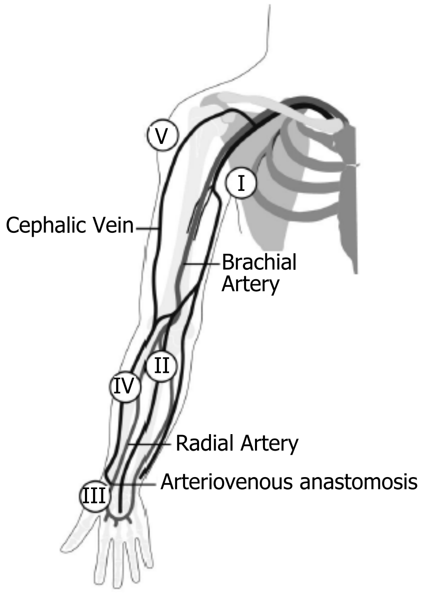

Figure 1.6: Schematic of autologous access types at the upper extremities. The arterial inflow can be located in the upper arm (I), the lower arm (II), the forearm (III). The venous outflow can be located in the forearm (IV) or in the upper arm (V) (modified from [21]).

3 Hemodynamic changes following the creation of a native AVF

Once created, the fistula acts as a low-resistance short-cut between the arterial and venous systems [23]. The afferent arterial flow rate increases significantly during the first 3 to 10 days after the fistula creation [24, 25, 26]. This rise represents the first signature of a maturing fistula.

During the first three to six months following the fistula creation the vein adapts and remodels because of the larger pressure and pulsatility of the blood flow. The vein enlarges and dilates in response to the hemodynamic modifications induced by the newly created, low-resistance circuit [27]. Its collagen content increases because of the larger mechanical loads: the venous wall becomes stiffer and its cross-sectional area increases [28]. This natural response of the compliant vasculature provides a vein that can be punctured 2-3 times per week. Such is not the case for native veins, which become thrombotic if frequently pierced. At the end of the maturation period, the venous flow rate has increased by a factor 20 to 50 when compared to the pre-surgical conditions [14, 29]. It typically reaches values larger than 500 ml.min^{-1}. If the flow rate and pressure are increased, the wall shear stresses remain near the physiological values thanks to the vein enlargement [11, 26].

The vein remodeling, sometimes called 'venous arterialization', is the main outcome of the fistula maturation. It is, however, not the only accommodation which occurs inside the patient cardiovascular system. The low-resistance fistula pathway results in an increase in cardiac output and a redistribution of the blood flow in the whole vasculature. As a consequence, the entire vascular bed is likely to undergo significant remodeling but little is known on these phenomena. The collect of clinical data in the entire cardiovascular system is in fact difficult over several months. Only acute changes in distensibility of large arteries have been documented [30].

When the maturation process succeeds, the AVF can be used for several years. But it may, in some cases, fail. The incidence of early failure is about 20% for fistulas in the forearm [8], but it can increase up to 60% in patients that are diabetic or older than 70 years of age [31]. The aetiology of the failure remains unclear [27]. However, in several cases intima hyperplasia in the region close to the anastomosis and/or reduced vein dilation have been observed. The geometry of the fistula obtained surgically is another aspect which might prevent fistulas from maturing or accelerate the degeneration of a mature AVF. The geometry of the AVF anastomosis is indeed crucial for the post-surgery hemodynamic conditions [14].

4 Flow-related AVF complications and their treatments

4.1 Current detection methods of AVF dysfunctions

Most of the remodeling processes occur during the period of maturation of the AVF. However, the induced non-physiological hemodynamic conditions may in some cases lead to a continuation of the remodelling over a time-scale of several years. Such a remodeling may cause the onset of complications in the mid-long term. They can affect the AVF and lead to local and/or systemic consequences, the first ones implying the AVF failure, the second ones putting a threat on the patient survival.

In Europe only, almost 60,000 new vascular accesses are created each year, and more than 24,000 vascular accesses need to be revisited every year because of complications [32]. The associated costs are high; early detection and treatment of rising pathologies are crucial to reduce them. Detection relies, in clinical practice, on the collect and follow-up of parameters recorded during the hemodialysis sessions. Ensuring repeatability of the conditions over subsequent hemodialysis sessions improves the intra- and inter-dialysis well-being of the patients and maximizes the long-term outcomes. The parameters which are currently measured are:

- the median value of venous blood flow measured during the dialysis session;
- the duration of the dialysis session, automatically computed from the start and end times recorded in the dialysis monitor;
- the median value of pressure in the needle for blood aspiration;
- the median value of pressure in the needle for blood re-injection;
- the patient weight loss over the dialysis session;
- the dry weight, which is the weight expected at the end of hemodialysis.

All these parameters are usually collected manually but Bellazzi *et al.* have proposed an automatized method of measurement [33].

Changes of one or more of the collected parameters over hemodialysis sessions are usually a signature of the onset of complications. Variations in the venous blood flow directly affect the clearance of toxins during hemodialysis, which can lead to less effective treatments [34]. The median values of pressure at both the arterial and venous needles indicate, when stable, that the vascular access is efficient. Alterations of the quality of the vascular access modifies the arterial and venous needle pressures and has repercussions on the bulk flow [33]. The dialysis time is important to ensure the correct removal of catabolites (other than urea) and water [35, 36]. Finally, it is crucial to reach the dry weight target for the hydro-saline homeostasis: in the interval between two hemodialysis treatments the patient accumulates water leading to a weight increase. When the dry weight is reached, one can assume that the accumulated water is entirely removed. It needs to be underlined that this hypothesis is verified if the patient maintains his/her weight, which is obtained giving him a diet to be followed. One risk associated with very high ultrafiltration rates is the potential increase of cardiovascular stress for the patients [37].

Several dedicated exams can be performed to identify and localize the rising pathologies usually causing alterations in hemodialysis parameters [20]:

- Flow test: the flow rate aspired by the pump from the fistula is increased by steps of 50 ml.min^{-1} till the threshold flow rate of 500 ml.min^{-1}. The test is used to verify that the vein is perfused with a minimum flow rate of 500 ml.min^{-1}. If it is not the case, a venous stenosis might be present [28];

- Ultrasound scan: the location of the vascular wall and the direction and velocity of the flow are calculated. The mean velocity and flow rate, obtained by integrating the velocity over the cardiac cycle, are quantified in different branches of the vasculature. The ultrasound technique is flexible, non-invasive and the associated costs are small. It is therefore largely used when a pathology is suspected;

- Fistulography/angiography: the state of the vascular tree is observed by X-rays thanks to the injection of a radio-opaque fluid, since vessels are otherwise transparent to radiography. This exam is routinely performed before the creation of the fistula to evaluate the state of the vessels. Fistulography also allows the identification of pathologies associated with a mature fistula. But radiologists prefer to limit the use of X-rays and radio-opaque contrast liquids on the patients and rely on other imaging technique when possible;

- CT-scan angiography: the 3-dimensional geometry of the patient vasculature is reconstructed by taking a series of X-ray images. The images differ from one another because the X-ray source and detector scan all possible angles around the patient. As for the angiography, a contrast agent needs to be used. This exam is useful for the detection of pathologies of the fistula, but during the exam the patient absorbs a large amount of X-radiation and receives the injection of a radio-opaque contrast agent. The use of CT-scan angiography is therefore limited to its strict necessity;
- Magnetic-resonance imaging: the phase contrast between blood (in movement) and the vascular wall (at rest) is used to visualize the three-dimensional geometry of the fistula. It represents a non-invasive alternative to CT-scan angiography, and is particularly efficient to identify a thrombus. Information about the age of the thrombus can also be obtained by the intensity of the registered electromagnetic signal. However, the application of magnetic-resonance imaging to arteriovenous fistula is difficult because of the tortuosity and the non-planar development of the vasculature.

The data that these exams provide are often more qualitative than quantitative because of the complexity of the AVF geometry. It is important to underline that these exams are not routinely performed since they may be invasive and represent an additional clinical cost. The administration of contrast agents and radiation can be risky if frequently repeated. Moreover, the tortuous morphology of fistulas and the large flow conditions when compared to the healthy case, make these exams difficult and sometimes unsuccessful. In the remaining part of the section, we present the most current complications and the treatment usually performed to preserve or restore the functionality of the fistula.

4.2 Cardiac failure

Clinical studies have shown that peripheral AVFs increase the cardiac output by about 18% [38], which corresponds to an averaged increase of 640 ml.min^{-1} [39]. It is a consequence of the bypass of more peripheral, resistive muscular arteries. Patients undergoing hemodialysis therefore present a higher risk of premature cardiovascular disease [40, 41]. The cardiovascular event with the largest incidence is heart failure and sudden cardiac death [42], whereas it is myocardial infarction in the general population. A strong link between the increased cardiac output and early heart failure has therefore been hypothesized in hemodialysis patients. The risk of heart failure can however be reduced by bending the venous limb of the AVF: in a case-report study it has been shown that this correction reduces the AVF flow rate from 3,710 ml.min^{-1} to 1,410 ml.min^{-1} and preserves the hemodialysis access [39].

4.3 Steal syndrome and ischaemia

The low-resistance venous outflow redirects the majority of the incoming flow to the central veins, especially if the diameter of the vein is larger than 75% of the arterial diameter [43]. The tissues located downstream of the anastomosis might therefore suffer from low perfusion and oxygenation. This phenomenon is called steal syndrome. It can degenerate in tissue ischaemia or even necrosis when the blood supply is below a certain threshold. If necrosis occurs, amputation is needed [44]. Most fistulas remain entirely asymptomatic: ischemia symptoms appear only in 10% of cases. An augmented collateral circulation may in fact counterbalance the low perfusion of the arterial branch of the AVF. A gradual improvement of distal perfusion has even been noted in some cases [45]. Although quite rare, the steal phenomenon can also be related to the presence of a stenosis in the distal artery, but in this case, it has been noticed that the stenosis was present before the AVF creation. It proves the necessity to carefully check the conformation of the vasculature before the surgery [14, 43].

When a patient suffers from the steal syndrome only a few therapeutic options are available. The most common technique aims at reducing the flow going through the vein by increasing its resistance [14, 43, 46, 47]. The increased venous resistance is typically achieved by narrowing, bending or lengthening the vein. These techniques are based on empirism, so neither the optimal degree of narrowing, bending angle nor length of the graft are universally defined [43]. Another technique is called 'distal revascularization - interval ligation'. It consists in feeding the distal artery via an interposed segment of PTFE graft or saphenous vein after ligating the distal artery at the AVF anastomosis [14, 48]. If the surgery fails, the fistula needs to be ligated and created at a different location.

4.4 Hyperflow

The vein can in some cases increase in size after the maturation period. It leads to an increase in the venous flow rate over time, from 500-1,000 ml.min^{-1} at the end of the fistula maturation to values above 2,000-3,000 ml.min^{-1}. This condition represents an overcharge for the heart, and typically occurs in fistulas located in the upper arm [49].

The only surgical solution to this complication is surgical: the venous diameter needs to be reduced in order to increase the venous resistance and therefore decrease the venous flow. However, the optimal venous diameter that should be obtained after this procedure is still unknown. If the vascular conditions make the surgery highly risky, the fistula needs to be definitely ligated. A new vascular access will be created at a different location for hemodialysis [50].

4.5 Aneurysm

Aneurysmal dilatation of AVFs occurs in around 5% of the patients, but this percentage can increase up to 30% in the upper arm [51]. Three factors have been identified as probable leading causes to aneurysm formation: the obstruction of the central venous outflow, the repeated piercing of the same area of the vein or the reduced thickness of the venous wall. The dilatation is called a pseudo-aneurysm if it appears at the puncture site as a direct consequence of the micro-lesions caused at the venous wall at each session of hemodialysis [52].

The aneurysm may have a direct impact on the quality of the hemodialysis treatment: the overlying skin can degenerate and break down increasing drastically the risk of bleeding and infection. In addition, the fistula results to be painful and bruising, which affects the patient quality of life. It has also been reported that patients are bothered by its appearance [53].

Several treatment strategies have been developed with the aim to prolong the usability of native fistulas. Surgical techniques include resection, diameter reduction, reconstruction of the vessel affected by the aneurysm and aneurysm ligation [51]. Endovascular techniques rely on the placement of prosthetic grafts inside the enlargement. Recently, percutaneous approaches have been proven successful [54, 55].

4.6 Stenoses

Stenosis formation results in a reduction of the vascular lumen and an increase in its hydraulic resistance. It is typically caused by neo-intima development or atherosclerotic plaque formation. End-stage renal disease patients typically present several comorbidity, such as hypertension and calcium-phosphate imbalance. These pathologies lead to a diffuse sedimentation of calcium ions at the vascular walls. The calcified regions generally develop in calcified atherosclerotic plaques. Patients in hemodialysis are thus affected by stenoses at multiple sites of the vascular tree, these lesions being not related to altered hemodynamic conditions. Stenoses can affect both the vein or the artery within the AVF. Since the aetiology may be different, we will analyze the formation mechanisms and consequences separately.

4.6.1 Venous stenoses

For many years venous stenoses have been considered to be the main complication affecting arteriovenous fistulas [56]. They typically form in the draining vein near the anastomosis [8] or in the central veins [57]. Their formation has been hypothesized to be associated with two factors: the increased pulsatile pressure [8] and the increased venous flow rate [11]. It is also possible that a stenosis lesion was already present prior to the fistula creation. The increase in flow rate would then make it become symptomatic [11].

Venous stenoses may cause thrombosis and the failure of the hemodialysis access because of insufficient venous flow [58]. It can also lead to difficulties in puncturing, painful arm oedema or prolonged bleeding after needle removal [17]. It ought to be treated if the diameter is reduced by more than 50%. Recommendations also stipulate treatment if it is accompanied with a reduction in the access flow rate [17] and if it leads to a local pressure drop larger than 5-10 mmHg [59]. The best treatment indicated for venous stenoses is balloon-angioplasty. It consists in the endovascular insertion of a balloon folded in a catheter. The balloon is introduced across the stenosis and inflated to restore the vessel lumen. Balloon-angioplasty has been proven to lengthen the period of fistula functionality [57, 60, 61, 59, 62, 63]. For persistent stenoses ultra-high pressure balloons can be used [64]. Another endovascular treatment consists in deploying a stent across the stenosis. Self expandable stents in Nitinol (SMART®, Cordis) or stainless steel (Wallstent®, Boston Scientific) are usually used. They are deployed after the preliminary expansion of the stenosis by balloon-angioplasty.

Stents are currently used in case of unsuccessful angioplasty or recurring stenosis. The use of stenting has in fact been questioned since the late 80s [65]. Clinical studies have shown that after six months, the restenosis rate varies between 15% and 40% [66, 67]. Stenting have hence been used with parsimony to avoid risks of restenosis and to reduce the treatment costs. Recently, it has, however, been proven that stent deployment following angioplasty is more effective than a simple balloon-angioplasty [62, 68]. But at this stage, clinical practices still remain to evolve and adapt to these new results.

When thrombosis occurs, it should be treated in the shortest delay, and in all cases within 48 hours. The thrombus indeed tends to progress very rapidly along the venous wall, making its removal difficult [17]. The most indicated treatments are mechanical/pharmaco-mechanical thrombolysis [69] or surgical thrombectomy [70]. Both treatment types have a success rate larger than 80% [17]. The high success rate of endovascular techniques makes them preferable to the more invasive surgical treatments. However, a large number of patients are still treated surgically [71].

4.6.2 Arterial stenoses

For a long time, the occurrence of arterial inflow stenoses has been considered a rare complication in hemodialysis fistulas [17]. Recent studies have, however, provided a very different picture of the reality. Arterial stenoses have been shown to occur in 40% of patients with a radio-cephalic AVF [58, 72, 73, 74]. The occurrence rate is much lower in patients with a brachio-cephalic fistula (0-4%). The aetiology of arterial stenoses has not yet been studied and remains unknown. It has been hypothesized that inflow stenoses may be linked to the steal syndrome or an increased risk of heart failure [8, 72].

Inflow arterial stenoses are difficult to detect and localize as they do not seem to affect parameters monitored during hemodialysis, unless they are close to the anastomosis. In that case blood recirculation between the aspiration and re-injection needles is observed, causing a significant reduction in the flow rate available for hemodialysis. For all other cases, an ultrasound scan is a possible technique for detection, but it is not part of the routine exam conducted on hemodialyzed patients [75, 76]. So far, the indications for treatment are the same as those used for venous stenoses: a lumen narrowing larger than 50% or a pressure drop higher than 5 mmHg [59].

5 *In vitro* and *in silico* models for the investigation of hemodynamics within AVF

Clinical studies have shown that the fistula creation leads to a remodeling process within the whole cardiovascular system. Evidence suggests that a direct link exists between the hemodynamic/mechanical solicitations observed at the vascular wall and the remodeling process. The quantification of the hemodynamic and mechanical parameters is, however, difficult in clinical practice. Several questions still lie unanswered:

- What is the optimal location where to create the fistula to ensure its maturation and reduce the risk of complications?
- What are the systemic consequences of a functioning AVF?
- What are the local hemodynamic conditions within patient-specific mature AVF? Can failure risks be associated with hemodynamic patterns?
- What is the impact of treatments of failing fistulas on the hemodynamics inside the fistula itself and in the overall cardiovascular system?
- What are the criteria to use in clinical practice to evaluate the degree of success of a surgical or endovascular treatment of a fistula?

In order to answer these questions, it is necessary to quantify local hemodynamic parameters and evaluate mechanical loads on the vascular walls. There is therefore the need to model the blood flow within the vascular network of patients with AVF. Two modelling approaches can be undertaken, either experimental (*in vitro* model) or numerical (*in silico* model). We will review how simulations have contributed to the understanding of the AVF impact and evolution and discuss the implications they have had.

5.1 Overview of *in vitro* and *in silico* modeling of cardiovascular hemodynamics.

5.1.1 Experimental techniques to investigate hemodynamics

Experimental techniques for flow visualization and velocity measurement have been largely used to investigate the hemodynamics within arterial bifurcations and large vessels ([77, 78, 79] among others). Flow visualization techniques rely on the use of dyes or on the seeding of the fluid with particles reflecting light. In the case of fluorescent dye or particles a laser beam is used to selectively enlighten two-dimensional planes of the investigated geometry; the flow patters are recorded by a camera. Flow visualization enables the investigation and characterization of regions of flow recirculation and detachment. This technique has been typically used to investigate the flow patterns in large arteries or at arterial bifurcations (e.g human carotid bifurcation, [77]).

More quantitative results have been obtained measuring the velocity of the fluid. The Laser Doppler Velocimetry (LDV) technique enables the measurement of the instantaneous velocity of the particles dispersed in the fluid at a specific point within the flow field. LDV provides a precise measurement of the velocity, but this measure is punctual. By measuring the velocities on a pre-defined grid of points, quantities such as the local wall shear stresses can be obtained precisely [77].

Another technique is Magnetic Resonance Velocimetry (MRV). MRV is capable of measuring the three component mean velocity field in complex three-dimensional geometries. This technique is based on the phenomenon of nuclear magnetic resonance: MRV utilizes a commercial magnetic resonance imaging (MRI) machine to take an internal image of a stationary target. The molecular spins are aligned with a strong uniform magnetic field ($\sim$1.5 T). Simultaneously, a radio frequency signal adjusted to the resonance frequency is emitted from the machine. This signal alters the spin of the atoms and induces a precession motion at a frequency which is characteristic to each tissue. The MRI device measures this frequency and encodes the position of the emitting atoms. The velocity of a moving target, like in the blood flow, can be measured because moving atoms do not acquire and loose the phase of the magnetic signal with the same characteristic time, contrary to stationary targets. Velocities can be measured along single lines, in planes or in full 3D volumes with sub-millimeter resolution. The advantage of MRV is that no optical access or flow markers are required, so measurements can be obtained *in vivo*, as well as in clear or opaque MR compatible flow models and fluids [80]. This technique has been used to investigate the hemodynamics within realistic phantoms of human aorta and brain aneurysms [79, 81].

The third quantitative technique, which has been developed, is Particle Image Velocimetry (PIV). PIV enables the measurement of the velocity field in particular cross-sectional planes within the investigated geometry. It consists in illuminating a plane with a laser light sheet. Two pictures of the light reflected by the particles that seed the flow are captured by a camera at two instants of times separated by a short time delay. The velocity field is obtained by comparing the position of the particles in both images and calculating the displacement with cross-correlation techniques [82]. The advantage of PIV with respect to LDV is that the velocity measurement is obtained in 2D planes, and not at a specific point. The technique has even been extended to characterize the three-dimensional velocity field (stereoscopic PIV). The standard PIV technique has been largely used to investigate the hemodynamics within abdominal aortic aneurysms and cerebral aneurysms [83, 84, 85, 86] among others. Echo PIV has also been validated experimentally for the *in vivo* study of quantitative velocity profiles and shear stresses [87]. The PIV technique has then been used to quantify the effects of vascular treatments. Charonko *et al.* have for instance investigated experimentally the effect of stent design on wall shear stresses [88, 89]. Ionita *et al.* [90] have focused on the use of asymmetric stent-grafts within phantoms of abdominal aortic aneurysms. But the same technique has also been used to investigate in vitro the efficiency of prosthetic heart valves [91, 92, 93].

5.1.2 Numerical methods

Computational-fluid dynamics models

Computational-fluid dynamics (CFD) models have been initially developed for mechanical engineering applications to analyze fluid flows, heat transfer and their associated phenomena. These models solve for the discrete form of the momentum and mass equations and return the field of motion of the fluid. CFD has emerged in the biomedical field later than in other industrial sectors, such as the car industry, and its application to clinics is still limited. It is mainly due to the complexity of human anatomy and behavior of physiological fluids. Thanks to the hardware and software improvement that took place over the last 20 years, CFD analysis is increasingly performed to study fluid phenomena inside the human cardiovascular system [94, 95, 96, 97]. Medical simulations of circulatory functions offer many benefits. They can lower the chances of postoperative complications, assist in developing better surgical procedures, and deliver a good understanding of biological processes, as well as more efficient and less destructive medical equipments such as blood pumps, valves and other devices (e.g. [94, 98, 99, 100]).

Computational-fluid dynamics (CFD) simulations have been used to simulate the hemodynamics in different vessels of the cardiovascular system. Researchers have mainly focused on the vessels which are mainly affected by cardiovascular pathologies. CFD techniques enable the researchers to quantify the hemodynamic parameters that are supposed to be involved in the onset and development of pathologies, and therefore better understand the relationship between hemodynamics and pathological conditions. Many authors have investigated the hemodynamics in stenotic lesions affecting coronary (e.g. [101, 102, 103, 104, 105, 106, 107, 108]) and carotid arteries ([109, 110, 111, 112] among others). Numerical research has also focused on aortic ([113, 114, 115] among others) and cerebral aneurysms (e.g. [116, 117, 118, 119]) as well as congenital heart diseases (e.g. [120, 121, 122, 123, 124]). The related pathologies have been related to altered hemodynamic factors.

Fluid-structure interaction models

CFD models consider the vascular wall to be rigid, which is not the case physiologically. Modeling the interactions between the blood flow (incompressible fluid) and the deforming vascular structure represents one of the major challenges in cardiovascular mechanics. Different numerical methods have been developed to solve the coupled problem.

One of the most well-known used techniques is the Arbitrary Lagrange-Eulerian (ALE) formulation. In this formulation the Navier-Stokes equations which solve for the fluid field are written in a reference frame which moves with the vascular interface. The evolution of the interface between the blood flow and the vascular structure is determined by the kinematic and dynamic continuity conditions. Perktold and Rappitsch [125] have been pioneers in using this formulation for the simulation of the fluid-structure interactions (FSI) in carotid artery bifurcations, but it has since then been used in various patient-specific models ([126, 127, 128] among others). A limitation of this formulation is the large computational time when the motion of the vascular structure is large.

Another numerical scheme is the immersed boundary method. The immersed boundary method involves both Eulerian and Lagrangian variables. The spatial discretization of the immersed boundary equations is based on a fixed Cartesian mesh for the Eulerian variables, and a moving curvilinear mesh for the Lagrangian variables. The two types of variables are linked by interaction equations that involve a smoothed approximation of the Dirac delta function. The total momentum and total power, which are identical in both formulations, are used to transfer of data from one mesh to the other [129]. The immersed boundary method has mainly been applied to the study of ventricular and heart valves pathologies [130, 131, 132].

The fictitious domain method has firstly been developed by Glowinski *et al.* [133]. This method is related to the immerse-boundary method, but introduces Lagrange multipliers to constrain the motion of the fluid and the solid at the interface. This formulation is particularly adapted to capture rapid motions of the solid domain. It has mainly been used for the study of aortic valve motion [134, 135].

Deforming-spatial-domain/stabilized space-time formulation has been developed by Tezduyar *et al.* [136]. In this formulation the motion of the boundary interface is defined in terms of velocity and displacement. This formulation appears to be particularly effective in terms of computational time. It has been used to study the FSI in patient-specific arteries and cerebral aneurysms [137, 138].

Another formulation that has been developed by the group of Figueroa and Taylor is the coupled-momentum method [139]. This formulation embeds the solid equations into a variational form of the system of the fluid equations. It is obtained via the introduction of a fictitious force, which drives the motion of the solid (this force is related to the traction at the fluid-solid interface if the wall can be assumed to be thin). This formulation results to be robust for large-scale models, if the thin-wall hypothesis is reasonable. It has been used by the same group to simulate large-scale FSI coupled with lumped parameter models at boundaries [140, 139, 141].

The majority of the previous studies consider simplified models of the vascular wall. The vascular wall, however, is anisotropic and inhomogeneous. Holzapfel and his group have developed a mathematical and numerical descriptions of the wall mechanics [142, 143, 144]. The constitutive models are able to capture the anisotropic elastic tissue response in addition to the inelastic phenomena associated with stretching of the tissue beyond the physiological domain. The anisotropic characteristics of wall mechanics have been taken into account to investigate the effects of balloon-angioplasty [142, 145, 146] and stent positioning ([142, 147, 148, 149, 150, 112] among others). In some cases, the structural simulations have been coupled with CFD simulation in order to investigate the effects on the hemodynamics of the simulated treatments [104, 151, 152]. Patient-specific geometries obtained from medical images taken after the clinical endovascular treatment [153, 154, 155] have also been investigated.

5.2 Modeling of a newly-created AVF

In clinical practice, surgeons decide where to create the fistula based on pre-operative scans of the patient vasculature without any quantitative information on the local hemodynamic conditions. It has been proven that the success in maturation of a fistula largely depends on the early hemodynamic changes that follow its creation [24, 25, 26]. The lack of clinical tools that provide detailed maps of the hemodynamics could account for the significant failure rate [8].

Recently, a Lumped Parameter (LP) model has been developed to predict the blood flow within a newly-created arteriovenous fistula [156]. The model is based on the model developed by Bessems *et al.* [157]. It solves for the one-dimensional equations of momentum and mass, modelling blood as an incompressible Newtonian fluid flowing in straight vessels under fully-developed flow conditions. The downstream vascular resistances and compliances are modeled with equivalent resistances and capacitors using an electric analog. The main advantage of an LP model is that it can quantify the flow distribution within the different branches of the patient cardiovascular system both before and after the surgery. In order to correctly set the resistance and compliance values, the pre-operative flow and pressure conditions need to be known.

Hubert *et al.* [156] tuned the resistance and capacitor parameter values to best fit the measurements taken on patients in pre-operative conditions. The simulations were therefore patient-specific. Two possible locations of the fistula were modeled: in the forearm or in the upper arm (figure 1.7). The blood flow distribution was evaluated within the different branches of the vascular tree, imposing the same cardiac output both before and after the surgery. The objective of the study was to estimate which of the two fistula configurations would lead to the more optimal flow conditions. The results of the simulation were confronted to the choice that was made by a surgeon in ten clinical cases of fistula creation. It is interesting that in nine out of the ten cases, the surgeon chose the AVF configuration considered as optimal by the LP model. It turns out that the fistula actually failed in the latter case. In addition, the predicted postoperative flow distribution corresponded to the postoperative flows in six out of ten cases [156]. Since the model is robust and easy to implement in a clinical context, it has the potential to facilitate the routine decision-making process. It could help predict the flow entering the afferent artery after the fistula creation, and reduce the risk of non-maturing fistulas.

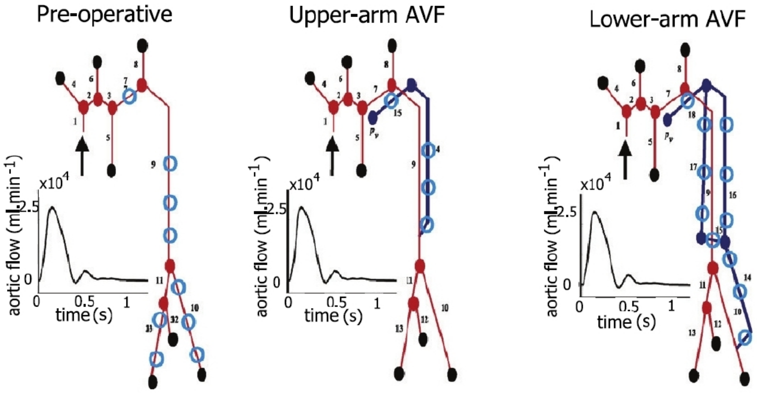

Figure 1.7: Computational domain for the simulations in the pre-operative condition, after the creation of a fistula in the upper or lower arm (modified from [156]). The numbers represent the nodes at which the vessel compliance and resistance properties have been imposed.

5.3 Modeling of the hemodynamics within a functional AVF

In clinics, the quantification of flow velocity is limited. Clinical exams provide estimations of flow rates and of cross-averaged velocities. But the three-dimensional flow patterns are necessary to understand the hemodynamic conditions that prevail in the fistula. Experimental or numerical simulations are therefore necessary to quantify the local velocity field, determine the regions of flow recirculation and provide estimates of the wall shear stresses.

5.3.1 *In vitro* studies

Flow visualization techniques have been used since the late 80s [158, 159, 160, 161, 162] to provide a qualitative picture of the hemodynamics within the fistula. Flow visualization enables the investigation and characterization of regions of flow recirculation and detachment. The studies have all been conducted in simplified models of fistula, with phantoms made of two coplanar straight vessels. The phantom is perfused with steady-state and pulsatile flows. An example of the experimental circuit is shown in figure 1.8. Ojha *et al.* [158] showed the formation of a stagnation point at the anastomosis, where the flow splits between the venous and arterial outlets. The flow exhibited unsteady secondary patterns downstream of the anastomosis. It assumed a spiraling motion inside the distal artery, as shown in figure 1.9. The formation of secondary flow patterns similar to those arising in curved vessels was noticed. However, the details of the flow field in the anastomosis (in which there is an abrupt change in flow direction) were different from those seen in a gradually curved vessel. When studying the local flow patterns in the symmetry plane of the anastomosis Sivanesan *et al.* showed that the flow pulsatility in AVF is very low [23]. It therefore has a limited effect on the hemodynamics: steady-state simulations provide a good estimate of the characteristic flow structures within the AVF (figure 1.10).

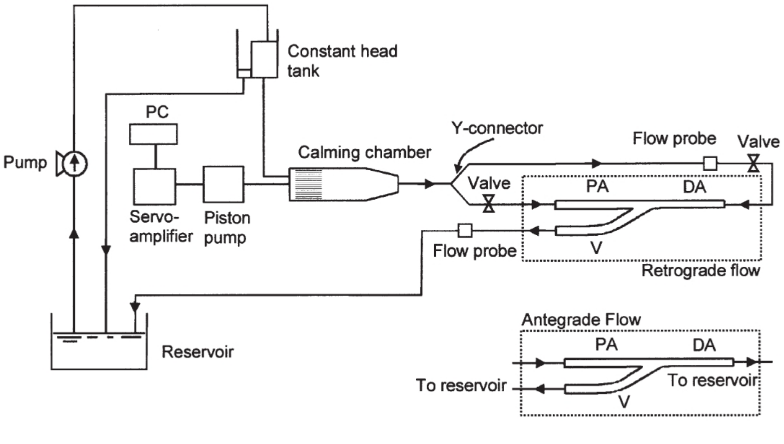

Figure 1.8: Schematic of the experimental set-up for the LDA measurements used by Sivanesan *et al.* [23].

The flow visualization studies also looked at the influence that the geometry of the fistula has on the hemodynamics. Hughes *et al.* [161] showed that the larger the anastomosis angle, the more pronounced the secondary

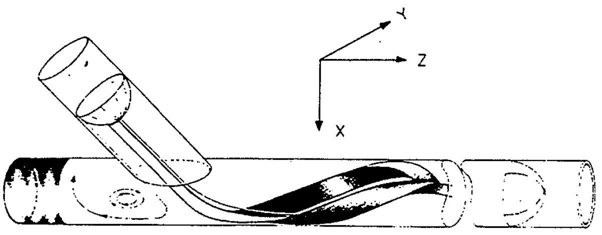

Figure 1.9: Three-dimensional sketch of the dye pathline observed under steady flow conditions [158].

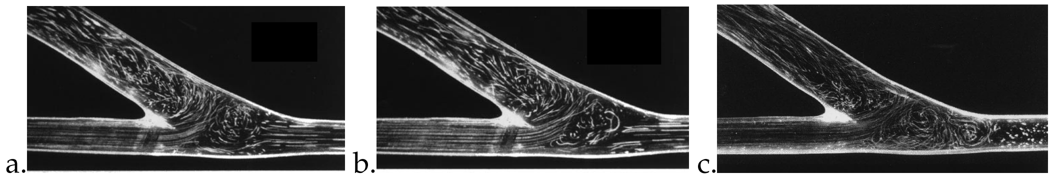

Figure 1.10: Flow patterns at the symmetry plane of an AVF at the anastomosis at the peak systole (a), at late diastole (b) and in case of steady state simulation (c) [23].

flow in the distal artery. Flow separation can be avoided when the anastomosis angle is smaller or equal to 15°even at large flow rates.

Quantitative flow measurements were carried out in the late 90s in idealized models of AVF [163, 23]. The velocity was initially measured at specific locations within the flow using LDV. Estimate of the wall shear stresses (WSS) were calculated from discrete velocity measurements obtained in the vicinity of the vascular wall in a plane perpendicular to it (figure 1.11). Physiological wall shear stress values fell in the range 1-2 Pa in healthy arteries [8] and in the range 0.8-3 Pa in healthy veins [164]. Non-physiological values of wall shear stresses have been associated with endothelial damage (for high values of WSS) or neointima proliferation (for low values of WSS). Sivanesan *et al.* [23] evaluated the wall shear stresses at the inner and outer wall of the vein at different locations away from the anastomosis center. They have observed that the wall shear stress values at the outer wall of the vein decrease from a value of 40 Pa near the anastomosis center to 7-14 Pa 24 mm far from the center. The amplitude of the wall shear stress oscillations also decreases from a value of 50 Pa to 8-9

Pa. Wall shear stresses were therefore found to oscillate between extremely high and extremely low values. Similarly, Li and Rittgers [163] investigated the influence of different flow ratios between the outlets of an end-to-side arterial bypass graft on the local wall shear stresses at the floor and heel regions of the anastomosis. In particular they focused on flow ratios between the two outlets equal to 0-100 (I), 25-75 (II) and 50-50 (III). The authors have shown that both the wall shear stresses and oscillatory shear index at the arterial floor were significantly larger in case I. Differences between cases II and III were not significant. At the graft hood, the oscillatory shear index and wall shear stresses were lower in case I than in cases II and III. But at this location the wall shear stresses differ between cases II and III, case II showing lower values than case III.

LDV experiments have therefore provided an accurate evaluation of wall shear stresses at selected locations. However, LDV cannot provide directly the velocity field in a plane or the distribution of streamlines, as the velocity is measured at point locations.

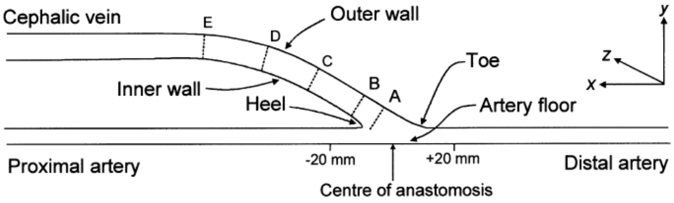

Figure 1.11: Axial positions along graft hood and artery floor for velocity measurements [23].

The first study that obtained two-dimensional measurements of the velocity field was conducted by Kharboutly *et al.* [165]. The velocity field was measured by PIV in a patient-specific phantom of AVF (figure 1.12). The two planes of measurements are indicated on the image of the geometry inserted in figure 1.12. The velocity fields were compared with numerical results obtained in the same vessel geometry using a computational fluid dynamic code. Figure 1.13 shows that a good qualitative correspondence is achieved throughout the cardiac cycle. It was confirmed quantitatively, comparing the velocity profiles.

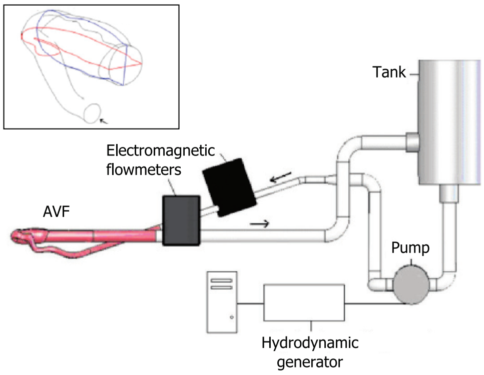

Figure 1.12: Schematic of the experimental set-up for the PIV measurements used by Kharboutly *et al.* [165]. Within the box a magnification of the anastomosis is shown. The red and the blue lines indicate the 2 planes considered for the analysis of the hemodynamics (modified from [165]).

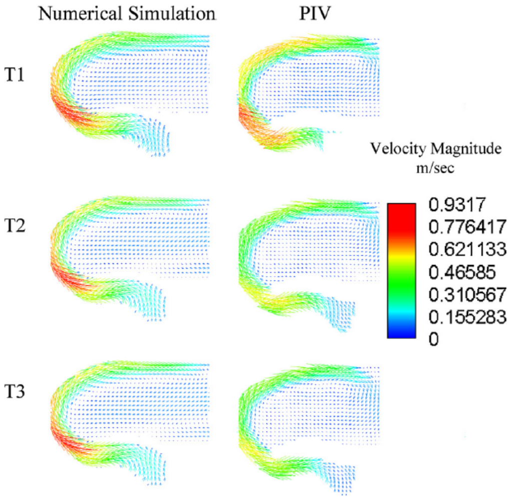

Figure 1.13: Velocity vector cartography in the horizontal plane (PH) for the three time cardiac instants T1 (peak systole), T2 (middle value) and T3 (late diastole) [165].

As shown in this section, both idealized and patient-specific models have been used to model the hemodynamics within an AVF. Each model type has its proper advantages and disadvantages. Idealized models enable to complete parametric studies and evaluate the influence of various parameters (geometry, flow rate, pressure, etc) on the flow conditions. General trends/conclusions can be deduced from the results, which is not possible from patient-specific models. Patient-specific models, however, enable to measure velocities and wall shear stresses in a realistic vessel mock. If the imposed flow profile and boundary conditions are well suited, the hemodynamic quantities thus measured should be a faithful representation of the flow conditions in the patient's AVF.

5.3.2 *In silico* studies

When considering the literature on the hemodynamics in arteriovenous fistulas, one can notice a much greater number of numerical studies compared to experimental ones. Modeling the unsteady flow conditions inside a complex AVF geometry may indeed be less challenging numerically. Numerical models also have the advantage that the geometric parameters and boundary conditions can be varied systematically: parametric studies are therefore easier to perform *in silico* than *in vitro*.

Computational fluid dynamics (CFD) simulations investigated the 3D hemodynamics inside arteriovenous grafts [162, 166, 167] and autologous fistulas [19, 165, 168, 169, 170, 171]. These studies aimed at better understanding the local hemodynamics and how it evolves in the presence of intimal hyperplasia, stenosis and vascular alterations. Kharboutly *et al.* [170] for instance related regions of low wall shear stresses to calcified regions in a patient-specific AVF wall (figure 1.14). In particular they found a potential association between calcification regions and high temporal wall shear stress gradients. Similarly, Ene-Iordache and Remuzzi [19] associated the zones of flow recirculation inside the AVF to those of wall remodelling (figure 1.15) in idealized fistula geometries. The importance of the anastomosis angle was also highlighted [20, 168]: in general angles smaller than 10°are to be avoided, since they lead to a local increase in wall shear stresses. This result might appear in contradiction with the one mentioned in section 5.3.1. But the studies searched for the optimal angle with two different objectives: the *in vitro* study aimed at minimizing the detached flow region, while the *in silico* study aimed at minimizing the wall shear stress. It suggests that the optimal anastomosis angle is a compromise between the minimization of the flow detachment and local wall shear stresses.

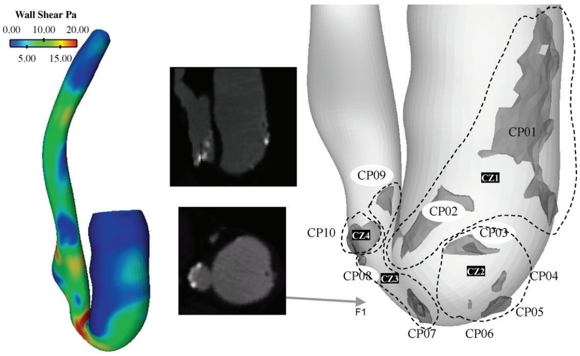

Figure 1.14: The wall shear stress distribution is shown on the left-hand side. From CT-scan angiography data (of which two sections are reported in the centre of the figure) the 3-D distribution of calcified regions has been obtained, and calcification plaques ’CP’ have been distinguished by calcification zones ’CZ’, as shown on the right-hand side [170].

So far surgeons and nephrologists only rely on clinical flow measurement techniques to estimate the flow conditions. The use of in silico models would provide a more complete and accurate picture of the hemodynamic conditions. It would be of great support to decide on treatments and plan surgical acts. Still, patient-specific numerical models have their limits. Various parameters are not and cannot be taken into account. One instance is the presence of other pathologies, such as diabetes, which modify the vascular response to physio/pathological sollications. But too little is known on such co-factors to so far include them in numerical simulations.

5.4 AVF pathologies: optimization of the strategies for detection and treatment

More recently, simulations have been used as a tool to investigate pathological conditions and optimize surgical and endovascular treatments. Van Canneyt *et al.* [172] proposed a method for the early detection of a stenosis inside the vein or at the anastomosis. The detection relies on the use of a brachial sfigmomanometer to measure the pulse pressure. Before be-

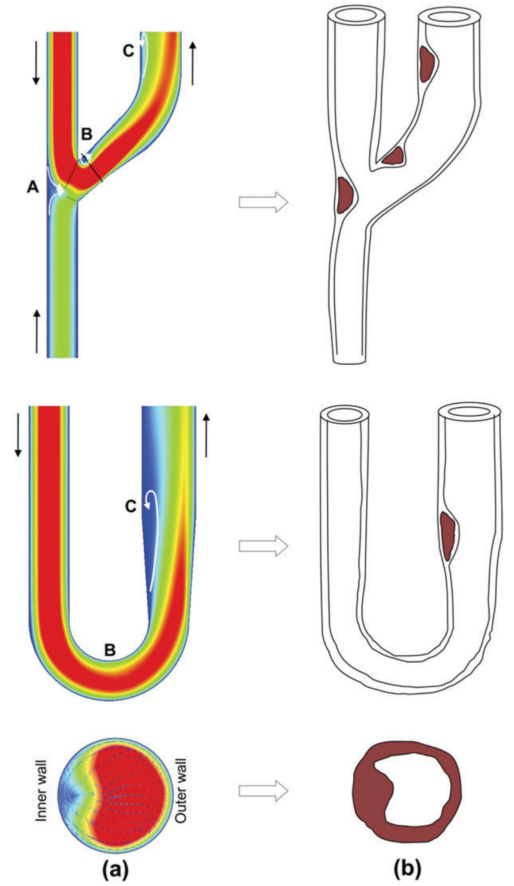

Figure 1.15: a) Contour of the velocity magnitude. The cut-plane shows the recirculation zones. b) Areas where the low wall shear stresses ant the large oscillatory shear index trigger formation of neointima with subsequent increase in wall thickness [19].

ing potentially used routinely on patients, the result of Van Canneyt *et al*. would first need to be validated through a clinical study. One would need to prove that the benefit for the patient outweights the inconvenience of adding yet another instrument during the hemodialysis session.

This example proves that modeling approaches have a great potential to study pathologies affecting fistulas and their associated treatment. It is indeed possible to predict how to optimize the treatment techniques. If three-dimensional simulations were coupled with lumped parameter models [172], it would be for example possible to investigate the influence that pathological fistula have on the cardiac output.

6 Objectives

We are interested in numerically modeling the hemodynamics within a patient-specific arteriovenous fistula. We propose a model which takes into account the compliance of the vascular wall. It represents a novelty compared to the state-of-the-art, since the numerical models developed so far for the AVF have considered the wall to be rigid.

We also differentiate the venous from the arterial mechanical properties and consider the non-Newtonian blood behavior. The investigated patient-specific geometry presents an 80% stenosis at the proximal radial artery. We are interested in better understanding the impact of the arterial stenotic lesion on the hemodynamics. We also want to investigate the effect of the endovascular treatment of an arterial stenosis.

We firstly simulate the treatment by balloon-angioplasty, and investigate the impact of the degree of residual stenosis which persists after the treatment. Then we simulate the treatment of the stenosis by balloon-angioplasty followed by stent positioning. The effects of angioplasty both without and with stenting are compared.

Chapter 2

Material and methods

1 Geometry

1.1 Patient-specific arteriovenous fistula

1.1.1 Image acquisition, segmentation and volume reconstruction

Nowadays angiography imaging techniques (CT-scan or magnetic resonance) provide a high-quality three-dimensional (3D) volume rendering of the vasculature of the patient in real time. It is, however, not adapted for numerical purposes. Angiography images therefore need to be post-processed using segmentation and reconstruction techniques in order to obtain the 3-dimensional geometry of the patient-specific vascular tree.

The segmentation and volume reconstruction procedures aim at isolating the vessel lumen from surrounding tissues and structures. During his PhD, Zaher Kharboutly developed specific numerical techniques to segment and reconstruct of patient-specific fistulas [20]. Since the medical images are encoded in greyscale, the segmentation consists in extracting the structures that have grey levels contained within a certain range. A good contrast between the vessel lumen and the other tissues is required for a successful segmentation procedure. Technically, it is obtained using the methods called ’active contours’ and ’region growing’ (see [20] for details). One must note that the reconstructed geometry depends on the choice of the range of greylevels. It is therefore operator-dependent. Moreover, there may be variabilities in grey levels for images taken at different times during the cardiac cycle or in sequential cardiac cycles. At the end of the segmentation procedure the isolated geometry is cleaned up to remove possible vessels, calcified plaques and bone structures that would have been retained inadequately (figure 2.1).

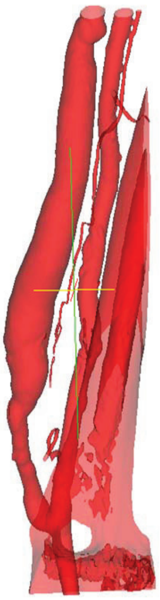

Figure 2.1: Patient-specific AVF geometry obtained by volume reconstruction [20].

In figure 2.2 we show the fistula geometry after the reconstruction and clean-up procedure, ready to use in numerical simulations. The different parts of the investigated vasculature have been identified (proximal radial artery, distal radial artery and cephalic vein) as well as the location of the stenosis throat. We call S_a^i the arterial inlet, S_a^o the arterial outlet and S_v^o the venous outlet.

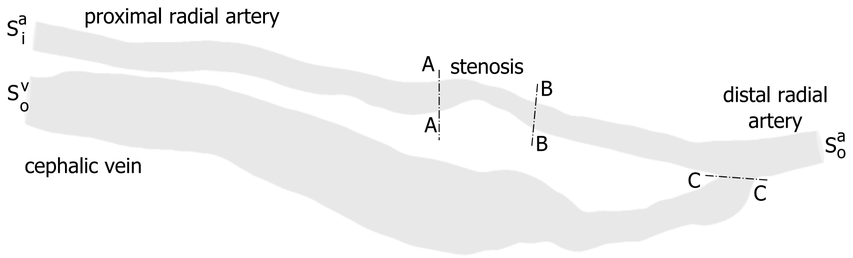

Figure 2.2: Patient-specific AVF geometry. S_a^i is the arterial inlet, S_a^o the arterial outlet and S_v^o the venous outlet.

1.1.2 Partition of the vascular wall

At the end of the volume reconstruction procedure we firstly extract the vascular wall. We triangulate the lateral surface wall, and partition it within ANSYS T-Grid by creating cut-planes. This partition aims at differentiating the mechanical properties of different vasculature segments, as shown in figure 2.2. We isolate the vein from the artery by splitting the entire vasculature at the level of the anastomosis (plane C-C in figure 2.2). We also separate the stenosed portion of the artery as the segment between the cutting planes A-A and B-B (figure 2.2).

1.1.3 Meshing of the fluid volume and vascular wall

The fluid volume mesh is created with ANSYS T-Grid (ANSYS, Inc.). We start from the triangulation of the lateral surface wall of the reconstructed AVF lumen. The volume mesh is made of an hybrid grid, which combines a prismatic boundary layer and a core meshed with tetrahedrons. Both cell element types are linear. More details on the mesh generation technique may be found in Kharboutly et al. [169]. The fluid volume mesh is exported from T-Grid in MSH format, which can be directly imported in the ANSYS computational fluid dynamic solver.

The vascular wall is extracted from the volume mesh. It is meshed with triangles. It shares the same nodes as the fluid mesh at the interface. It is exported in STL format from T-Grid. It is then meshed with a single layer of discrete-Kirchhoff theory-based, four-node linear-triangular shell finite elements: the "Shell 181" elements implemented in ANSYS-Structural (ANSYS, Inc.). The solid mesh consists of 89×10^3 shell elements.

1.1.3.1 Spatial convergence of the mesh grid Different mesh sizes have been tested in order to guarantee a maximum error of 1% on the velocity magnitude and wall shear stresses within a reasonable computational time t_{comp}. All meshes have been created using the method described in section 1.1.3.

We have investigated meshes of maximum element length Δl_{max} equal to $1, 2, 4, 5, 7$ and 10×10^{-3} mm. We choose as reference the results obtained with the smallest mesh size (10^{-3} mm). We calculate the relative error $\varepsilon_u = |u - u^{ref}|/u^{ref}$ on the maximum value of the velocity magnitude ($u = v_{max}$) and time-averaged wall shear stress ($u = \overline{WSS}$).

Figure 4.2 shows that the numerical procedure converges with respect to Δl_{max} approximately as $\Delta l_{max}^{4.8}$ and that the normalized computational time decreases about linearly with Δl_{max}. We have chosen to run the simulations with the mesh characterized by a maximum element length of 4×10^{-3} mm, since it respects the 1%-error limit (horizontal line in figure 4.2a) for both the velocity and wall shear stress and runs four times faster than the reference case (figure 4.2b). The total number of elements for the patient-specific geometry is then 784×10^3.

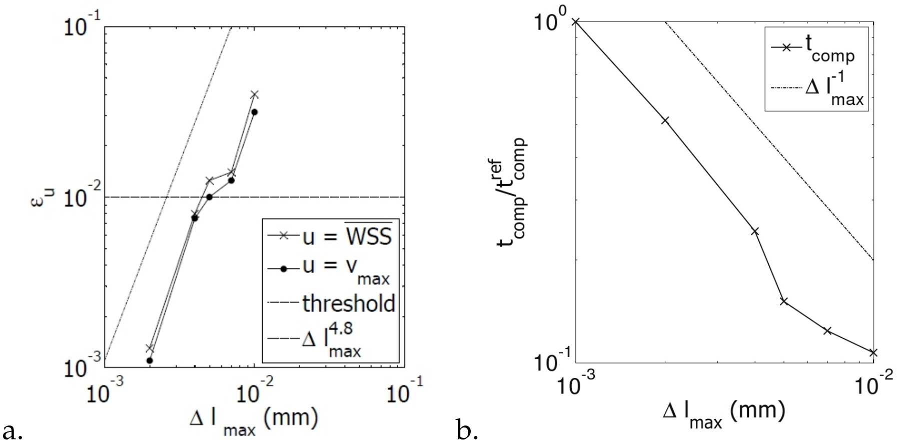

Figure 2.3: (a) Relative error on the maximum velocity ($\varepsilon_{v_{max}}$) and time-averaged wall shear stresses ($\varepsilon_{\overline{WSS}}$) as a function of the maximum mesh length Δl_{max}. The horizontal line indicates an error of 10^{-2}, chosen as the threshold. (b) Normalized computational time t_{comp}/t_{comp}^{ref} as a function of the maximum mesh length Δl_{max}. The reference case corresponds to the mesh with a maximum element length of 10^{-3} mm.

1.2 Angioplasty balloon

We model the angioplasty-balloon as a cylindrical surface. The cylinder is created within ANSYS-Geometry (ANSYS, Inc.). Its length is 15 mm and its diameter 1 mm. The balloon surface is meshed with linear triangular elements. The triangular elements are modeled as the shell elements "Shell

181" implemented in ANSYS (ANSYS, Inc.).

1.3 Stent

The stainless steel wire stent Wallstent (Boston Scientific; Natik, MA, USA) is one the most used to treat stenosed fistula. It is a self-expandable, braided stent (figure 2.4). We model its geometry as a tubular shape made from sets of wires spiraling clockwise and anti-clockwise. The stent is created with the software PyFormex (copyright ©Benedict Verhegge), developed in Python, a scripting language. Python is well suited to generate, transform and manipulate large geometrical models of 3D structures through sequences of mathematical operations. The stent has a length of 12 mm and a deployed diameter equal to 4.2 mm. It is composed of 24 separated wires. Before being exported in ABAQUS format, the structure is meshed with the sweep method. We obtain the stent meshed with hexahedrons. The details of the script used are shown in annex A.

Once imported in ANSYS-Workbench environment the ABAQUS file of the stent is re-meshed within ANSYS-Structural with the native algorithm for ANSYS-Workbench applications. The quality of the ABAQUS mesh is indeed too poor for numerical simulation in ANSYS. In particular we:

- import each wire within ANSYS-Structural;
- delete the existing mesh;
- mesh the wires with the default sweep, patch conforming algorithm.

We thus obtain the twenty-four wires meshed with tetrahedrons.

2 ANSYS-Workbench environment

We have chosen ANSYS-Workbench as the environment for the fluid and solid numerical simulations. The version 13.0 of the software has been used on an Intel(R) Xeon(R) workstation with 64 bit CPU dual core processors of 2.67 GHz clock speed, 23.9 GB RAM memory and a Microsoft Windows XP operating system. ANSYS 13.0 (ANSYS, Inc.) combines the strength

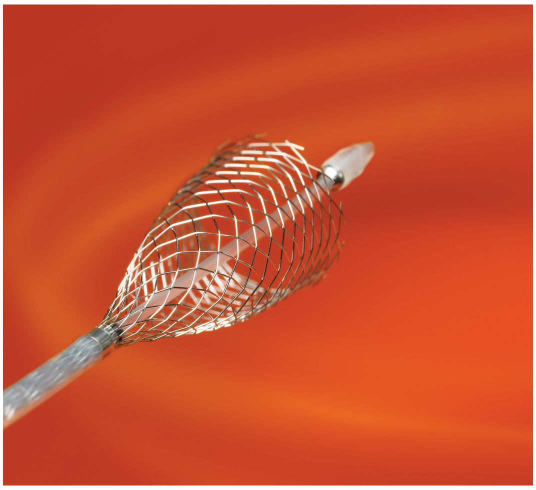

Figure 2.4: Picture of the wire stent Wallstent (Boston Scientific; Natik, MA, USA) as available on Boston Scientific website (http://bostonscientific.mediaroom.com/).

of native core solvers with project management tools allowing the user to customize the work-flow [173]. In figure 2.5 we show the home interface of ANSYS-Workbench.

Within ANSYS-Workbench one can solve fluid, structural, thermal or electro-magnetic problems. Each type of simulation has its proper interface, called 'Analysis System'. The analysis systems implemented in Workbench can be found in the 'Toolbox' menu (figure 2.5). These systems can be added to the project stand-alone or combined with others depending whether the problem to be solved is multi-physics or not. When a stand-alone system is created, the user defines the geometry, mesh, boundary and initial conditions, and then runs the solver. The set up of a multi-physics project requires to build connections between the different analysis systems. The strength of ANSYS-Workbench is that each analysis system maintains its proper interface and solves the relative problem with a native solver. In the case of a fluid-structure problem, the interaction between the two systems takes place at the interface between the fluid and solid geometries, where the results of one analysis are passed to the other analysis [173].

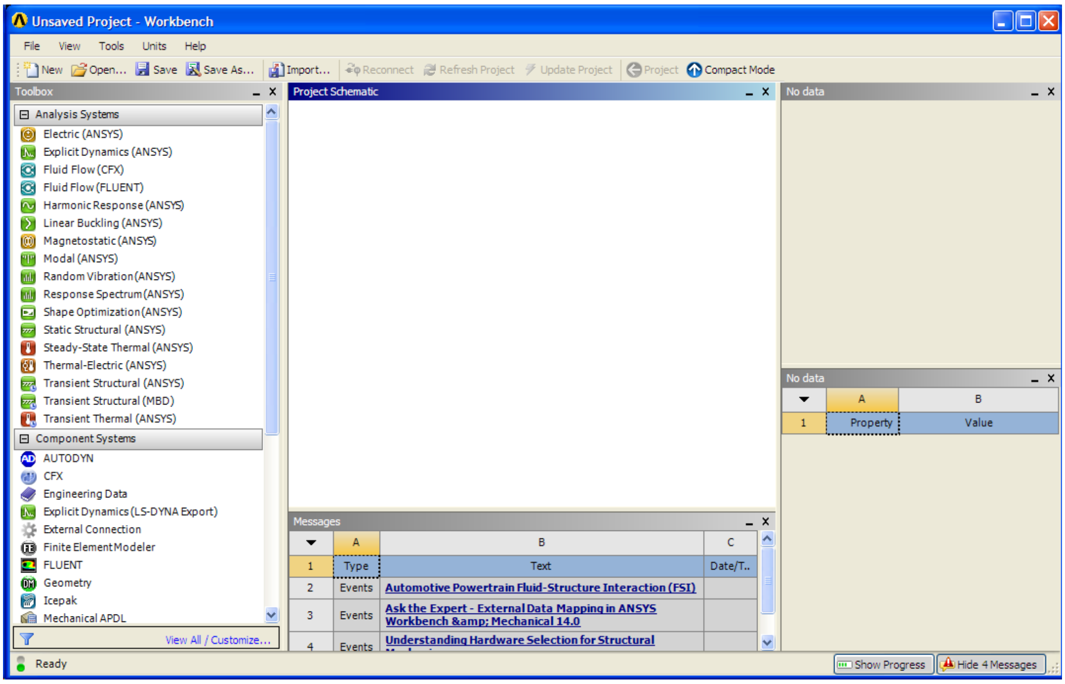

	A	B	C
1	Type	Text	Date/T..
2	Events	Automotive Powertrain Fluid-Structure Interaction (FSI)	
3	Events	Ask the Expert - External Data Mapping in ANSYS Workbench & Mechanical 14.0	
4	Events	Understanding Hardware Selection for Structural	

Figure 2.5: Main interface of ANSYS-Workbench. In the toolbox one can find all the physics ('Analysis Systems') or parts ('Component Systems') which can be added to the 'Project Schematic' in order to build-up the specific analysis.

2.1 The use of meshed geometries within ANSYS-Workbench

The fluid and solid meshes described in section 1.1.3 of this chapter need to be imported within ANSYS-Workbench. We describe separately the import of the fluid volume mesh within the fluid solver and the import of the solid mesh within the structural solver.

2.1.1 Import of the volume meshed geometry

When ANSYS-CFX (computational fluid dynamic, CFD, solver) is added in ANSYS-Workbench the user has firstly to define the fluid geometry and its associated mesh. For this study we use the geometry of the AVF lumen meshed as described in section 1.1.3. The MSH file created in T-Grid (ANSYS, Inc.) is imported right clicking on the box 'Mesh' of the CFX system. This geometry can be scaled to the correct unit system if necessary. Once imported the mesh file cannot be modified.

2.1.2 ANSYS FE-Modeler

We use ANSYS FE-Modeler to import the solid geometries (AVF wall, stent, balloon) and convert them into ANSYS-Structural system [173]. Neither the vascular wall of the AVF nor the wires of the stent are meshed in a native format for the Workbench environment. The AVF wall is indeed meshed in STL format and the stent in ABAQUS format. Such mesh formats cannot be directly read by ANSYS-Structural. The imported mesh has no units. The user is therefore in charge of notifying the dimension units during the import.

2.1.2.1 Steps to be followed within ANSYS FE-Modeler When a mesh is imported in the ANSYS FE-Modeler application, the menu 'Geometry Synthesis' allows the user to generate a geometry from a finite element model. The first step consists in identifying the exterior faces of the imported geometry(ies) with the 'Skin Detection Tool' (figure 2.6). This tool enables the user to select the threshold angle which allows to correctly identify the imported geometry as a single body. The angle is in fact evaluated among facets at the external meshed surface of the body. For too small threshold angles, adjacent facets of the mesh can be separated and the body partitioned in a multi-component body. In same cases this partitioning can be useful to facilitate the transfer of the mesh in ANSYS-Structural. We have presently used a large value of threshold angle ($\geq 50^o$) to ensure that the bodies are single-component structures.

Once the skin of the bodies is detected, the geometry needs to be converted in a format that can be read in ANSYS-Structural. One has to define a so-caller 'Initial Geometry'. The 'Initial Geometry' appears in the tree menu (see figure 2.6), and it contains all the bodies that have been identified with the 'Skin Detection Tool' and that will be transferred to ANSYS-Structural. The user can decide to group two or more bodies in a 'Part' and two or more parts in an 'Assembly'.

The 'Initial Geometry' can be, if necessary, modified with the transformation tool using the specific licence called ANSYS Mesh Morpher license

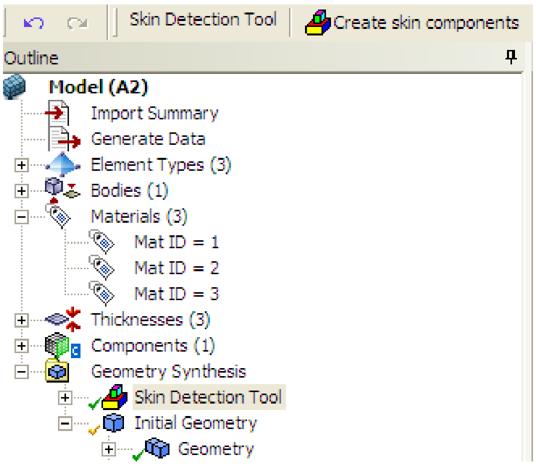

Figure 2.6: Outline of the ANSYS FE-Modeler.

[173] through the 'Target Configuration' feature. The 'Initial Geometry' is first copied into the 'Target Configuration', which is then modified. Each transformation implies a modification of the geometry or of its position in space in the 3-dimensional reference system. Note that the numbering of nodes and elements remains unaltered by the transformation. The 'Target Configuration' has a parameter associated which is zero when the 'Target Configuration' is created. The first transformation which is imposed modifies the value of the parameter. For instance, if the first transformation is a translation of 0.01 m the parameter value is modified to 0.01. When the 'Target Configurations' correspond to the geometrical characteristics that the user needs for the analysis, the 'Parametrized Configuration' has to be updated. It is important to update this configuration before carrying on the analysis. It is indeed the 'Parametrized Configuration' that is transferred to ANSYS-Structural within ANSYS Workbench. This update is made effective simply by substituting the parameter values in the 'Parameter Set' section of the Workspace (P1 Mesh.Morpher.1) shown in figure 2.7 with the value associated to the 'Target Configuration'(1). This parameter is zero by default and has to be changed to the parameter value associated with the 'Target Geometry' within the interface of ANSYS FE-Modeler. The update of these parameters makes the transformation effective for the export in

---

(1) The user simply clicks on the value of P1 Mesh.Morpher.1 and overwrites it with the value associated with the target configuration.

different ANSYS-Workbench systems.

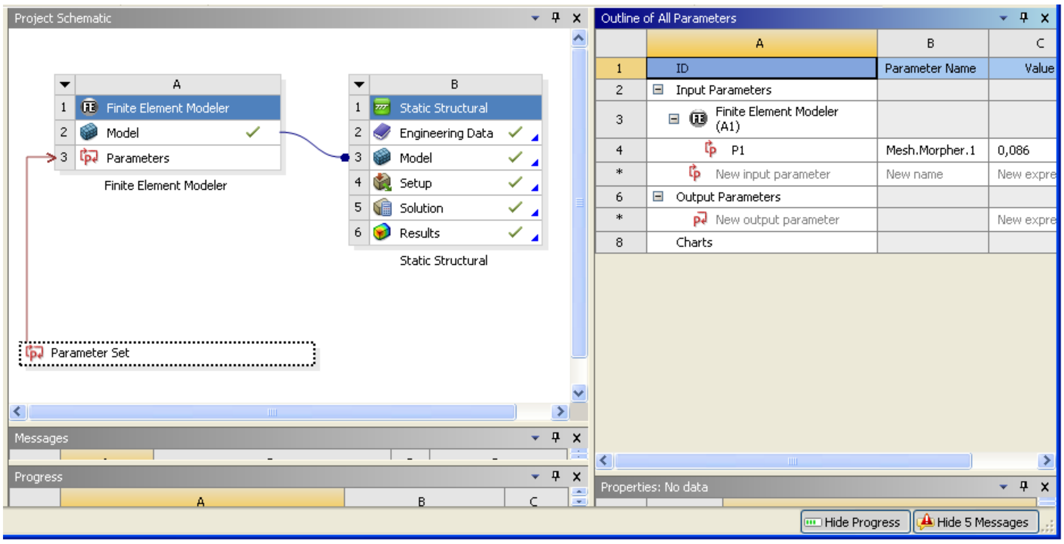

	A	B	C
1	ID	Parameter Name	Value
2	⊟ Input Parameters		
3	⊟ Finite Element Modeler (A1)		
4	P1	Mesh.Morpher.1	0,086
*	New input parameter	New name	New expre
6	⊟ Output Parameters		
*	New output parameter		New expre
8	Charts		

Figure 2.7: 'Parameter Set' section of the Workspace, in which the value of the parameter has to be changed to correctly read the transformed geometry in ANSYS-Structural.

We have used the transformation tools when importing together the balloon, the artery and the stent since they are created within different software tools. The balloon and the stent need to be positioned across the stenosis throat and centred onto it. To ensure that the quality of the transformed mesh is preserved, the extent of the transformations one applies must be limited [173]. The 'Initial Geometry' and its associated mesh can be transferred to other Workbench applications, such as ANSYS-Structural.

2.2 ANSYS-CFX

ANSYS-CFX is the system which solves the computational fluid dynamics in ANSYS 13.0. The user is guided step-by-step in the setup of the model. The schematic of the pipeline is shown in figure 2.8. In the following paragraphs we detail the model setup we have used.

2.2.1 Computational fluid dynamic numerical method

ANSYS-CFX (ANSYS, Inc.) is used to solve the fluid continuity and momentum equations in their conservative convection-diffusion form [173].

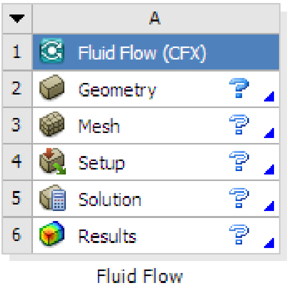

	A
1	Fluid Flow (CFX)
2	Geometry ?
3	Mesh ?
4	Setup ?
5	Solution ?
6	Results ?

Fluid Flow

Figure 2.8: Pipeline of ANSYS-CFX system, the computational fluid dynamic solver implemented in ANSYS-Workbench.

These equations are solved implicitly with the Rhie-Chow interpolation method [174]. We presently consider the atmospheric pressure as reference pressure and we neglect gravity. For time-integration, we use the high-resolution, second-order backward Euler scheme implemented in ANSYS-CFX fluid solver (ANSYS, Inc.). This scheme is a second-order accurate, implicit time-stepping scheme, recommended for non-turbulent flow simulations [173]. The system of algebraic equations is solved iteratively using a time-step Δt equal to 5 ms. At each time step, the residual is calculated and reported as a measure of the overall conservation of the flow properties. The maximum allowed residual is 10^{-4}. To reach convergence at each time step, we set a maximum number of sub-iterations equal to 100, but convergence is verified in less than 10 iterations at the first time step and in less than 5 iterations at all the following time steps. All the transient simulations are initialized with the results obtained running the equivalent steady flow simulation with time-averaged quantities as boundary conditions.

2.2.2 Model setup

By double-clicking on the 'Setup' box a window dedicated to the simulation pre-processing opens. Within this window, the user can define all the simulation conditions. The following paragraphs describe in detail the setup parameters we have used.

2.2.2.1 Blood model Blood is assumed to be an isotropic, homogeneous, non-Newtonian fluid. Blood density is set to 1050 kg.m^{-3} and its apparent viscosity μ is assumed to follow Casson model. The apparent viscosity μ can be expressed as

$$\sqrt{\mu} = \sqrt{\frac{\tau_0}{\dot{\gamma}}} + \sqrt{\kappa}. \tag{2.1}$$

where τ_0 represents the yield stress, $\dot{\gamma}$ the shear rate and κ the consistency. The model parameters have been chosen according to experimental data obtained at low shear rates: $\tau_0 = 4 \times 10^{-3}$ Pa, $\kappa = 3.2 \times 10^{-3}$ Pa.s [175].

2.2.2.1.1 Validation of the need of a non-Newtonian blood model In a non-Newtonian model the dynamic viscosity is function of the local shear rate. For large shear rates, the equivalent dynamic viscosity is constant and the fluid behaves as Newtonian. For low shear rates, the non-Newtonian effects are significant and the local equivalent viscosity increases. In figure 2.9 we show the equivalent dynamic viscosity values observed at the AVF wall. Inside the radial artery the dynamic viscosity is equal to $3.2{\times}10^{-3}$Pa.s^{-1}. It corresponds to the value the model gives for large shear-rates, when the fluid follows a Newtonian behavior. Within the enlarged vein the non-Newtonian effect are significant: shear rates are in fact lower than 100 s^{-1} and the equivalent dynamic viscosity becomes up to 6 times larger than within the artery. The choice of the non-Newtonian model is therefore justified by the low shear rate conditions that prevail inside the cephalic vein and which lead to significant non-Newtonian effects. In this region, the wall shear stresses would be overestimated by a Newtonian model.

We have quantified the error made on the wall shear stresses if a Newtonian model was used. The dynamic viscosity μ has been set to $3.2{\times}10^{-3}$ Pa.s^{-1}, corresponding to the dynamic viscosity given by the Casson model at large shear rates. Inside the proximal artery the error is almost zero. The largest error on the wall shear stresses is found in the enlarged vein: at this location we observe a spatial-averaged error of 13%, with peaks of 20%. At the anastomosis the errors are within 15%, with a spatial average of 10%. This is coherent with the finding of Kabinejadian and Ghista [176].

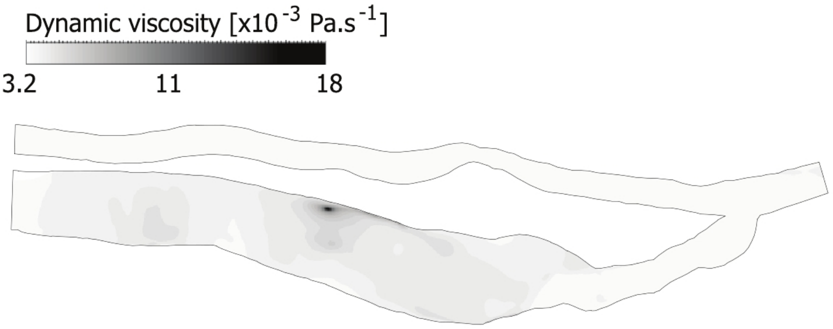

Figure 2.9: Dynamic viscosity values obtained at the AVF wall with the Casson's model.

2.2.2.2 Modeling of the flow conditions The simulations are run under the hypothesis of laminar flow. This hypothesis is coherent with the fact that the prescribed boundary conditions (detailed in section 2.2.2.3 of this chapter) correspond to a systolic Reynolds number of 800, a time-averaged Reynolds number of 650 and Womersley number of 4. Since the fluid is not reactive we do not impose combustion, thermal radiation or heat transfer.

2.2.2.3 Boundary conditions No-slip conditions are imposed at the vascular wall. The section-averaged velocity v_a^i is the one that was measured by echo-Doppler on the patient on the same day as the CT-scan angiography [170] and it is shown in figure 2.10. We have prescribed the flat, time-dependent profile of v_a^i at the inlet of the proximal radial artery (S_a^i in figure 2.2).

At each of the two outlets S_a^o and S_v^o, we impose a flow-dependent pressure condition based on a RC Windkessel model [177]. This model is based on the hypothesis that the hemodynamic behavior of the vessel network downstream of the 3D-geometry outlet is related to its compliance and resistance. If one models the vessel compliance with a capacitor and the hydraulic resistance as an electrical resistance, one can generate a zero-dimensional model of the flow through the network based on a simple electrical analog circuit.

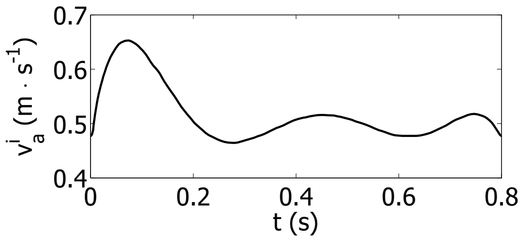

Figure 2.10: Flat, time-dependent velocity profile v_a^i prescribed at the inlet of the proximal radial artery (S_a^i in figure 2.2). It corresponds to the section-averaged velocity measured on the patient.

We have modeled the behavior of the downstream vasculature as a capacitor C in parallel with a resistance R. The relationship between the blood flow rate Q and the pressure P is given by the equation

$$\frac{\partial P}{\partial t} = \frac{1}{C}\left(Q - \frac{P}{R}\right), \tag{2.2}$$

which becomes upon discretization

$$\frac{P_i - P_{i-1}}{\Delta t} = \frac{Q_i}{C} - \frac{P_i}{RC}. \tag{2.3}$$

The index i represents the current time-step and $i-1$ the previous one. The model therefore requires the pressure value at time step $i-1$ to be available to the solver. It is obtained by creating an additional variable that we have called 'PPrev'. The variable 'PPrev' allows the storage of the pressure values at the previous time-step at each point of the geometry. In the command editor the CCL variable 'PPrev' is defined as⁽²⁾

```
LIBRARY:
  &replace ADDITIONAL VARIABLE: PPrev
    Option = Definition
    Tensor Type = SCALAR
    Units = [Pa]
    Variable Type = Specific
  END
```

---

(2) 'Additional Variables' are added in the section 'Fluid Domain', 'Fluid Model' in the tree menu within ANSYS-CFX.

```
END
```

Re-arranging the terms of the equation 2.3, we obtain

$$P_i = \frac{P_{i-1} + \dfrac{Q_i}{C}\Delta t}{1 + \dfrac{\Delta t}{RC}}. \tag{2.4}$$

The parameters R and C have been estimated using the technique of Molino *et al.* [178]. It requires to know

- the pulse pressure, defined as the difference between the systolic pressure P_s and the diastolic pressure P_d at the considered outlet within one cardiac cycle;
- the time-averaged pressure $\overline{P}$ at the flow outlet;
- the time-averaged blood flow rate $\overline{Q}$ at the same flow outlet.

From the flow rate data measured by echo-Doppler, we obtain the time-averaged flow rate. Neither the pulse pressure nor the time-averaged pressure can be measured directly on the patient. In order to calculate the pulse pressure $P_s - P_d$ we run a rigid-wall simulation where the desired flow split between the arterial and venous outlets is imposed and free pressure outlet conditions are set at sections S_o^a and S_o^v. We find a pulse pressure equal to 12 mmHg. The same simulation returns also the value of the pressure drop within the AVF geometry for the imposed flow inlet. According to the literature, functional fistulas may have a mean pressure in the proximal radial artery between 50 and 100 mmHg [179]. The range of values is large, since it is a function of the patient general health conditions. To cover the entire possible range, we have run 3 simulations with different time-averaged inlet pressures $\overline{P}_a^i$ (table 4.1). For each value of $\overline{P}_a^i$, we have estimated the corresponding values of $\overline{P}_a^o$ and $\overline{P}_v^o$. At this stage, we have an estimation of the mean pressure, the pulse pressure and of the flow rate at each outlet. We can therefore apply the model of Molino *et al.* [178] to our data. The values of the constants R and C are calculated for both the arterial (denoted by subscript a) and venous (subscript v) outlets of the considered domain (table 4.1).

No data exists in the literature on the pressure and flow conditions in fistulas that could help compare the present R and C constants calculated for the segments downstream of the arterial and the venous outlets. Values can be calculated in the healthy case from the data provided by Westerhof [177] for comparison. The present values are of the same order of magnitude as in the healthy case. At the venous outlet the constant C tends to be larger but by maximum an order of magnitude, and the R values only slightly smaller. Conversely, at the arterial side the constant C is about 5 times smaller than in the healthy case and the value of R increases up to 8 times the healthy case values.

It is also interesting to consider the product of the two constants $\tau = RC$, which is the time constant of the dynamic response of the vascular tissue. It is linked to the capacity of the vascular segment to absorb the peak systolic kinetic energy. We find a time constant τ equal to 0.15 s for the arterial outlet and 0.08 s for the venous one in the case $\overline{P}_a^i = 70$ mmHg. It is coherent to find a larger time constant downstream of the artery, owing to the presence of more elastic vessels downstream of the outlet and of the capillary bed. In large elastic arteries, the time constant is of order 1: Ismail *et al.* [180] found, for instance, $\tau \sim 1$ s for the vascular network downstream of the iliac arteries. This is coherent, since the arterial outlet of the AVF is made of less elastic vessels than those at the outlet of the iliac arteries.

2.2.2.4 Initialization The velocity field is initialized with the solution of the steady-state simulation. In this simulation the fluid properties are kept identical as in the pulsatile simulation. As boundary conditions, we impose the time-averaged values of the inlet velocity at S_a^i and of the venous and arterial pressures at S_v^o and S_a^o, respectively. All the simulations are run taking the atmospheric pressure as the reference pressure.

Table 2.1: Values of the venous and arterial resistances (R_v and R_a) and compliances (C_v and C_a) for the different values of time-averaged inlet pressure $\overline{P}^i_a$. The corresponding inlet pressures at peak systole $P^i_{a_s}$ and diastole $P^i_{a_d}$ are provided for reference. The pressure values are in mmHg, the resistances in 10^8 kg.m^{-4}.s^{-1} and the compliances in 10^{-11} kg^{-1}.m^4.s^2.

$\overline{P}^i_a$	$P^i_{a_s}$	$P^i_{a_d}$	R_a	C_a	R_v	C_v
55	63	51	11.9	4.98	4.77	11.5
70	78	66	30	5	6.5	12
90	98	86	41	5.04	7.4	12.1

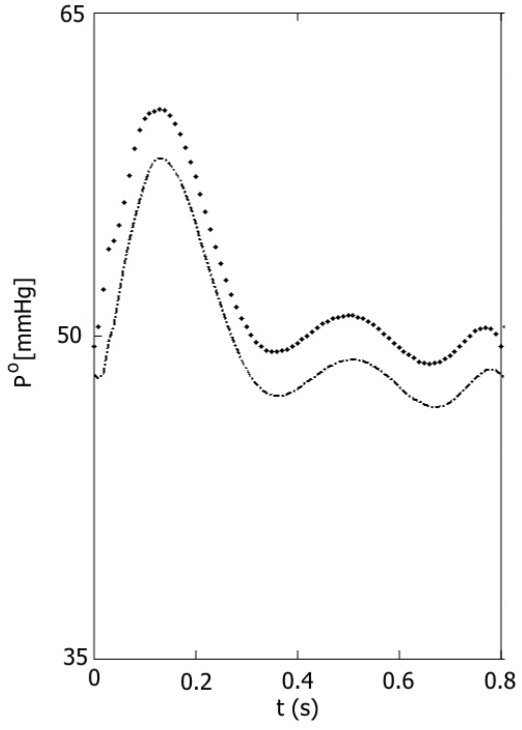

Figure 2.11: Arterial pressure profile P^a_o (dotted line) obtained at the arterial outlet S^a_o and venous pressure profile P^v_o (dot-mark line) obtained at the venous outlet S^v_o. The ordinate axis does not start from a zero pressure.

2.2.2.5 Hemodynamic parameters As part of the post-treatment, we study the evolution of hemodynamic quantities which have been shown to affect vascular remodeling. The wall shear stresses are contained within the plane tangent to the vascular wall, defined by the unit vector normal to the vessel wall **n**. They can be expressed by the two-component vector

$$\tau_w = \mu \frac{\partial \mathbf{v}}{\partial \mathbf{n}}, \tag{2.5}$$

where τ_w is the viscous stress acting tangentially to the vessel wall and **v** the velocity vector. We call wall shear stress WSS the modulus of τ_w. The time-averaged value of WSS, called $\overline{WSS}$ is calculated as

$$\overline{WSS} = \int_0^T |WSS| dt. \tag{2.6}$$

In a healthy radial artery, $\overline{WSS}$ is in the range 1-2 Pa [8], which we will refer to as the healthy physiological $\overline{WSS}$ range. In a vein, it has been reported that neointimal hyperplasia rapidly develops when $\overline{WSS}$ values are below 0.5 Pa [164].

The oscillatory shear index OSI is defined as

$$OSI = 0.5(1 - \frac{| \int_0^T WSSdt|}{\int_0^T |WSS|dt}), \tag{2.7}$$

where T is the time period of the cardiac cycle. The OSI index represents the degree of oscillation in the wall shear stress orientation. Its values fall in the range $[0, 0.5]$, 0 corresponding to a constant forward flow and 0.5 to a purely oscillating flow. OSI values are typically below 0.2 in healthy physiological vessels. A value of 0.3-0.35 is considered as the threshold, above which neo-intimal activation and proliferation might occur [181].

In order to obtain the time-averaged modulus of the wall shear stress $\overline{WSS}$ the user needs to introduce an additional variable, that we call 'wallshearmag'(3). When an 'Additional Variable' is created, a few lines of code need to be written. The user has to define the name of the variable, its type (scalar on vector) and its units. In the details, the lines of code are:

```
LIBRARY:
  &replace ADDITIONAL VARIABLE: wallshearmag
    Option = Definition
    Tensor Type = SCALAR
```

---

(3)'Additional Variables' are added in the section 'Fluid Domain','Fluid Model' in the tree menu within ANSYS-CFX.

```
    Units = [Pa]
    Variable Type = Specific
  END
END
```

Once the variable has been created and defined, the user needs to specify the expression which enable the solver to calculate it. For the 'wallshear-mag' the expression is

$$\sqrt{(Wall\ Shear\ x)^2 + (Wall\ Shear\ y)^2 + (Wall\ Shear\ z)^2} \tag{2.8}$$

where Wall Shear x, Wall Shear y and Wall Shear z, are the name that ANSYS-CFX assign to the three components of the wall shear stress vector τ_w.

The temporal gradients of WSS ($WSSG_t$) are defined as

$$WSSG_t = \frac{\partial WSS}{\partial t}. \tag{2.9}$$

They are typically small in healthy vessels. We will analyze which AVF zones are exposed to non-vanishing values of temporal gradients.

2.3 ANSYS-Structural

2.3.1 Numerical method

The equation system of the solid problem is solved implicitly using the Lagrangian multiplier-based mixed u-P formulation in ANSYS-Structural (ANSYS, Inc.), u standing for the displacement and P for the static pressure. ANSYS-Structural is divided in several parts in order to help the user in the set-up of the model. As for ANSYS-CFX, the steps correspond to sequential interfaces to be opened in ANSYS-Structural. The sequence used to define the model setup is shown in figure 2.7, where an FE-Modeler system is connected to the 'Model' section of the ANSYS-Structural system. These steps consist in:

- Definition of the mechanical properties of the different parts of the bodies to be simulated(4);

---

(4) The definition of the mechanical properties of the different materials is done in the 'Engineering Data' section of ANSYS-Structural

- Definition of the thickness of the shell-element bodies and assignment the material properties to each body$^{(5)}$;
- Definition of the boundary conditions, loads to be applied and solver settings$^{(6)}$;
- Run of the solution$^{(7)}$ and post-process of the results$^{(8)}$.

In the following sections we describe the various steps needed for the simulation.

2.3.2 User-defined mechanical properties: Engineering Materials

When ANSYS-Structural is opened within ANSYS Workbench, one firstly defines the mechanical properties of the body(ies) involved in the simulation. The physical properties of the material(s) the density and then the mechanical behavior. ANSYS supports both linear and non-linear constitutive laws. Among the non-linear laws pre-defined in ANSYS one finds the plastic, multi-linear elastic, hyperelastic, hyperviscoelastic and viscoelastic/viscoplastic laws. The user can also enter additional laws using the 'user defined models'.

In this study we hypothesize that the vascular wall of the AVF behaves as a homogeneous, incompressible, hyperelastic material. We assume that both the artery and the vein follow the 3^{rd}-order Yeoh model [182]. The strain energy function ψ reads

$$\begin{aligned}\psi = C_{10}(I_1-3) + C_{20}(I_1-3)^2 + C_{30}(I_1-3)^3 + \\ D_1(J-1)^2 + D_2(J-1)^4 + D_3(J-1)^6,\end{aligned} \tag{2.10}$$

where I_1 is the deviatoric first principal strain invariant and J the Jacobian. The parameters are the material constants C_{10}, C_{20}, C_{30} and the incompressibility parameters D_1, D_2, D_3. Since the vessel wall is assumed to be

---

(5) The definition of the geometrical characteristics of the different bodies is done in the 'Model' section of ANSYS-Structural

(6) The definition of the mechanical loads and boundary conditions is done in the 'Setup' section of ANSYS-Structural

(7) The solution is run in the 'Solution' section of ANSYS-Structural

(8) The results post-processing is done in the 'Results' section of ANSYS-Structural

incompressible, the Jacobian J is equal to 1. We differentiate the arterial and venous mechanical properties in order to model the larger compliance of the artery as compared to the arterialized vein. The model constants, listed in table 3.1, are the ones that best fit the experimental data of Mc Gilvray *et al.* [183] for the vein and Prendergast *et al.* [184] for the artery. To the authors knowledge, the mechanical properties of the vein of a mature AVF have never been quantified. We therefore consider the stress-strain curve measured by Mc Gilvray *et al.* when the vein is subjected to pure circumferential elongation in mice. In the case of mice, the healthy and the phlebitic conditions are almost undistinguishable since the vein of the mice has a large content in collagen in both cases. We therefore suppose this mechanical characteristic as a good estimation of the mechanical properties of the arterialized vein.

Table 2.2: Values of the constants of the hyperelastic 3^{rd}-order Yeoh model used for the radial artery and the cephalic vein

Constant	**Artery**	**Vein**
$\mathbf{C_{10}}$	0.763×10^{5} Pa	3.784×10^{6} Pa
$\mathbf{C_{20}}$	3.697×10^{5} Pa	5.543×10^{8} Pa
$\mathbf{C_{30}}$	5.301×10^{5} Pa	6.491×10^{9}

The behavior of the stenosed part is modeled with a viscoplastic law. The implementation of the viscoplastic behavior in ANSYS is based on the Maxwell model [173]. We impose a law which has the same stiffness as the healthy arterial parts for small deformations. This choice ensures the mechanical continuity at the interface between the stenosed and non-stenosed segments. At large deformations we have set the law parameter values so that they fit the data of Maher et al. [185].

The balloon and the stent are modeled with linear elastic material properties. For such a material one needs to define the density ρ, the Young modulus E and the Poisson coefficient ν. These mechanical parameters are summarized in table 5.1

Table 2.3: Values of the mechanical properties of the balloon and stent

	Balloon	**Stent**
ρ	1000 kg.m^{-3}	7999 kg.m^{-3}
E	9×10^{8} Pa	2×10^{9} Pa
ν	0.3	0.3

2.3.3 Geometrical and material properties assignment

When opening the 'Model' part in ANSYS-Structural, the user has to assign the proper mechanical properties to each body. If one or more shell element bodies have been loaded, the user also has to define the thickness of the elements. These two operations are done in the section 'Geometry' which is contained within 'Model'. In figure 2.12 we show an example of geometry project in which we define the properties of 'Surface body 1'. This body represents the wall of the cephalic vein of the fistula. We have set the thickness to 0.4 mm and the material properties to vein, which is the name given to the venous mechanical properties saved in the library in the 'Engineering Materials' section. We also set the type of offset for the shell element. It can be set to be either the centerline of the element, its top surface or its bottom surface. We have chosen to define the surface as the top surface as it is the lumen-wall interface.

Since we have partitioned the AVF wall in order to distinguish the venous and the arterial properties, the vasculature is composed by more than one body (see section 1.1.2). In order to make the ANSYS solver treat the parts of the AVF as a single body, we merge the nodes at the interfaces with the command lines

```
/gopr
nummrg,node,2e-5
etcontrol,SUGGESTION.
```

Within the code, line 1 indicates that the command line acts on the geometry; line 2 imposes the merge of nodes located at a distance smaller than 2×10^{-5} mm and line 3 indicates that ANSYS automatically chooses the best element technology to be used by the solver.

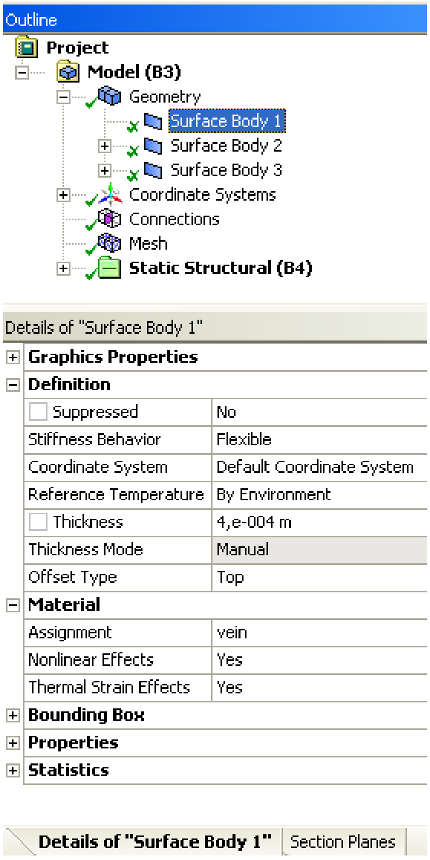

Definition	
☐ Suppressed	No
Stiffness Behavior	Flexible
Coordinate System	Default Coordinate System
Reference Temperature	By Environment
☐ Thickness	4,e-004 m
Thickness Mode	Manual
Offset Type	Top
Material	
Assignment	vein
Nonlinear Effects	Yes
Thermal Strain Effects	Yes

Figure 2.12: Definition of the geometrical and mechanical properties of the 'Surface body 1' which corresponds to the wall of the cephalic vein.

2.3.4 Definition of boundary conditions and loads

Within this section of the Structural system, we differentiate the setup according to the simulation we run. We describe the details of the settings we have used for each case of study:

- Balloon-angioplasty;
- Balloon-angioplasty with stenting;
- Evaluation of the equivalent stiffness of the stented artery;

- Evaluation of the wall internal stresses through a one-way fluid-structure interaction.

2.3.4.1 Implicit simulation of balloon-angioplasty We simulate the opening of the balloon once it is positioned across the arterial stenosis. At the beginning of the simulation the balloon is not in contact with the artery (figure 4.3a). Neither translation nor rotation is allowed at the extremities of the balloon and vessel walls. The balloon is inflated and deflated by an increasing/decreasing linear ramp in pressure. The contact which occurs between the balloon and the artery during the balloon inflation, is supposed to be frictionless [146] and solved using the augmented-Lagrange method.

Figure 4.3b shows when the contact occurs between the balloon and arterial wall. The balloon is further inflated until the maximum pressure is reached (figure 4.3c). It is then deflated, leaving the vessel wall in its post-treatment configuration (figure 4.3d).

Different values of the balloon pressure are imposed (6, 5.6, 5.1, 4.7 bar). They respectively lead to a degree of residual stenosis equal to 0, 10, 20 and 30% after angioplasty. The cross-sections at the stenosis throat are shown in figure 2.14 for the patient-specific geometry presenting an 80% stenosis and for the different post-treatment geometries.

The fluid-region resulting from these geometries has been re-meshed with the same criteria defined in section 1.1.3. It is used within CFD simulations for the evaluation of the effects of the endovascular treatment.

2.3.4.2 Implicit simulation of balloon-angioplasty with stenting The simulation of the stenting treatment is run implicitly in a three-step simulation:

- During the first step the stent body is inactive and we simulate the inflation of the balloon during balloon angioplasty as described in section 2.4.1;
- In the second step the pressure within the balloon is kept constant and the stent body is activated;

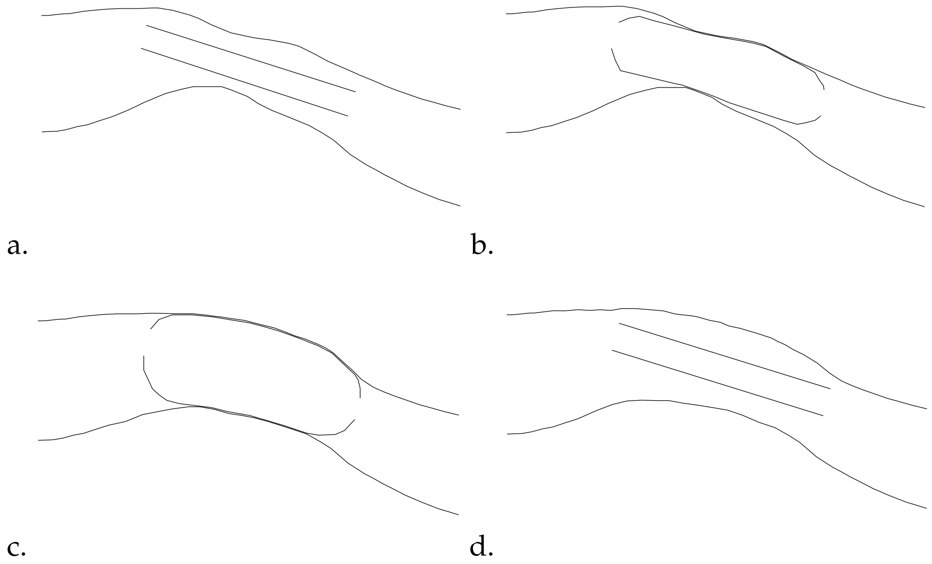

Figure 2.13: Schematics of the numerically-simulated angioplasty procedure. a) Initial configuration: positioning of the balloon within the artery. b) Configuration when the balloon comes into contact with the artery. c) Configuration at maximum balloon internal pressure. d) Vessel final shape when the balloon is completely deflated.

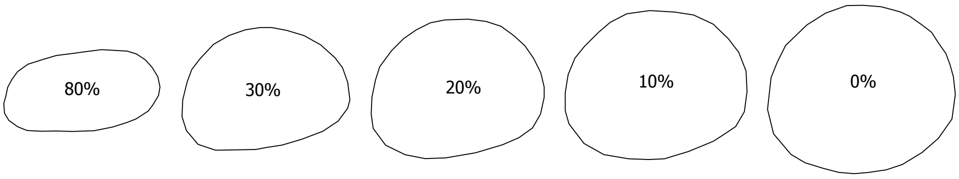

Figure 2.14: Vessel cross-sections at the throat of the stenosis for the patient-specific (80%-stenosis) and treated geometries (30, 20, 10, 0% residual stenosis).

- During the third step the stent deployment within the artery treated by angioplasty is simulated.

The contact between the artery and the balloon is defined as described in 2.4.1. No contact is defined between the stent and the balloon.

A body is made inactive when it is transparent for the other bodies involved into the simulation. However, the inactivation of a body requires at first the definition of the contact in which the inactive body will be involved when activated. We define the contact between the artery and the stent as a frictional following the Coulomb theory. The friction coefficient is equal to 4.5×10^{-2}. The stent body is identified by adding the command lines$^{(9)}$

```
paramC=cid
paramT=tid.
```

The stent is make transparent to other bodies during the first step of the simulation in the section B4 of the model outline (see figure 2.12). The command line which inactivate the stent body are

```
esel,s,type,,paramC
esel,a,type,,paramT
ekill,all
allsel.
```

This command line is applied to the first step of the simulation.

The stent is re-activated by adding the following command lines to section B4 of the model outline (see figure 2.12)

```
esel,s,type,,paramC
esel,a,type,,paramT
ealive,all
allsel.
```

These command lines are applied to the second step of the simulation.

When the simulation requires the inactivation/reactivation of one or more bodies, it is advised to impose the full Newton-Raphson numerical scheme for the calculation of the solution [173]. It is obtained by adding the following command line to section B4 of the model outline (see figure 2.12)

```
nropt, full.
```

2.3.4.3 Evaluation of the equivalent stiffness of the stented artery We are interested in evaluating the equivalent stiffness of the stented artery. We define two models in ANSYS-Structural:

- The stented artery, obtained with the method described in section 2.4.2;

---

(9) 'Connection' section, see figure 2.12.

- The artery in its stented configuration without the inner presence of the stent (bare artery).

We solve for the deformation of the stented artery imposing a ramped internal pressure in the lumen in an implicit structural simulation (Structural Mechanics, ANSYS, Inc.). The contact between the artery and the stent is imposed to be bonded and solved using the Augmented Lagrange algorithm already implemented in ANSYS-Structural (ANSYS, Inc.). We then run the same simulation for the bare artery and search which mechanical properties need to be set to obtain the same deformation as the stented artery.

2.3.4.4 One-way fluid-structure interaction simulation We are interested in the mechanical solicitations that the vascular wall of the AVF undergoes under the hydrodynamic pressure field. The solution of the pressure field needs to be available (resolution of the fluid-problem, section 2.2). The one-way fluid-structure interaction simulation is built up in ANSYS-Workbench connecting a CFX-results system to the 'Configuration' section of ANSYS-Structural, as shown in figure 2.15. The fluid solution at the time step of interest is loaded in CFX-results. The user has to open the CFX interface and select the vascular wall as the boundary on which the variable to be exported (the pressure in the case of study) has to be calculated.

When the 'Configuration' interface is opened, one can see 'Import Load' in the tree menu (figure 2.16). By right-clicking the user can select 'Include Pressure'. The surface on which the pressure is applied as boundary condition needs to be specified: one needs to select the internal face of the AVF wall. The 'Imported Pressure' needs to be refreshed and then the simulation can be run.

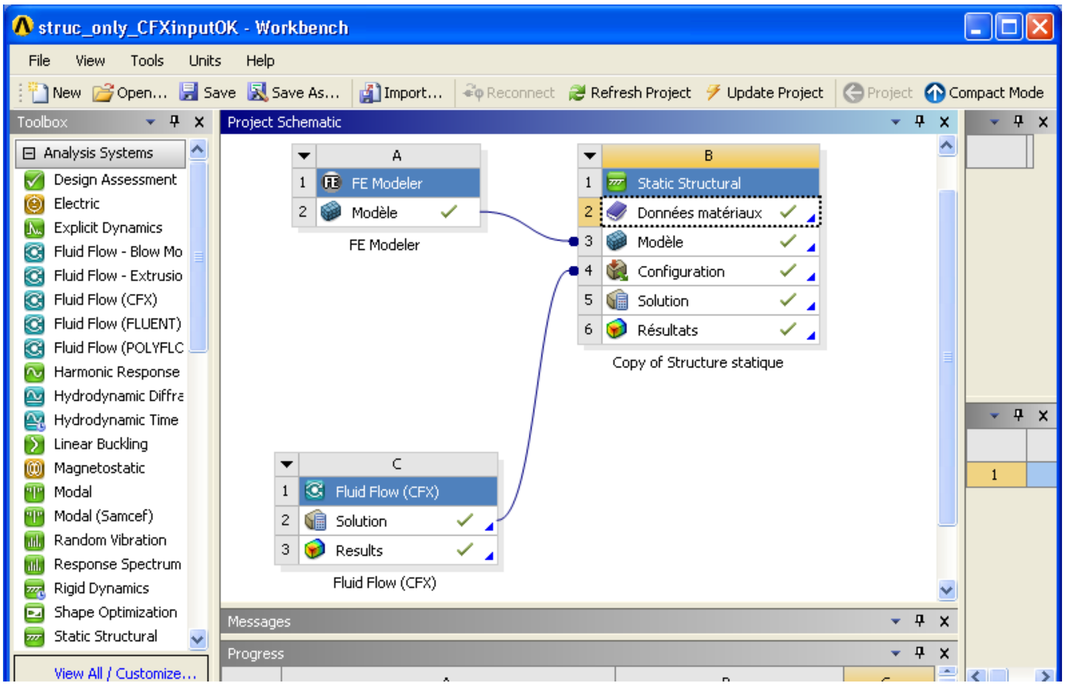

Figure 2.15: Screen-shot of the connection that need to be created within ANSYS-Workbench to run the one-way simulation returning the AVF wall displacements and internal stresses for a pressure field previously calculated within a fluid-dynamic simulation.

2.4 Fluid-structure interaction

2.4.1 Numerical method

The transient fluid-structure interactions are simulated inside the AVF using ANSYS-Workbench V13.0 (ANSYS, Inc.), coupling ANSYS-CFX and ANSYS-Structural implicitly [173]. The schematic of the links made in ANSYS-Workbench to run such a simulation are shown in figure 2.17. The software is based on an arbitrary Lagrangian-Eulerian formulation. It uses a partitioned approach with stagger iterations within each time step. During each stagger iteration:

- The displacement vectors are transferred from the structural to the fluid solver, where the fluid problem is solved for the current time-step;
- The load vectors are then transferred from the fluid to the structural

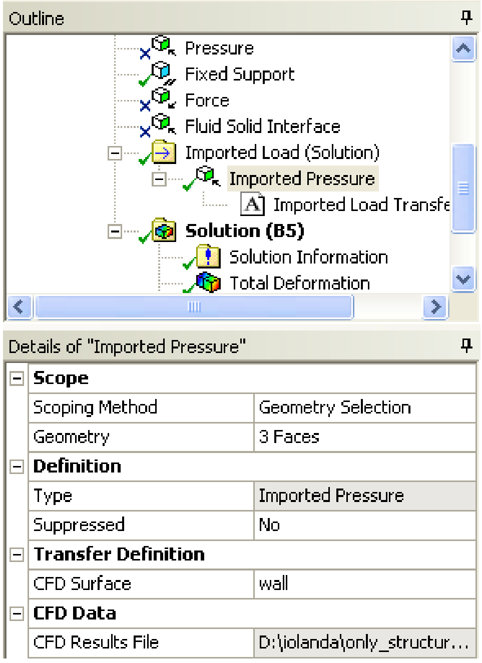

Details of "Imported Pressure"

Scope	
Scoping Method	Geometry Selection
Geometry	3 Faces
Definition	
Type	Imported Pressure
Suppressed	No
Transfer Definition	
CFD Surface	wall
CFD Data	
CFD Results File	D:\iolanda\only_structur...

Figure 2.16: Detail of the tree menu of the 'Configuration' interface of ANSYS-Structural. The load imported from the fluid domain is specified.

solver, where the structural problem is solved;

- The convergence of all the field equations (fluid and structural) is evaluated.

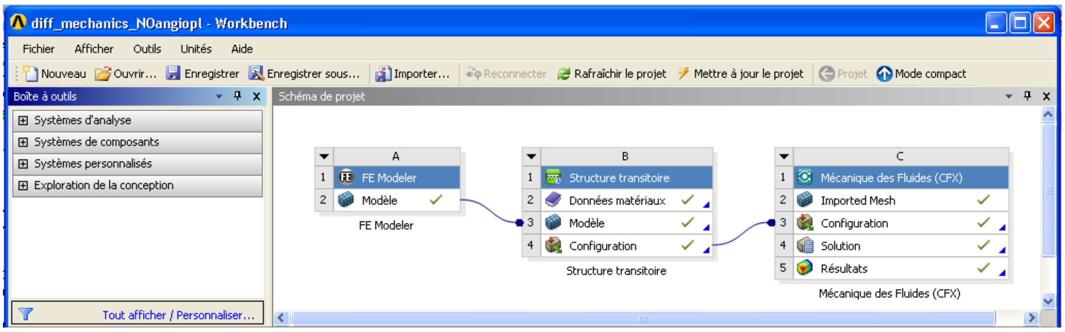

Figure 2.17: Links between the Structural and CFX solvers in order to run FSI simulations within ANSYS-Workbench (ANSYS, Inc.).

Stagger iterations are repeated until all the field equations have converged and the coupling conditions are satisfied at the fluid-solid interface: (1) displacements of the fluid and solid domains are compatible, (2) forces acting on the interface are at equilibrium, (3) the fluid obeys the no-slip condition.

The finite element structural solver uses a Lagrangian multiplier-based mixed u-P formulation. The simulation is performed assuming large displacements. Each FSI simulation is run over six consecutive cardiac cycles, corresponding to a simulated time of 4.8 s. A time-step equal to 5×10^{-3} s is defined for both the fluid and the solid solver.

2.4.1.1 Optimization of the time step for the fluid-structure interaction simulation We have searched for the optimal time-step for which (i) the numerical model is stable, (ii) the computational time is the smallest, (iii) the temporal resolution is sufficient to capture the time-dependent flow features. We have tested 3 values of the time step: 10^{-3}, 5×10^{-3} and 10^{-2} s. We find that the simulation is unstable with a time step of 10^{-2} s, but remains stable with the two smaller values. The numerical scheme is therefore conditionally stable, with a limit of stability between 5×10^{-3} and 10^{-2} s. Reducing the time step by a factor of 5 hardly has an effect on the accuracy of the results: the results obtained with a time step of 5×10^{-3} s differ by less than 1% from those obtained with 10^{-3} s. It, however, has a direct impact on the computational time, which increases linearly with the number of iterations. We have therefore chosen to run all the following simulations with the time step of 5×10^{-3} s in order to optimize the computational time without loss in accuracy. The simulation time is approximately 70 CPU hours.

2.4.1.2 ANSYS-Structural: setup for FSI simulation The internal surface of the vascular wall has been defined to be the interface between the fluid and the solid physics. It is set to receive the load from the external software and send back the resulting displacement. Neither translation nor rotation is allowed at the vascular extremities (corresponding to sections S_i^a, S_o^a and S_o^v in figure 2.1). The external tissues are supposed to be at atmospheric pressure, which is the pressure of reference in the FSI simulation. The gravity has been neglected.

2.4.1.3 ANSYS-CFX: setup for FSI simulation Blood model and flow conditions are the same as described in sections 2.2.2.1 and 2.2.2.3. The wall boundary is defined as a 'Multi-physics Interface'. The fluid solver is set to send the loads at the interface to the solid solver and receive from it the displacement.

3 Experimental simulation

3.1 AVF geometry

A phantom having the same geometry as described in chapter 1 has been fabricated. A CAD model of the geometry has been created by Innovaltech (IUT de l'Aisne, Saint-Quentin, France) from the volume reconstruction of the AVF lumen is exported in STL file format. The vascular walls are generated with a thickness of 3 mm which is required for the rigidity of the mould. A phantom made in poly(methyl methacrylate) (PMMA) is fabricated by rapid prototyping. The 3D printing of the object is obtained by depositing PMMA microcapsules. The capsules are liquefied by a laser beam where the material needs to be added.

The 3D phantom is shown in figure 2.18. Its transparency is sufficient to enable the measurement of the inner velocity field. One can still notice some imperfections (grooves). They are a consequence of the technique of material deposition used during rapid prototyping. However, the transparency of the mould is optimized by conducting all the experiments within a water bath. The phantom is rigid. We will therefore simulate numerically the hemodynamics in a CFD simulation with ANSYS CFX.

3.2 PIV: Principles

Particle Image Velocimetry (PIV) is a technique that allows the estimation of the velocity field in a 3-dimensional flow by calculating the velocity vectors in a cut-plane, as introduced in chapter 1, section 5.1.1. The typical PIV setup consists in a Charge Coupled Device (CCD) camera for image acquisition, a double pulsed laser for lighting the flow field seeded with particles

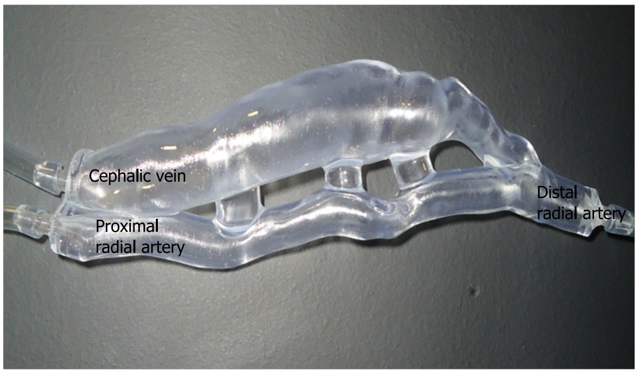

Figure 2.18: Phantom of the AVF: the 3-dimensional mould is obtained by rapid prototyping.

and a PC for synchronization with the laser pulse and image recording. A software enables to control the laser and camera, determine the velocity field and post-process the data.

The PIV technique relies on the capture of two images (A and B) at two sequential times t_1 and t_2, where $t_2 = t_1 + \Delta t$. A fast doubled shuttered CCD camera is typically used to record the images with double exposure. Δt can be in the range from hundreds to thousands of μs, depending on the velocity of the fluid motion. Images A and B are employed to detect the variation of the position of tracer particles (for instance nylon or lycopodium) dispersed within the flow. The information about the particle displacement during the period Δt is then processed in order to estimate the velocity field within particular regions of the fluid [186]. The time lag Δt between the successive firing of the two lasers is an important parameter because it is directly involved in the calculation of the velocity. During this time, a particle that has been recorded in the image A, moves to another position, recorded in the image B. An estimate of Δt can be obtained from the value of the mean velocity and targeting a mean displacement of the particles of 5 pixels between two successive frames. The minimum time delay between the two laser pulses is dictated by the time resolution of the camera. Moreover, since the camera aperture is larger during the first frame (frame A), the second frame (frame B) has a lower background intensity [187].

The images are analyzed with the two-frame cross-correlation technique. It calculates the displacement correlation peak R_D [186]. Cross-correlation technique includes several steps:

- Divide each double-frame image into interrogation spots and copy the interrogation spot to memory for analysis;
- Compute the correlation;
- Find the displacement peak R_D
- Determine the displacement $\Delta\mathbf{x}$, which corresponds to the displacement to be imposed at the interrogation spot in frame B to make the particles overlap the correspondent interrogation spot in frame A;.

The second, third and fourth steps must be repeated for each interrogation spot in which the image has been divided [187]. The velocity of the particles $\mathbf{u}$ is then calculated as

$$\mathbf{u} = \frac{\Delta\mathbf{x}}{\Delta t}. \tag{2.11}$$

The spatial resolution of the PIV analysis is defined by the size of the first interrogation spot [186]. In order to obtain reliable velocity field measurements, a spot should contain from 7 to 10 particle pairs, where one pair refers to a particle imaged at both t_1 and t_2 [82]. The particle concentration must in fact be sufficiently high to detect the main characteristics of the flow but not to elevated to avoid speckle phenomena. Note that the velocity of a particular interrogation spot is a function of the average displacement of the particles in the spot. In order to obtain good image quality, it is also important to ensure that the particles and the fluid have the same density. This condition guarantees that the fluid and the particles have the same velocity by avoiding gravity effects.

3.3 PIV: Experimental setup

The experimental setup has been installed in the Biomechanics and Bioengineering Laboratory (CNRS UMR 7338) at the Université de Technologie de Compiègne (figure 2.19). The experiments have been carried out by

Tommaso Vassallo, a master student who did his final stage in the laboratory. The laboratory is provided with a specific room for particle image velocimetry measurements.

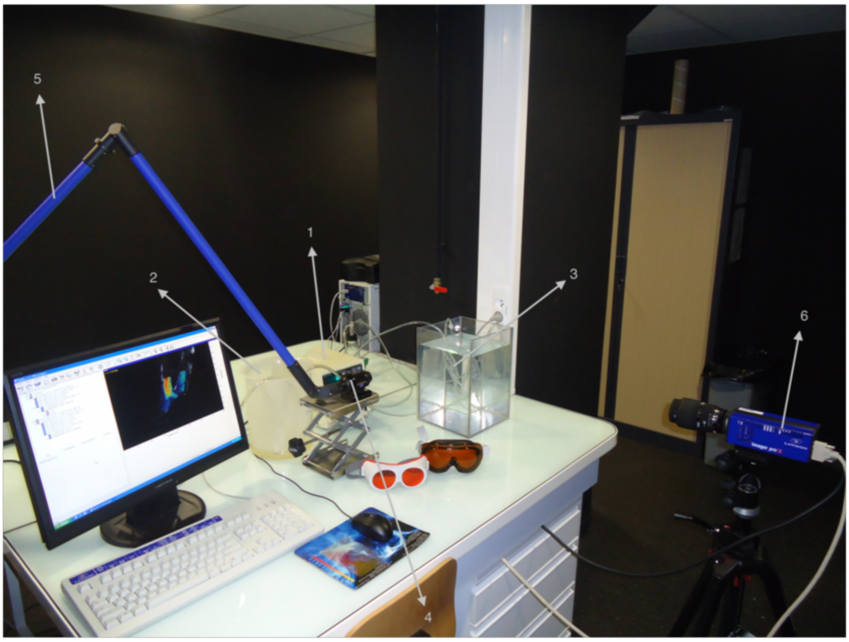

Figure 2.19: Experimental setup for the PIV measurements: (1) pump, (2) fluid, (3) AVF, (4) laser, (5) laser guiding arm, (6) camera.

3.3.1 Pump

The steady flow is provided by the peristaltic pump Easy-Load® 7518-10 from Masterflex® (Cole-Parmer Instrument Company). It can provide a constant flow rate in the range 0-1250 ml.min^{-1}. We have chosen to simulate physiological, time-averaged flow-rates that can be provided by the available pump. The arterial inlet flow-rate has been set to 800 ml.min^{-1}.

3.3.2 Fluid

All the experiences have been conducted using an aqueous glycerine solution (68% water, 32% glycerine). Its viscosity has been measured to be 3.75×10^{-3} Pa.s, and its density 1083.2 kg.m^{-3}. We seed the solution with lycopodium particles (Lycopodium, SIGMA-ALDRICH) with a concentration of 0.7 g.l^{-1}.

3.3.3 Laser

The light source is the double laser Nano S PIV Pulsed Nd:Yag from the Litron Lasers (UK) provided in the pack LaVision Flowmaster PIV System. It is powered by the LPU450-PIV twin power supplier, which drives the two laser units with a combined throughput of about 450 W. The laser system is controlled remotely via the PC ('external trig' mode). The Nano laser heads have a verified electronic intra-cavity safety shutter. It is possible to stop the laser emission by closing the shutter (`http://www.litron.co.uk/pages/nanopiv.html`).

The function of the laser is to light the field of motion of the fluid. The wavelength of Neodimium Yttrium-Aluminium-Garnet (Nd-YAG) pulsed laser beam is 1064 nm (infrared light). For PIV applications a wavelength of 532 nm (green light in the visible spectrum) is usually used. It is obtained with an appropriate crystal called 2nd-harmonic crystal. The laser beam is then transformed in a focused sheet through a system of optical lenses. This sheet is used to lighten a selected plane within the geometry [187]. For this study, a divergence lens with a focal length of -10 mm has been chosen. It has to be orthogonal to the camera, which records a sequence of double-frame (A and B) images. To ease the positioning of the laser plane, a guided arm is employed (see figure 2.19).

3.3.4 Camera

The camera used for the image acquisition is the Charged Coupled Device (CCD) camera Imager pro X 2M (LaVision). It is a high sensitivity, high resolution digital camera. The pixel resolution is 1660 x 1200 pixels, and the frame rate is 29 frames.s^{-1}. The camera is positioned orthogonally to the laser sheet, in order to minimize sources of noise and avoid blurred frames. For a better visualization of the field of motion, a 105 mm F2.8 DG MACRO (Sigma) objective is used. It allows a good focus onto the regions of interest of the AVF geometry.

3.3.5 Protocol for image acquisition and velocity vector field calculation

The image acquisition is managed in the 'external trig' mode, which means that the laser and the camera are completely managed from the PC. All the parameters for image acquisition and analysis have been defined using the software DaVis 7.2. The first operation to be performed when the software is started is the calibration of the field of view. It is done grabbing an image of the field of view in which a ruler has been inserted. A project for image acquisition is then created and the recording process is started via a dedicated panel. We set the number of acquired image pairs to 20 and the correlation technique to 'double frame'. The trigger synchronizes the laser and the camera.

We have optimized the time interval Δt between frames A and B in each region of interest of the AVF. The larger the velocity, the smaller the time interval. We have set Δt to be equal to 150 μs in the stenosis and anastomosis, and to 7000 μs for the enlarged vein.

The laser power has also been adjusted to maximize the luminosity of the reflected light without having risks of damaging the camera sensor because of excessive lightness. We have obtained the optimal intensity of light when we set 40% of the maximum power at the stenosis, 35% at the anastomosis and 38% at the vein.

Once the images are recorded, it is necessary to create a PIV project for the calculation of the velocity vectors field and import the acquired images. We created a specific user-defined mask for each region to compute the velocity vectors within the lumen. The velocity vectors are calculated with a three-pass cross-correlation algorithm. The interrogation spot is set to be circular 32×32 pixels in size. The overlap of the interrogation spots has been set to 50%.

Spurious vectors have been eliminated and replaced with the spatial-average value of the neighbours using the median filter implemented within the software. This filter computes the mean value of the velocity at the nine points of measure which are the closest to the spurious vector. We have time-averaged velocity field at each location among the 20 instant of measurement to reduce the effects of eventual artefacts, and calculated the standard deviation [187]. More quantitative date have been obtained by extracting the velocity profiles at specified cross-section locations.

Chapter 3

Simulation of the fluid-structure interactions within the AVF

In this chapter we study the fluid-structure interactions within a patient-specific arteriovenous fistula. We transcribe the text as it has been submitted to the 'International Journal for Numerical Methods in Biomedical Engineering'.

1 Introduction

Hemodialysis is conducted in patients with end-stage renal disease in order to filter blood waste products and compensate for the ill-functioning kidneys. To enable hemodialysis, a partial extracorporeal circulation needs to be set up towards the artificial kidney. It requires a permanent vascular access that is easily available for a repeated use and that provides a blood flow larger than 500 ml.min^{-1} [188, 189]. The most standard technique is to create in the arm an arteriovenous fistula (AVF) by connecting a vein onto an artery (e.g. the cephalic vein onto the radial artery in the case of an end-to-side AVF) [23]. Subjected to arterial pressure, the vein gets arterialized after three to six months [27]. Once mature, the fistula behaves as a low resistance, high compliance pathway between the high pressure arterial system and the low pressure venous system [23].

The lifespan of an AVF is limited from a few days to about 10 years because of the onset of several complications [23]. Some complications may affect directly the AVF, such as atherosclerotic plaques, stenoses or aneurysms [71, 23]. In practice, the AVF failure is caused by an insufficient or excessive blood flow inside the vein, compromising either the hemodialysis procedure [8] or the cardiac load.

Hemodynamics plays an important role in the evolution and long-term efficiency of the AVF [8]. Non-invasive *in vivo* hemodynamic measurement techniques, such as echo-Doppler, can provide averaged velocity values [190] but neither velocity profiles nor wall shear stresses (WSS). The hemodynamics inside patient-specific fistulae has previously been investigated through computational fluid dynamics (CFD) simulations [166, 170, 171]. These studies have provided a comprehensive knowledge of the spatial and temporal distribution of the hemodynamics inside the AVF and shown direct correlations between altered wall shear stress patterns and local vessel damages. They, however, assume the vascular wall to be rigid, which is not the case physiologically. No study has yet investigated the influence of the wall compliance on the hemodynamics in an AVF.

Over the last years, quite a few numerical models simulating the fluid-structure interactions (FSI) in the cardiovascular system have otherwise been developed ([191, 126, 192, 193, 194, 195, 138] among others). They are performed with a three-fold objective: to investigate how hemodynamic factors influence the onset and progression of cardiovascular diseases, to predict the outcome of surgical interventions and to evaluate the effect and efficacy of medical devices [153, 196, 197, 137]. Recently, some studies [191, 198] have started to use more elaborate vessel wall models, such as the anisotropic constitutive laws derived by the group of Holzapfel [145, 199].

Our present objective is to study the influence of the wall compliance on the hemodynamics and wall mechanics in a patient-specific radio-cephalic AVF. Our goal is to perform the FSI simulation with one of the numerical software that clinicians could use to evaluate the hemodynamic and structural conditions within the AVF during the patients' follow up. For this purpose, we have chosen to simulate the FSI with the commercial code ANSYS Workbench (ANSYS, Inc.). We have modeled the hyperelastic behavior of the vessel walls using the Yeoh constitutive law. We have made the deliberate choice not to implement more elaborate constitutive laws (e.g. [145, 199]), as they are not yet available by default in ANSYS Workbench. We have, however, differentiated the wall thickness and mechanical properties of the cephalic vein and radial artery.

In a second part of the study, we have analyzed whether it is possible to reduce the computational time of the simulation in the perspective of translating the numerical tool to clinicians. We have relaxed independently the different assumptions concerning the material properties and the strong coupling of the fluid and solid physics, and compared the results with those obtained with the more physiologically-correct model.

2 Material and Methods

2.1 Patient-specific AVF geometry and meshing

The case of study is a mature end-to-side radio-cephalic fistula. The medical images of the complete AVF lumen have been acquired by CT-scan angiography at the Polyclinique Saint Côme (Compiègne, France). During the clinical measurements, the patient was at rest in supine position.

The images have been segmented and the complete AVF lumen has been reconstructed following the method described by Kharboutly et al. [169] (figure 3.1). Throughout the paper, the subscript v stands for vein and a for artery. The AVF presents an 80%-stenosis along the proximal radial artery and an enlargement in the cephalic vein. The artery is 170 mm long and has an internal diameter of 5.95 mm at the inlet and 6.25 mm at the outlet. The outlet venous diameter is 10 mm.

The fluid mesh is generated using the software T-Grid (ANSYS, Inc.). We first mesh the lateral surface of the lumen and then generate the volume mesh of the fluid domain. The latter consists of an hybrid mesh, with prismatic cells in the boundary layer and tetrahedral cells in the vessel core (see [169] for more details on the mesh generation).

The structural part of the vessel wall is then modeled as a monolayer of discrete-Kirchhoff theory-based shell finite elements. They are four-node

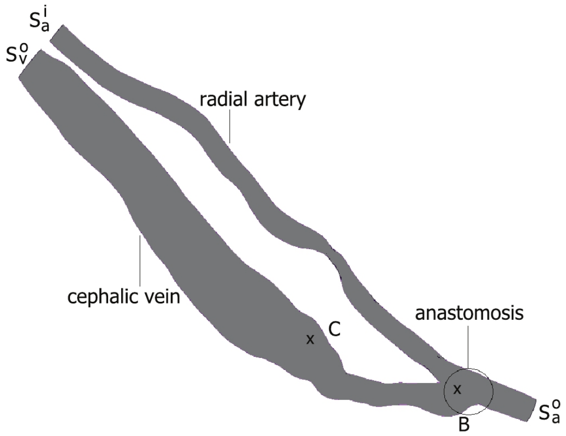

Figure 3.1: Schematics of the vascular geometry. S_a^i represents the arterial inlet, S_a^o the arterial outlet and S_v^o the venous outlet.

linear triangular shell elements. Different thicknesses have been imposed for the arterial and venous shell elements. Thickness data have been taken from the literature, as no direct measurement was possible *in vivo*. We have modeled the vein with a thickness of 0.4 mm, which is typical for a cephalic vein prior to the AVF creation. Indeed, the vein thickness tends to remain altogether constant during the fistula maturation [28]. The arterial thickness is supposed to be equal to $1/10^{th}$ of the actual inlet diameter, i.e. 0.6 mm [200]. The fluid and solid meshes share the same nodes at the interface.

We have investigated the convergence of the numerical results with the mesh spatial resolution. The convergence study, reported in Decorato et al. [201], has shown that a maximum mesh size of 4×10^{-3} mm guarantees errors below 0.8% both for the maximum velocity magnitude and WSS. This characteristic mesh size appears as a good compromise between numerical accuracy and computational time. The whole mesh is hence composed of 784×10^3 fluid elements and 89×10^3 shell elements for the walls.

2.2 Numerical method

The transient fluid-structure interactions are simulated inside the AVF using ANSYS Workbench V13.0 (ANSYS, Inc.). It couples ANSYS CFX and

ANSYS Structural implicitly [173]. The software is based on an arbitrary Lagrangian-Eulerian formulation. It uses a partitioned approach with stagger iterations within each time step. During each stagger iteration:

- The displacement vectors are transferred from the structural to the fluid solver, where the fluid problem is solved for the current time-step;
- The load vectors are then transferred from the fluid to the structural solver, where the structural problem is solved;
- The convergence of all field equations (fluid and structural) is evaluated.

Stagger iterations are repeated until all the field equations have converged and the coupling conditions are satisfied at the fluid-solid interface. The latter requires that (1) displacements of the fluid and solid domains are compatible, (2) forces acting on the interface are at equilibrium, (3) the fluid obeys the no-slip condition.

The simulations are run neglecting gravity. The reference pressure is the atmospheric pressure. As initial condition, we use the results obtained from a steady fluid-only simulation, in which we impose the time-averaged values of the velocity and pressures as boundary conditions.

We have searched for the optimal time-step for which (i) the numerical model is stable, (ii) the computational time is the smallest, (iii) the temporal resolution is sufficient to capture the time-dependent flow features. We have tested 3 time steps: 10^{-3}, $5{\times}10^{-3}$ and 10^{-2} s. We find that the simulation is unstable with the time of 10^{-2} s, but remains stable with the two smaller values. The numerical scheme is therefore conditionally stable, with a limit of stability between $5{\times}10^{-3}$ and 10^{-2} s. Reducing the time step by a factor of 5 hardly has an effect on the accuracy of the results: the results obtained with a time step of $5{\times}10^{-3}$ s differ by less than 1% from those obtained with 10^{-3} s. It, however, has a direct impact on the computational time, which increases linearly with the number of iterations. We have therefore chosen to run all the following simulations with the time step of $5{\times}10^{-3}$ s in order to optimize the computational time without loss in accuracy.

Each FSI simulation is run over six consecutive cardiac cycles. The repeatability of the results is verified after 3 cardiac cycles with cycle-to-cycle differences inferior to 1%. The results shown in the following are obtained by phase-averaging the field values over the 4^{th}, 5^{th} and 6^{th} cardiac cycles. The total simulation time is approximately 70 CPU hours on an Intel(R) Xeon(R) workstation with 64 bit CPU dual core processors of 2.67 GHz clock speed, 23.9 GB RAM memory and a Microsoft Windows XP operating system.

2.3 Blood model

Blood is modeled as an isotropic, homogeneous, non-Newtonian fluid. It is assumed to follow Casson model

$$\sqrt{\tau} = \sqrt{\tau_0} + \sqrt{\kappa\dot{\gamma}}, \tag{3.1}$$

where τ_0 represents the yield stress, $\dot{\gamma}$ the shear rate and κ the consistency. The apparent viscosity μ is obtained from equation 3.1 and can be expressed as

$$\sqrt{\mu} = \sqrt{\frac{\tau_0}{\dot{\gamma}}} + \sqrt{\kappa}. \tag{3.2}$$

The model parameters have been chosen according to experimental data obtained at low shear rates: $\tau_0 = 4{\times}10^{-3}$ Pa, $\kappa = 3.2{\times}10^{-3}$ Pa.s [175]. In section 4.1 we will compare the results obtained using Casson blood model with those predicted modeling blood as a Newtonian fluid. Blood density is set to 1050 kg.m^{-3}.

2.4 Vessel wall properties

We simulate the vessel wall hyperelasticity assuming both the artery and the vein to follow the 3^{rd}-order Yeoh model [182]. The strain energy func-

Table 3.1: Values of the constants of the hyperelastic 3^{rd}-order Yeoh model used for the radial artery and the cephalic vein

Constant	Artery	Vein
$\mathbf{C_{10}}$	0.763×10^5 Pa	3.784×10^6 Pa
$\mathbf{C_{20}}$	3.697×10^5 Pa	5.543×10^8 Pa
$\mathbf{C_{30}}$	5.301×10^5 Pa	6.491×10^9

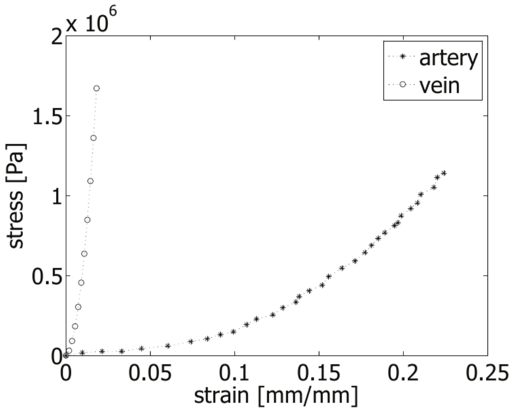

Figure 3.2: Arterial and venous mechanical properties. Data are adapted from [183] for the vein, [184] for the artery

.

tion ψ reads

$$\begin{aligned}\psi = C_{10}(I_1-3)+C_{20}(I_1-3)^2+C_{30}(I_1-3)^3+\\ D_1(J-1)^2+D_2(J-1)^4+D_3(J-1)^6,\end{aligned} \tag{3.3}$$

where I_1 is the deviatoric first principal strain invariant and J the Jacobian. The parameters are the material constants C_{10}, C_{20}, C_{30} and the incompressibility parameters D_1, D_2, D_3. The vessel wall is assumed to be incompressible (i.e. $J=1$). We have differentiated the arterial and venous mechanical properties (figure 3.2) in order to correctly model the larger compliance of the arterialized vein. The model constants, listed in table 3.1, are the ones that best fit experimental data ([183] for the vein and [184] for the artery).

2.5 Boundary conditions

All the boundary conditions imposed for the fluid and solid domains are summarized in table 3.2. For the fluid flow, we impose a time-dependent flat velocity profile V_a^i at the inlet and time-dependent pressure profiles at the arterial and venous outlets (figure 3.3). The velocity, prescribed at the inlet of the proximal radial artery (S_a^i in figure 3.1), is the one that was measured by echo-Doppler on the patient on the same day as the CT-scan angiography [170]. The imposed velocity corresponds to a systolic Reynolds number of 800, time-averaged Reynolds number of 650 and Womersley number of 4. A space-varying velocity profile following the Womersley solution [202] is recovered in the radial artery 8 diameters downstream of the inlet boundary. A fully developed profile therefore enters the stenosis, located about 16 diameters from the entrance.

The *in vivo* measurements do not provide any pressure data, as pressure measurements are invasive, but only the value of the flow split between the arterial (S_a^o) and venous (S_v^o) outlets (30%-70% respectively). In order to deduce the pressure waveforms at the outlets, we have conducted a CFD simulation using ANSYS-CFX (ANSYS, Inc.). As inlet velocity, we set V_a^i. At the two outlets, we impose a R-C Windkessel model, following the method described in Decorato et al. [201]. The values of the parameters of the Windkessel model have been calculated so that

- the flow split between the arterial and venous outlets is 30%-70%;
- the time-averaged inlet pressure $\overline{P}_a^i$ is about 70 mmHg [8].

Neither rotation nor translation is allowed at the vascular extremities of the solid domain. The external tissues are supposed to be at atmospheric pressure, which is the pressure of reference in the FSI simulation.

2.6 Wall shear stresses

The wall shear stresses are contained within the plane tangent to the vascular wall, defined by the unit vector normal to the vessel wall **n**. They can

Table 3.2: Boundary conditions imposed at the extremities of the fluid and solid domains (see figure 3.1 for the surface definitions)

Boundary	Fluid domain	Solid Domain
S_a^i	Time-dependent velocity profile V_a^i	0-translation, 0-rotation
S_a^o	Time-dependent pressure profile P_a^o	0-translation, 0-rotation
S_v^o	Time-dependent pressure profile P_v^o	0-translation, 0-rotation
Vessel wall	No-slip condition	Atmospheric pressure

be expressed by the two-component vector

$$\tau_w = \mu \frac{\partial \mathbf{v}}{\partial \mathbf{n}}, \tag{3.4}$$

where **v** is the velocity vector. We call wall shear stress WSS the modulus of τ_w. In healthy arteries, physiological values of WSS are typically 1-2 Pa [8]. The physiological range is rather 0.8-3 Pa in healthy veins [164].

The oscillatory shear index OSI

$$OSI = 0.5\left(1 - \frac{|\int_0^T WSSdt|}{\int_0^T |WSS|dt}\right), \tag{3.5}$$

where T is the time period of the cardiac cycle. The OSI index represents the degree of oscillation in the wall shear stress orientation. Its values fall in the range $[0, 0.5]$, 0 corresponding to a constant forward flow and 0.5 to a purely oscillating flow. OSI values are typically below 0.2 in healthy physiological vessels. A value of 0.3-0.35 is considered as the threshold, above which neo-intimal activation might occur [181].

The time derivatives of WSS ($WSSG_t$) are defined as

$$WSSG_t = \frac{\partial WSS}{\partial t}. \tag{3.6}$$

They are typically small in healthy vessels. We will analyze which AVF zones are exposed to non-vanishing values of wall shear stress time derivatives.

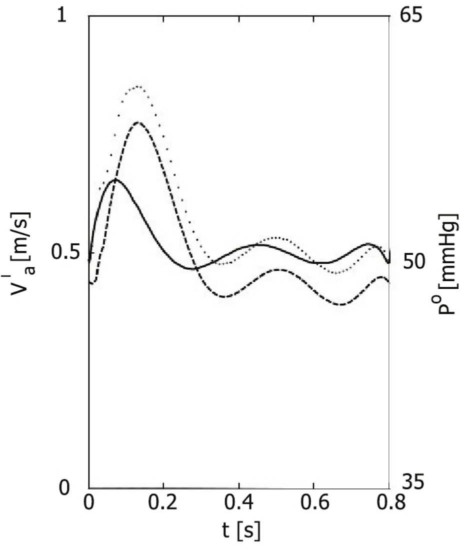

Figure 3.3: Waveforms of the inlet velocity profile V_a^i (continuous line) and outlet pressures P_a^o (dotted line) for the radial artery and P_v^o (marked line) for the cephalic vein.

2.7 Internal wall stresses

To study the stresses within the vessel wall, we consider the Cauchy stress tensor σ. The stress tensor can be reduced to its principal components σ_i ($i = 1, 2, 3$) in the principal coordinate system. We study the distribution of the maximum component of the principal stresses

$$\sigma_{max} = max_i(\sigma_i), \tag{3.7}$$

and consider its time-averaged value $\overline{\sigma}_{max}$.

3 Physiologically-correct, patient-specific FSI

3.1 Hemodynamics

The mean velocity entering the radial artery does not vary significantly over the cardiac cycle, which is typical of peripheral arterial flows: it ranges from 0.42 m.s^{-1} at peak diastole to 0.62 m.s^{-1} at peak systole. As a consequence, only moderate differences in the mean velocity are found over time across different segments of the AVF. In order to visualize the flow patterns, 31 velocity streamlines are shown at peak systole in figure 3.4 and at late

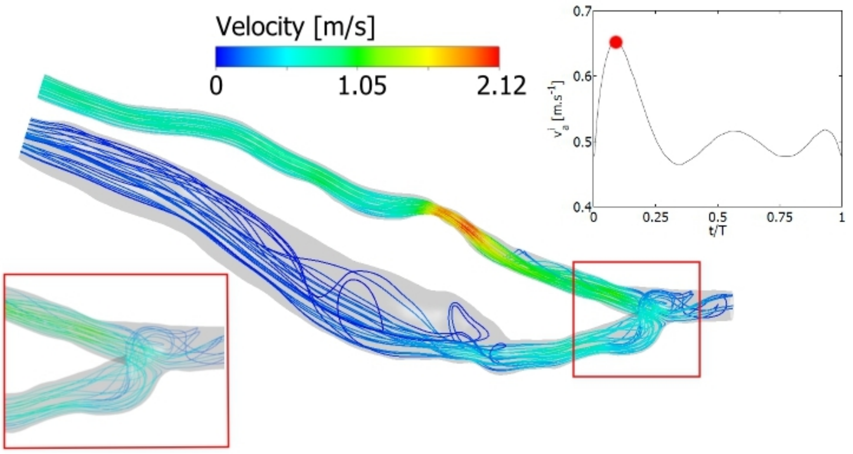

Figure 3.4: Velocity streamlines at peak systole. The time of measurement is indicated by the red dot on the inlet velocity profile. On the bottom left, a zoom on the region of the anastomosis shows that the flow impacts on the bifurcation generating a stagnation point.

diastole in figure 3.5. The stenosis causes a local increase in the flow velocity, as well as a region of recirculation downstream of it. The flow impacts on the bifurcation between the radial artery and cephalic vein, called the anastomosis, generating a stagnation point (red box in figure 3.4).

The particularity of most mature AVFs is to present an enlarged vein: it is associated with the largest zone of flow recirculation. If we compare figures 3.4 and 3.5, we observe a change in streamline distribution in the cephalic vein with a stronger recirculation motion and helical flow at late diastole (shown in cross-section A, figure 3.5).

We have analyzed the evolution of the static pressure along the vasculature. We observe a global static pressure drop between the arterial inlet and the venous outlet of 16.6 mmHg. About 70% of the pressure drop is caused by the stenosis. The vein enlargement does not lead to a significant additional pressure drop.

3.2 Wall shear stresses analysis

3.2.0.1 Wall shear stresses The *WSS* map is shown in figure 3.6. The *WSS* values fall within the healthy physiological range in the proximal radial

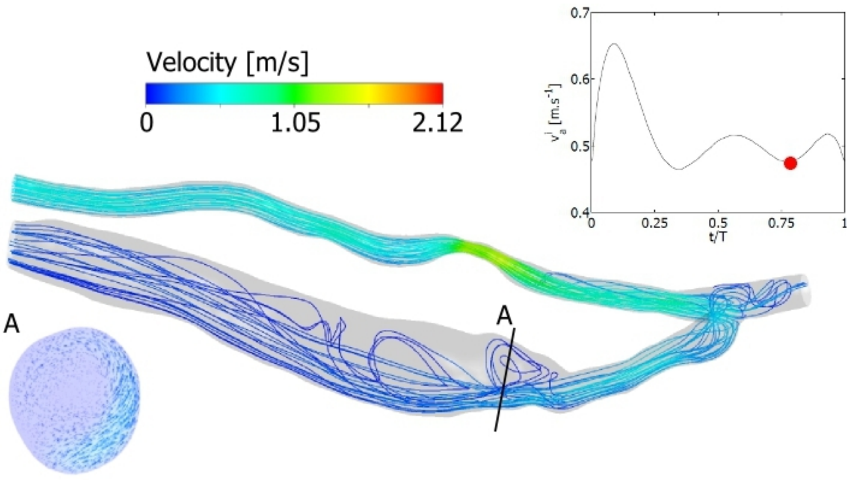

Figure 3.5: Velocity streamlines at late diastole. The red dot on the inlet velocity profile indicates the corresponding time of measurement. The bottom left insert shows the flow recirculation inside the vein (section plane A): the velocity arrows have been projected within the two-dimensional plane.

artery, upstream of the stenosis. Still the vessel tortuosity leads locally to WSS up to 10 Pa. The highest WSS is found at the level of the stenosis, where it approaches 60 Pa. The anastomosis is the other region subjected to high WSS ($\approx$ 18 Pa) especially on its venous side: it is a consequence of the incoming flow impacting onto the bifurcation. Lee and Roy-Chaudhury [56] have suggested that the large WSS lead to an increase in the oxidative stress resulting in inflammation and peri-anastomotic neointimal formation.

On the venous side, the patient presents a venous enlargement over most of the cephalic vein. This entire region is subjected to WSS generally below 0.15 Pa and OSI values larger than 0.4 (figure 3.7). The combination of extremely low WSS and high OSI values has been associated with intima hyperplasia [164].

3.2.0.2 Wall shear stress time derivatives In the case of AVF, wall shear stress time derivatives have been shown to have a larger influence than spatial gradients [203, 204]. We will therefore concentrate on WSS temporal gradient $WSSG_t$. Wall shear stress time derivatives are about nil across

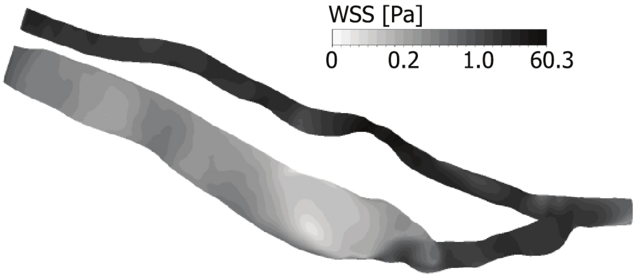

Figure 3.6: *WSS* map at peak systole. The highest *WSS* are found at the stenosis. A logarithmic gray-scale has been used to highlight the low *WSS* values calculated in the enlarged region of the vein.

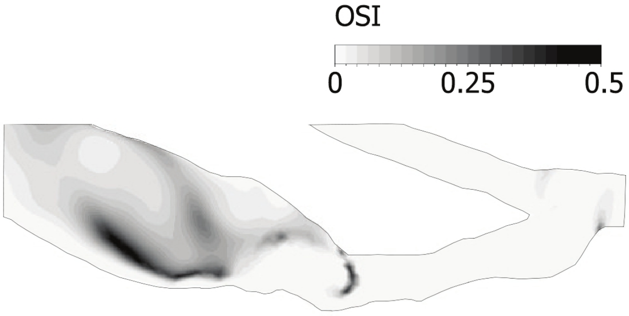

Figure 3.7: *OSI* spatial distribution in the cephalic vein.

the AVF (data not shown) apart from two locations. The region that experiences particularly high $WSSG_t$ with large temporal variations is the anastomosis (figure 3.8). The second highest value is found in the enlarged venous region, but their maximum amplitude is only 10 Pa.s^{-1} and they appear mainly in the diastolic phase of the cardiac cycle. Previous studies have associated wall shear stress time derivatives with endothelial cell proliferation and neointimal formation [204]. A thicker neointimal layer may modify the flow split in the long run by altering the vessel resistances. It could thus have large clinical consequences: on the one hand, too low arterial flow can cause necrosis of hand tissues; on the other, too low venous flow prevents the hemodialysis from taking place.

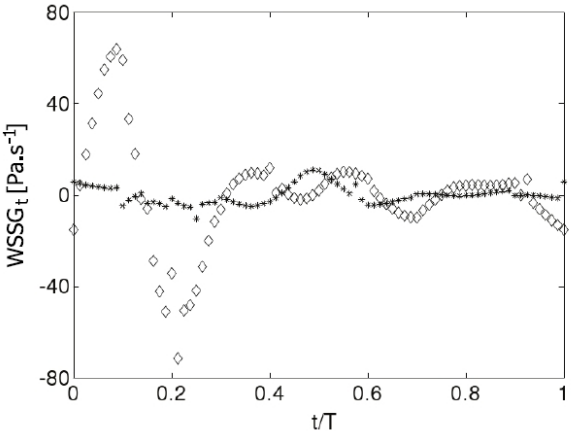

Figure 3.8: $WSSG_t$ time variation at point B in the anastomosis ($\diamond$) and point C in the vein enlargement ($*$). Points B and C are defined in figure 3.1.

3.3 Internal wall stresses analysis

The map of vascular wall displacement is represented at peak systole in figure 3.9. The maximum displacement in the artery is 0.62 mm, which corresponds to a maximum strain of 14%. On average the strain in the artery is of the order of 10%. It is about eight times smaller in the vein, which is a consequence of the larger stiffness of the venous wall. In the vein, the maximum displacement is only about 0.05 mm, (maximum strain of 3%). We have analyzed the corresponding values of the maximum component of the principal stresses $\overline{\sigma}_{max}$ at the vascular wall at peak systole (data not shown in a graph). They fall in the range 5.5-7.0 kPa inside the artery, with a space-averaged value of 5.7 kPa. Within the cephalic vein they are equal to 8.0-13.5 kPa with a space-averaged value of 11.5 kPa.

We hypothesize, based on the results of previous studies [205, 206, 207], that healthy large vessels remodel their internal structure to achieve a quasi-uniform internal stress of constant value. To determine this baseline stress value, we have considered the part of the radial artery located 8 to 16 diameters from S_a^i, i.e. where the flow is fully-developed and unperturbed by the stenosis. This region is also the least influenced by the existence of the anastomosis. Figure 3.10 shows the internal wall stresses normalized by the baseline stress. Results show that the stresses inside the

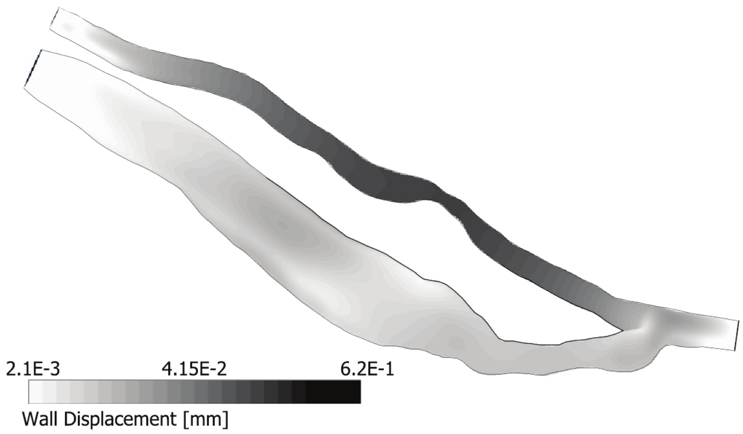

Figure 3.9: Spatial distribution of the vascular wall displacement. The map is shown in a logarithmic scale.

venous wall are, on average, larger than their baseline value by a factor of 2 and that they can be up to 2.4 times larger.

Non-physiological internal wall stresses can generate wall remodeling through their impact on smooth muscle cells: the cells are responsive to the level of stresses and modulate their migration rate, proliferation and synthesis of collagen [208, 205, 209]. One limitation that we face to analyze the present results is that most of the research on wall remodeling has been conducted in arteries, which are muscular vessels. Less is known on the remodeling of veins. Still the last four decades of clinical practice of AVF prove the high capability of remodeling of veins under increased hemodynamic stresses, since veins are able to get arterialized over a period of 3-6 months [27, 28]. We presently find non-nominal values of internal wall stress in the cephalic vein, which would indicate that the vein continues its remodeling. This perpetuation of the phenomenon could result in excessive wall remodeling downstream of the anastomosis and explain the enlargement of the vein.

3.4 Discussion on the FSI simulation

In this section we have modeled the fluid-structure interactions in a patient-specific AVF geometry, taking into account the physiological non-linearities

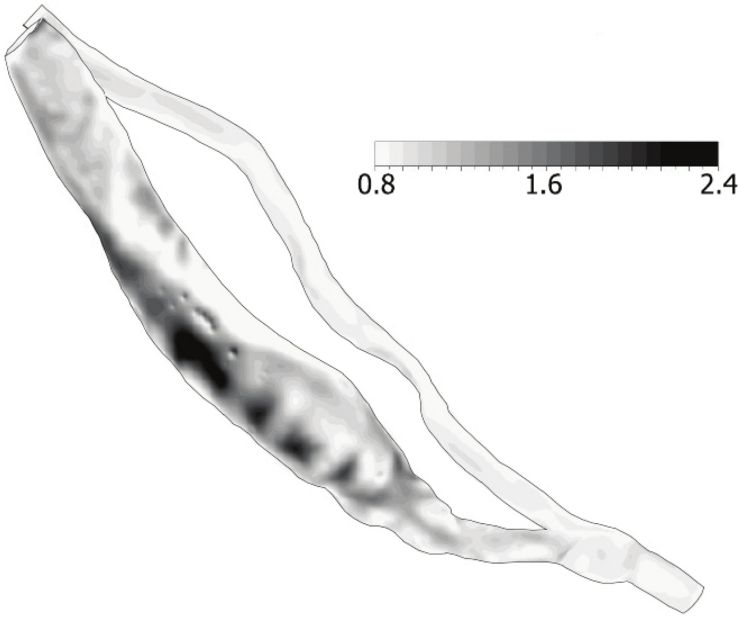

Figure 3.10: Spatial distribution of the internal wall stresses $\overline{\sigma}_{max}$ normalised by the baseline stress.

in the material properties. We have proven that it is feasible to solve the multi-physics numerical simulation using the commercial environment provided by ANSYS, Inc. We have differentiated the venous and arterial mechanical properties in order to obtain realistic results for the internal stresses in the vascular wall. We have shown that the venous shear and internal stresses both differ from their baseline values and that the vein is likely to continue remodeling its wall internal structure.

Setting relevant mechanical properties for the different vessel portions has proven to be challenging due to the lack of available data in the literature. It is known that the vein is subjected to a significant increase in stiffness as a consequence of the fragmentation of the elastin content and increase in collagen content, as the vein enlarges [28, 210]. But few quantitative data exist as reported in the introduction. Similarly, it has not been possible to take into account the presence of external tissues to the AVF: no study has yet characterized the mechanical properties of the tissues below the elbow region.

4 Relaxation of various hypotheses in the simulation

In the previous section, we have shown that although feasible, a coupled fluid-structure simulation is highly challenging and results in large computational times. The calculation takes 70 CPU hours to run on 4 cores. The objective is to eventually translate the simulation tool to clinicians, but a routine use will not be possible in practice if the computational time is not reduced. In this section we investigate whether it is possible to reduce the computational time by relaxing some of the hypotheses, while maintaining the clinical relevance of the simulation. We will compare the physiologically-correct model (section 3) with simulations assuming first blood to be Newtonian and secondly the vessels to have uniform properties (same thickness and mechanical properties all along the vasculature). We will then evaluate the accuracy of uncoupled fluid or structural simulations.

4.1 Comparison between Newtonian and non-Newtonian blood modeling

Blood is a non-Newtonian fluid, but in some cases its non-Newtonian behavior can be neglected. Blood behaves like a Newtonian fluid under large shear rates (≥ 300 s^{-1}). This is typically the case in arteries with a diameter larger than 0.5 mm. A shear rate value of 100 s^{-1} has been identified as the threshold below which non-Newtonian effects need to be modeled, but they begin to be significant for shear rates $\dot{\gamma} \leq 300$ s^{-1}.

From a numerical point of view, the main problem of implementing a non-linear Casson model is the numerical instability that it induces. But once the non-Newtonian simulation is rendered stable, its computational time is comparable to that of the Newtonian case.

We have run a new simulation, in which blood is set to be Newtonian with a dynamic viscosity $\mu = 3.2 \times 10^{-3}$ Pa.s (same value as that of the Casson model at large shear rates). All other parameters of the simulation are otherwise identical to the physiologically-correct one (section 3).

In the patient-specific case, we observe a maximum shear rate inside the cephalic vein of 90 s^{-1}. At the anastomosis level, the maximum shear rate is 190 s^{-1}, and inside the radial artery it is 300 s^{-1}. If we assume blood to be Newtonian, the WSS values are increased by 13% on average in the cephalic vein (20% at maximum) and 10% at the anastomosis (15% at maximum). These results are in agreement with those found by Kabinejadian and Ghista [176].

The present comparison indicates that non-Newtonian effects are important on the venous side, because of the low shear rate values. These results prove that the Casson model is necessary if one is interested in the quantification of the WSS distribution downstream of the anastomosis. It is, however, not needed to estimate the hemodynamics in the radial arterial. Needless to mention that the rheological model hardly has any influence on the wall internal stresses.

4.2 Comparison between the reference case and a homogeneous wall model

Differentiating arterial and venous wall properties substantially increases the time of preparation of the simulation and therefore the probability to introduce numerical errors. It indeed requires to segment the vascular geometry into different sub-parts, to which different properties are assigned. In order to ensure the numerical stability, one also needs to guarantee the correspondence of the boundary nodes between the segmented parts and their connection during the simulation.

In this sub-section, we aim at estimating the error on the hemodynamics and wall mechanics, if one models the vessel wall with uniform properties. A new simulation is run imposing the entire vascular wall to have the arterial geometrical and mechanical properties described in section 2.4. Blood is still supposed to follow the Casson model. The same fluid and solid mechanics boundary conditions are imposed as for the reference case (section 3).

Comparing the overall hemodynamic conditions predicted by both simulations, we only observe small differences. The error on the flow rate entering the cephalic vein at the anastomosis is inferior to 1% and no difference is calculated on the venous wall shear stresses. The maximum error is found on the hemodynamic conditions predicted at the stenosis: the uniform wall simulation overestimates the WSS by 14%, and underestimates the stenosis pressure drop by 7.5% (table 3.3). The latter is shifted in time and occurs at $t/T = 0.25$ instead of $t/T = 0.15$ in the reference case. This is a consequence of the smaller venous compliance.

More significant is the effect on the internal maximum principal stresses. When one models the vein with a compliance and thickness identical to the arterial one, one obtains non-dimensional internal stresses close to 1: they appear to be in the physiological range. We have independently studied the influence of wall thickness and seen that its contribution is negligible on the hemodynamics and weights for less than 2% on the maximal wall internal stresses values (data non shown). We conclude that it is necessary to impose wall properties that are as realistic as possible in order to properly estimate the risk of perpetuation of wall remodeling in the vein clinically. This is important, all the more so as it does not increase the computational time.

The main limitation of this conclusion is the difficulty in estimating the actual venous wall properties: the tissue is that of a vein subjected to arterial hemodynamic conditions. It is impossible to infer its properties from measurements on other venous tissues. Furthermore, the vein appears to be in constant remodeling, suggesting that its properties evolve over time.

4.3 Comparison between FSI and uncoupled fluid or structural simulations

To quantify the influence of wall compliance on the hemodynamics, we have conducted a CFD simulation using the fluid solver ANSYS CFX (ANSYS, Inc.). The rigid wall CFD simulation has been performed using the same settings for ANSYS-CFX as in the FSI simulation, but deactivating the multifield coupling. In particular we have imposed the same boundary

Table 3.3: Comparison of the results provided in the reference case and in the case of homogeneous wall properties at peak systole.

Parameter	Reference Case	Homogeneous Wall
Velocity at stenosis	2.12 $m.s^{-1}$	2.11 $m.s^{-1}$
WSS at stenosis	60.3 Pa	69.2 Pa
$\overline{\sigma}_{max}$ normalised by baseline stress	≈ 2	≈ 0.9

conditions described in section 2.5 and similarly assumed blood to follow the Casson model.

Comparing the two simulations, we notice that the local velocity and WSS values are globally overestimated by the CFD study. The largest differences found at peak systole are indicated in table 3.4. The rigid-wall simulation overestimates the peak velocity at the stenosis by $\approx$ 20% and the peak WSS values by $\approx$ 15%. The differences are, however, of a much smaller extent ($\approx$ 2%) in the zones of low velocity and WSS. The flow distribution across the two exits is well predicted (error $\leq$ 2%).

Although the quantitative data fail in accuracy, the CFD simulation provides a coherent qualitative picture of the hemodynamic conditions that prevail in the vasculature. It gives sound predictions for the zones dominated by low hemodynamic conditions. These zones have a high clinical relevance, since they are prone to complications, such as neo-intimal formation. Another advantage is the computational time, the rigid-wall simulation running twelve times faster than the fully-coupled FSI.

We have independently run a structural static simulation (ANSYS-Structural; ANSYS, Inc.). Instead of running the simulation with a two-way coupling as for the FSI simulation, we have presently used a weak one-way coupling. This method enables to impose the distribution of pressure at the AVF internal vessel walls calculated by the CFD simulation at a given instant of time. We have run the structural simulation with the peak systolic pressure field as lateral boundary condition. All the other bound-

Table 3.4: Comparison of the results provided in the reference case (FSI simulation) and in the rigid-wall case (CFD simulation) at peak systole.

Parameter	FSI	CFD
Velocity at stenosis	2.12 m.s^{-1}	2.52 m.s^{-1}
***WSS* at stenosis**	60.3 Pa	69.3 Pa
Flow rate percentage in cephalic vein	$\approx 70\%$	$\approx 68\%$

ary conditions are kept unchanged. The analysis of the wall displacement and internal constraints show that the difference with the reference case at peak systole is below 1% all along the vasculature. The structural simulation therefore predicts the results very accurately. It, however, cannot provide directly the time-evolution of the wall displacement and stresses. Like for the CFD simulation, the computational time is drastically reduced: the structural simulation runs in only one hour.

5 Conclusions

We have performed an FSI numerical simulation in a patient-specific AVF, modeling the vessel wall with non-uniform hyperelastic properties and the non-Newtonian behavior of blood. Such a simulation is challenging because of the large region of interest, the non-linear effects of the fluid and solid constitutive laws and the instabilities of the FSI coupling. In order to evaluate the importance of taking all these factors into account, we have compared the results with simplified versions of the simulation.

Our results confirm that AVFs are subjected to complex hemodynamics. The enlarged portion of the cephalic vein is subjected to *WSS* smaller than a tenth of the physiological values and *OSI* larger than 0.4. It also experiences non-zero time derivatives of WSS. The anastomosis is subjected to a stagnation point flow along with high time derivatives of WSS. These regions are therefore the more likely to suffer from intima hyperplasia.

The simulation has shown that the cephalic vein is conjointly subjected to internal wall stresses that are about the double to their baseline level. This condition is likely to promote continuous remodeling of the wall internal structure and therefore represents a risk of AVF failure.

Comparing the results with simplified versions of the simulation brought various conclusions:

- A non-Newtonian blood model is needed to predict the hemodynamics in the venous part of the AVF, owing to the low values of shear rates. The Casson model is, however, not useful on the arterial side.
- The use of homogeneous wall properties simplifies the preparation of the model, but does not provide a significant gain in computational time. It, however, significantly underestimates the internal wall stresses. When simulating the FSI in an AVF, one needs to take into account the very different wall properties of the venous and arterial parts of the vasculature. Such an issue will also come into play for other vascular diseases that profoundly alter the vessel mechanical properties over an extended region.
- Although the CFD simulation generally overestimates velocities and wall shear stresses, it still gives an informative map of the regions affected by wall shear stress values, which can lead to neointimal formation.
- A one-way coupling structural simulation provides the precise distribution of internal wall stresses, but only at one instant of time. It does not provide the time evolution of the stress distribution.
- Running an uncoupled fluid and structural simulation has the advantage to run significantly faster than the FSI simulation (15 hours instead of 70).

One issue that has been faced in the present study is the lack of data on the mechanical properties of vascular tissues. In the future, it would be interesting to device new techniques to characterize the tissues in vivo non invasively. This is a necessary step for clinicians to one day fully rely on the results of numerical simulations in the making of therapeutic choices.

Chapter 4

Simulation of the treatment by balloon angioplasty of a stenosed AVF

In this chapter study the effects of the endovascular treatment of a stenosed AVF by balloon-angioplasty. We transcribe the text as it has been submitted to the journal 'Cardiovascular Engineering & Technology'.

1 Introduction

Hemodialysis is one of the treatment options adopted for end-stage renal disease patients. It involves filtering blood waste products through a partial extracorporeal circulation. Blood is circulated through the artificial kidney up to three times a week, for which a permanent vascular access must be created. The most common approach is the suturing of a vein onto an artery in an autologous side-to-end arteriovenous fistula (AVF) [23]. The fistula is preferably created in the forearm, as radio-cephalic AVF tend to be less subject to complications than more proximal AVF, such as the brachio-cephalic AVF [211]. Autologous fistulas need three to six months to mature [27], during which period the vein dilates and the wall collagen content increases [28]. The fistula acts as a short-cut between the high pressure arterial vasculature and the low pressure venous tree. This pathway is characterized by a low resistance and a high compliance [23].

The lifespan of an AVF is limited from a few days to about 10 years because of the onset of several complications [23]. Atherosclerotic plaque formation, which is typically associated with thrombosis, stenosis formation either upstream or downstream of the junction and aneurysm formation have all been observed [23, 71]. Stenoses affecting the vein have been reported in 10-20% of patients [23]. They directly compromise the hemodialysis treatment, by reducing the venous blood flow [8]. Arterial stenoses are rare in patients with a brachio-cephalic fistula (0-4% of occurrence) but their incidence is greater in patients presenting a radio-cephalic AVF at around 30% [75]. Relatively little is known about arterial stenoses, but they can lead to a steal syndrome and increase the risk of cardiac failure in the mid-long term [8, 72].

Venous stenoses are detected owing to the changes they induce on hemodialysis parameters. The venous flow-rate can indeed be reduced to values below 100 ml.min^{-1} [8]. No technique exists so far to detect arterial stenoses. Their localization therefore requires a dedicated imaging exam, which is not routinely performed at present. Duplex ultrasound scanning is advised to be used as it is more accurate than angiography [76].

Several treatments exist to prolong the AVF functionality and reduce the associated risk of thrombosis [8]. In clinical practice, a stenosis is treated when more than 50% of the arterial lumen is compromised [74] or when it leads to a pressure drop larger than 5 mmHg (10 mmHg for peripheral veins) [59]. Although these criteria are well assessed for venous stenoses, they are still under discussion for arterial stenoses. The lumen criterion is considered to be universally valid [59] but less can be said about the optimal pressure drop across an arterial stenosis.

The treatment of a stenotic lesion can either be surgical or endovascular, the former being more invasive and usually performed when the vascular anatomy is likely to affect the success rate of the endovascular procedure [8]. As endovascular treatments radiologists can perform balloon-angioplasty with or without stenting. Angioplasty consists in the inflation of a non-compliant balloon to restore the stenosed vessel patency. It can be combined with the positioning of a metal stent. The latter is currently used in case of failure of the simple angioplasty. The efficacy of stenting is based on clinical experience and is still controversial. The use of stenting has been questioned since the late 80s [65], and has only recently been proven to be more effective than the simple balloon-angioplasty [62]. Nevertheless, in clinical practice balloon angioplasty remains commonly the most used endovascular treatment. After treatment, the diameter at the stenosis throat is rarely restored to its physiological value, and a residual stenosis remains. Treatment is considered successful when the degree of residual stenosis is below 30% [8, 72, 59, 62].

One of the reasons for the lack of more rigid guidelines for the treatment of stenosed arteriovenous fistulas is the difficulty associated with obtaining patients' hemodynamic data through non-invasive, routine exams. Computational fluid-dynamic (CFD) simulations have the potential to provide information and have been reported to be effective in the evaluation of hemodynamics [166, 170, 171]. However, to the author's knowledge, but no study has yet considered the case of a stenosed AVF. In the present study, the hemodynamics inside a patient-specific AVF presenting a stenosis inside the afferent artery is computed. The treatment of the stenosis by balloon-angioplasty is simulated with varying pressures used to inflate the balloon. We simulate the hemodynamics for degrees of residual stenosis are obtained ranging from 0 to 30%.

2 Material and methods

2.1 Geometry and mesh

The investigated vasculature consists of a mature side-to-end radio-cephalic AVF. The vascular lumen was segmented and reconstructed from computed tomography (CT) scan angiography images [170]. The images were obtained on a patient that was at rest in supine position at the Polyclinique St Côme (Compiègne, France). The patient-specific vascular geometry presents an 80% stenosis on the arterial side as indicated in figure 4.1a.

The patient-specific lumen is meshed starting from the triangulation of the lateral face of the reconstructed AVF lumen. The mesh is made of an hybrid grid created in ANSYS T-Grid. We firstly mesh the boundary

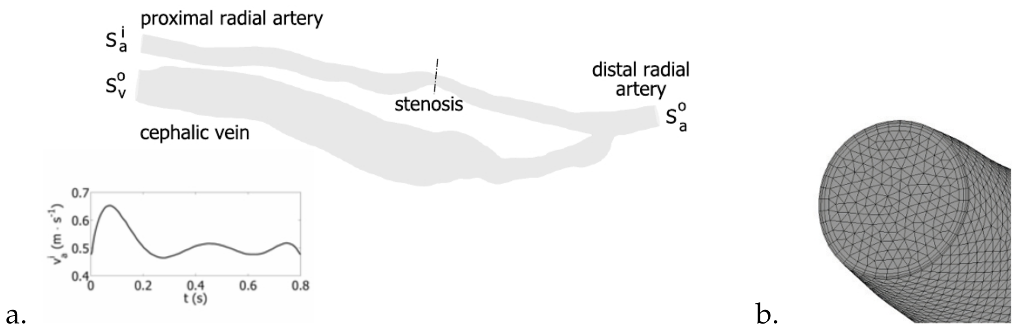

Figure 4.1: a) Reference case geometry. The surface S_a^i is the arterial inlet section, S_a^o the arterial outlet section and S_v^o the venous outlet section. The dotted line indicates the cross-sectional plane at the stenosis throat. The velocity waveform v_a^i set at the arterial inlet (S_a^i) has been measured on the patient by echo-Doppler. b) Magnification of the mesh at the distal arterial outlet (S_a^o).

layer with 7 layers of prismatic elements of decreasing thickness along the radius. We then mesh the core with tetrahedrons (figure 4.1b). Both cell element types are linear.

Different mesh sizes are tested in order to guarantee a maximum error of 1% on the velocity magnitude and wall shear stresses and acceptable computational time t_{comp}. We have investigated meshes of maximum element length Δl_{max} equal to 1, 2, 4, 5, 7 and 10×10^{-3} mm. The results obtained with the smallest mesh size (10^{-3} mm) are used as reference. In general, we define the relative error ε_u on the quantity u as $|u - u^{ref}|/u^{ref}$. We calculate the relative error for u equal to v_{max} the maximum amplitude of the velocity vector $\mathbf{v}$, which occurs at the stenosis, and $\overline{WSS}$, the time-averaged wall shear stress. The wall shear stress WSS is defined as the modulus of the two-component vector

$$\tau_w = \mu \frac{\partial \mathbf{v}}{\partial \mathbf{n}}, \tag{4.1}$$

where τ_w is the viscous stress acting tangentially to the vessel wall and $\mathbf{n}$ the unit vector normal to the vessel wall. The time-averaged wall shear stress is defined as

$$\overline{WSS} = \frac{1}{T} \int_0^T |WSS| dt, \tag{4.2}$$

where T is the period of the cardiac cycle. Figure 4.2 shows that the numerical procedure converges as Δl_{max} to the power 4.8 and that the normalized computational time decreases about linearly with Δl_{max}. In this study the simulations are run with the mesh characterized by a maximum element length of 4×10^{-3} mm, since it respects the 1%-error limit (horizontal line in figure 4.2a) for both the velocity and wall shear stress and runs four times faster than the reference case. The total number of elements used presently for the patient specific geometry is then 7.84×10^5. A magnification of the mesh at the distal arterial outlet (S_a^o) is shown in figure 4.1b.

The vascular wall is modeled as a monolayer of shell elements. It is meshed with discrete-Kirchhoff theory-based, four-node linear-triangular shell finite elements. The fluid and solid domains share the same nodes at the interface. The solid mesh consists of 8.9×10^4 shell elements. Prior to meshing, the AVF wall is divided in three zones in order to impose different mechanical properties to the healthy artery, the stenosed arterial portion and the vein.

2.2 Numerical method to simulate balloon-angioplasty

The treatment by balloon-angioplasty is simulated numerically using ANSYS-Structural (ANSYS, Inc.). A balloon is positioned at the stenosis; it is inflated and deflated by imposing an internal pressure in an implicit structural simulation. The simulation is conducted with the Lagrangian multiplier-based mixed u-P formulation.

The balloon is modeled as a cylinder with linear elastic mechanical properties. It is created as a separate body using ANSYS FE-Modeler (ANSYS, Inc.). It is positioned at the center of the stenosis, as shown in figure 4.3a.

The healthy artery is assumed to follow a hyperelastic, Fung-type law. The law constants are chosen to best-fit experimental data for healthy arteries [184]. The stenosed part is modeled with a viscoplastic law, which is based on the Maxwell model in ANSYS. At small deformations it has the same stiffness as the healthy arterial parts in order to ensure the me-

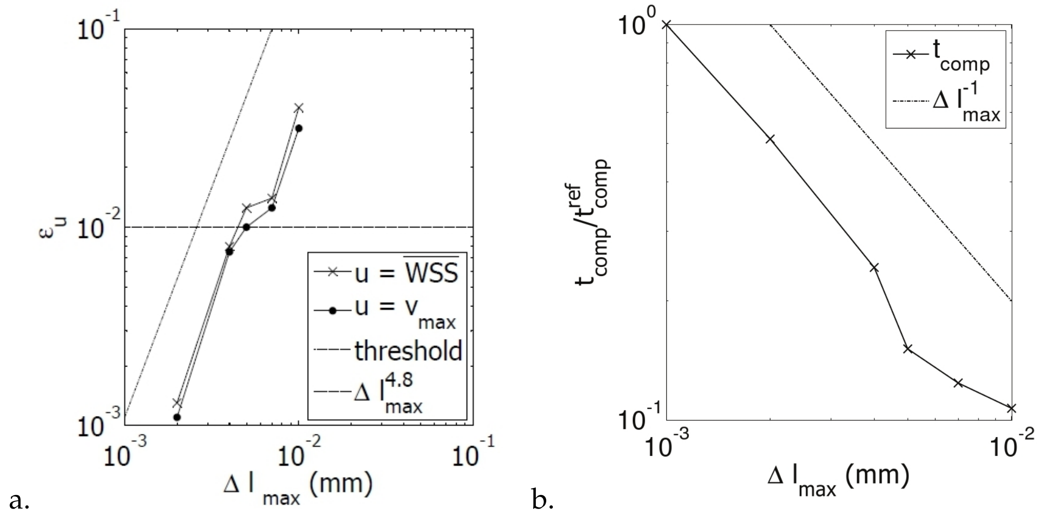

Figure 4.2: (a) Relative error on the maximum velocity ($\varepsilon_{v_{max}}$) and time-averaged wall shear stresses ($\varepsilon_{\overline{WSS}}$) as a function of the maximum mesh length Δl_{max}. The horizontal line indicates an error of 10^{-2}, chosen as the threshold. (b) Normalized computational time t_{comp}/t_{comp}^{ref} as a function of the maximum mesh length Δl_{max}. The reference case corresponds to the mesh with a maximum element length of 10^{-3} mm.

chanical continuity at the interface between the two segments. At large deformations we have set the parameter values in order to fit the data of Maher *et al.* [185].

Neither translation nor rotation is allowed at the extremities of the balloon and vessel walls. At the beginning of the simulation the balloon is not in contact with the artery (figure 4.3a). The balloon is inflated and deflated by an increasing/decreasing linear ramp in pressure. Figure 4.3b shows when contact occurs between the balloon and arterial wall. The contact problem is solved using the augmented-Lagrange method; it is supposed to be frictionless [146]. The balloon is further inflated until the maximum pressure is reached (figure 4.3c). It is then deflated, leaving the vessel wall in its post-treatment configuration (figure 4.3d). Different values of the balloon pressure are imposed (6, 5.6, 5.1, 4.7 bar). They respectively lead to a degree of residual stenosis equal to 0, 10, 20 and 30% after angioplasty (figure 4.3e).

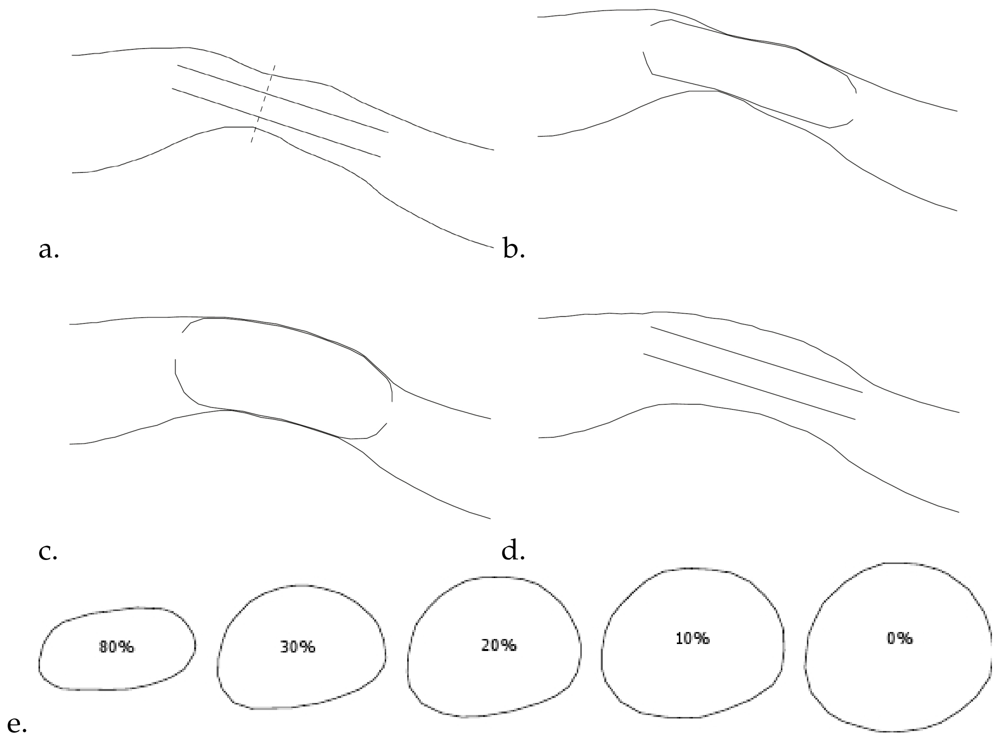

Figure 4.3: Schematics of the numerically-simulated angioplasty procedure. a) Initial configuration: positioning of the balloon within the artery. The plane indicates the stenosis throat. b) Configuration when the balloon comes into contact with the artery. c) Configuration at maximum balloon internal pressure. d) Vessel final shape when the balloon is completely deflated. e) Vessel cross-sections at the throat (plane indicated in figure 4.3a) of the stenosis for the patient-specific (80%-stenosis) and treated geometries (30, 20, 10, 0% residual stenosis).

2.3 Numerical method to simulate the hemodynamics inside the AVF

ANSYS-CFX (ANSYS, Inc.) is used to solve the continuity and momentum equations in their conservative convection-diffusion form [173]. These equations are solved implicitly with the Rhie-Chow interpolation method [174]. We use the high-resolution, second-order backward Euler scheme implemented in ANSYS-CFX fluid solver (ANSYS, Inc.). This scheme is a second-order accurate, implicit time-stepping scheme, recommended for non-turbulent flow simulations [173]. The system of algebraic equations is solved iteratively using a time-step Δt equal to 5 ms. At each time step, the residual is calculated and reported as a measure of the overall conservation of the flow properties. The maximum residual allowed is 10^{-4}. Convergence is verified in less than 10 sub-iterations at the first time step and in less than 5 iterations at all the following time steps.

Blood is assumed to be an isotropic, homogeneous, non-Newtonian fluid. The choice of the non-Newtonian model is justified by the low shear rate conditions that prevail inside the cephalic vein: in this region, the wall shear stresses would be overestimated by a Newtonian model. Its apparent viscosity μ is assumed to follow the Casson model. The apparent viscosity μ can be expressed as

$$\sqrt{\mu} = \sqrt{\frac{\tau_0}{\dot{\gamma}}} + \sqrt{\kappa}. \tag{4.3}$$

where τ_0 represents the yield stress, $\dot{\gamma}$ the shear rate and κ the consistency. Blood density is set to 1050 kg.m^{-3}. The model parameters have been chosen according to experimental data obtained at low shear rates: $\tau_0 = 4 \times 10^{-3}$ Pa, $\kappa = 3.2 \times 10^{-3}$ Pa.s [175].

The velocity field is initialized with the solution of the steady-state simulation. In this simulation the fluid properties are kept identical. As boundary conditions, we impose the time-averaged values of the inlet velocity at S_a^i and of the venous and arterial pressures at S_v^o and S_a^o, respectively. In all the simulations the atmospheric pressure is set as the reference pressure.

2.4 Boundary conditions

The time-dependent velocity v_a^i set at the arterial inlet S_a^i is the one measured on the patient by echo-Doppler in the proximal radial artery (figure 4.1a). It is imposed as a flat velocity profile. This velocity corresponds to a time-averaged inlet flow rate $\overline{Q}_a^i$ of 1.1 $\mathrm{l.min}^{-1}$. At each of the two outlets S_a^o and S_v^o, a flow-dependent pressure condition based on a RC Windkessel model is imposed [177]. This model is based on the hypothesis that the hemodynamic behavior of the vessel network downstream of the 3D-geometry outlet is related to its compliance and resistance. If one models the vessel compliance as a capacitor and the hydraulic resistance as an electrical resistance, one can generate a zero-dimensional model of the flow through the network based on a simple electrical analog circuit.

The behavior of the downstream vasculature is presently modeled with a capacitor C in parallel with a resistance R. The relationship between the blood flow rate Q and the pressure P is given by the equation

$$\frac{\partial P}{\partial t} = \frac{Q - \dfrac{P}{R}}{C}. \tag{4.4}$$

The equation is discretized using a first order scheme.

In order to estimate the parameters R and C, we use the model by Molino *et al.* [178]. It requires to know

- the pulse pressure, defined as the difference between the systolic pressure P_s and the diastolic pressure P_d at the considered outlet within one cardiac cycle;
- the time-averaged pressure $\overline{P}$ at the flow outlet;
- the time-averaged blood flow rate $\overline{Q}$ at the same flow outlet.

From the flow rate data measured by echo-Doppler, we obtain the time-averaged flow rate. Neither the pulse pressure nor the time-averaged pressure can be measured directly on the patient. In order to calculate the pulse pressure $P_s - P_d$ we run a rigid-wall simulation where the desired flow split between the arterial and venous outlets is imposed and free pressure outlet conditions are set at sections S_o^a and S_o^v. We find a pulse pressure equal to 12 mmHg. The same simulation returns also the value of the pressure drop within the AVF geometry for the imposed flow inlet. According to the literature, functional fistulas may have a mean pressure in the proximal radial artery between 50 and 100 mmHg [179]. The range of values is large, since it is a function of the patient general health conditions. To cover the entire possible range, we have run 3 simulations with different time-averaged inlet pressures $\overline{P}_a^i$ (table 4.1). For each value of $\overline{P}_a^i$, we have estimated the corresponding values of $\overline{P}_a^o$ and $\overline{P}_v^o$. At this stage, we have an estimation of the mean pressure, the pulse pressure and of the flow rate at each outlet. We can therefore apply the model of Molino *et al.* [178] to our data. The values of the constants R and C are calculated for both the arterial (denoted by subscript a) and venous (subscript v) outlets of the considered domain (table 4.1).

No data exists in the literature on the pressure and flow conditions in fistulas that could help compare the present R and C constants calculated for the segments downstream of the arterial and the venous outlets. Values can be calculated in the healthy case from the data provided by Westerhof [177] for comparison. The present values are of the same order of magnitude as in the healthy case. At the venous outlet the constant C tends to be larger but by maximum an order of magnitude, and the R values only slightly smaller. Conversely, at the arterial side the constant C is about 5 times smaller than in the healthy case and the value of R increases up to 8 times the healthy case values.

It is also interesting to consider the product of the two constants $\tau = RC$, which is the time constant of the dynamic response of the vascular tissue. It is linked to the capacity of the vascular segment to absorb the peak systolic kinetic energy. We find a time constant τ equal to 0.15 s for the arterial outlet and 0.08 s for the venous one in the case $\overline{P}_a^i = 70$ mmHg. It is coherent to find a larger time constant downstream of the artery, owing to the presence of more elastic vessels downstream of the outlet and of

Table 4.1: Values of the venous and arterial resistances (R_v and R_a) and compliances (C_v and C_a) for the different values of time-averaged inlet pressure $\overline{P}^i_a$. The corresponding inlet pressures at peak systole $P^i_{a_s}$ and diastole $P^i_{a_d}$ are provided for reference. The pressures values are in mmHg, the resistances in $10^8 kg.m^{-4}.s^{-1}$ and the compliances in $10^{-11}\ kg^{-1}.m^4.s^2$.

$\overline{P}^i_a$	$P^i_{a_s}$	$P^i_{a_d}$	R_a	C_a	R_v	C_v
55	63	51	11.9	4.98	4.77	11.5
70	78	66	30	5	6.5	12
90	98	86	41	5.04	7.4	12.1

the capillary bed. In large elastic arteries, the time constant is of order 1: Ismail *et al.* [180] found, for instance, $\tau \sim 1$ s for the vascular network downstream of the iliac arteries. This is coherent, since the arterial outlet of the AVF is made of less elastic vessels than those at the outlet of the iliac arteries.

The same R and C values are used for all the simulations, both before and after the treatment by angioplasty. The post-angioplasty simulations therefore model the situation shortly after treatment, before the occurrence of any physiological adaptation in the distal circulation.

2.5 Hemodynamic parameters

In order to evaluate the hemodynamic risk associated with a stenosed AVF, clinicians use the pulsatility index (PI), which is estimated from the patient blood velocity profile [26]. It is defined as

$$PI = \frac{v_s - v_d}{\overline{v}}, \tag{4.5}$$

where v_s is the peak systolic velocity, v_d the late diastolic velocity and $\overline{v}$ the time-averaged velocity. Clinically, an increased PI value can indicate a possible complication at the fistula [26]. This index has proven to help in the detection of venous stenoses. Fistulas without a venous stenosis have a reference PI value around 0.4 [23].

The use of CFD simulations makes it possible to also evaluate the classical hemodynamic parameters based on the wall shear stress. The wall shear stresses (WSS) and their time-average value $\overline{WSS}$ have been defined in section 2.1. In a healthy radial artery, $\overline{WSS}$ is in the range 1-2 Pa [8], which we will refer to as the healthy physiological WSS range. In a vein, it has been reported that neointimal hyperplasia rapidly develops when WSS values are below 0.5 Pa [164].

3 Results

3.1 Comparison of pre- and post-angioplasty geometries

The success rate of the treatment by balloon-angioplasty is mainly measured by the change in cross-section of the stenosis. Figure 4.3e shows the evolution of the cross-sectional area A within the plane of cut, as indicated in figure 4.1a. It is the plane perpendicular to the flow direction that passes through the stenosis throat. The degree of residual stenosis is obtained by comparing the value of A with the average cross-section of the parent vessel upstream of the treated stenosis. From the cross-sectional area, one can calculate the equivalent vessel diameter D_{eq}, which is the diameter of the disk with the same cross-section:

$$D_{eq} = \sqrt{\frac{4A}{\pi}}. \tag{4.6}$$

The various stenosis degrees correspond to an equivalent vessel diameter $D_{eq} = 2.65, 4.97, 5.31, 5.54$ and 5.94 mm, when the stenosis is reduced from 80% to 0%.

3.2 Comparison of pre- and post-angioplasty hemodynamic conditions

Results are first shown for an inlet mean pressure of $\overline{P}_a^i = 70$ mmHg. The influence of the boundary conditions will be examined in the next section.

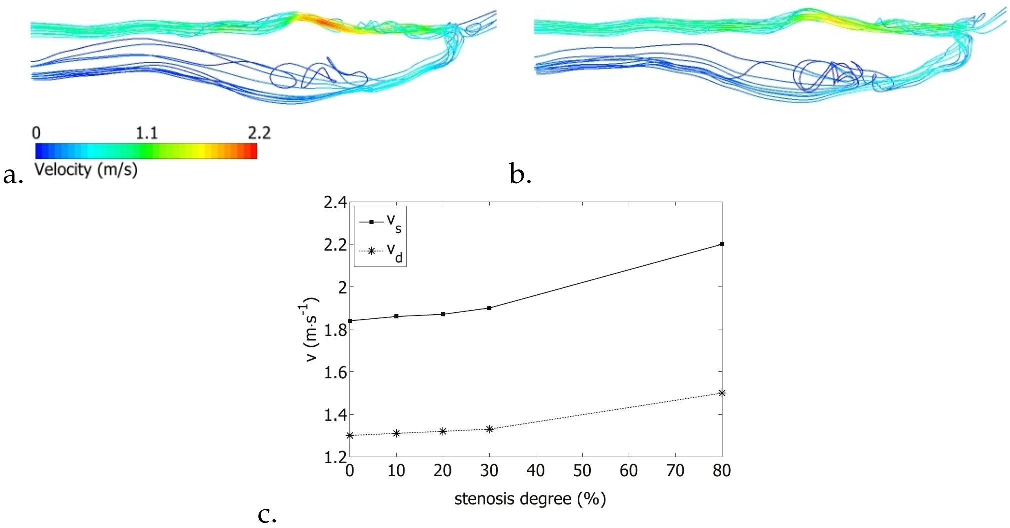

Figure 4.4: Streamlines at peak systole in the a) patient-specific and b) 0% residual stenosis geometries. c) Evolution of the peak systolic velocity v_s and late diastolic velocity v_d with the degree of residual stenosis.

3.2.1 Blood flow

The streamlines, shown in figures 4.4a,b at peak systole for the patient-specific native (80% stenosis) and fully treated (0% stenosis) geometries respectively, provide a qualitative picture of the flow field distribution within the AVF. The flow field away from the stenosis appears not to be significantly influenced by the angioplasty treatment. This is confirmed by comparing the time-averaged flow rate at the venous outlet in the two cases: it is reduced by only 4% when the arterial lumen cross-section is fully reopened. The main difference is observed locally at the stenosis, where the velocity magnitude is reduced following the removal of the stenosis. Figure 4.4c indicates the evolution of the peak systolic velocity v_s and late diastolic velocity v_d with the degree of residual stenosis. Both velocities follow a similar trend when the stenosis is treated and decrease up to 14 - 16%.

3.2.2 Wall shear stresses

Figures 4.5a,b show the spatial distribution of the time-averaged wall shear stress ($\overline{WSS}$) along the fistula wall for the patient-specific (80% stenosis) and fully treated (0% stenosis) geometries. The proximal and distal parts

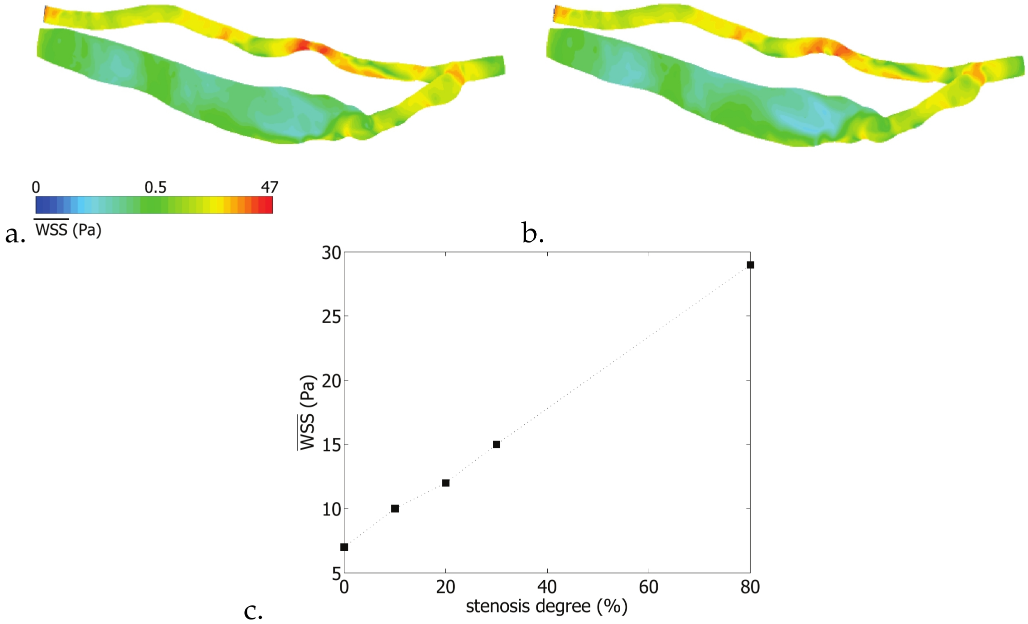

Figure 4.5: Spatial distribution of the time-averaged wall shear stress $\overline{WSS}$ for the a) patient-specific and b) 0% residual stenosis geometries. c) Evolution of the time-averaged wall shear stress $\overline{WSS}$ at the stenosis throat with the stenosis degree.

of the artery experience physiological values of $\overline{WSS}$ in the range 1-2 Pa [8]. The main exception is the stenosis, where the largest $\overline{WSS}$ values are observed. At this location, the maximum instantaneous value is 47 Pa (30 Pa if space-averaged across the stenosis neck). The anastomosis also experiences high WSS, but the maximum instantaneous value remains below 20 Pa. On the contrary, the vein experiences $\overline{WSS}$ values below 1 Pa or even 0.5 Pa in the dilated venous region.

In figure 4.5c we show the $\overline{WSS}$ values at the stenosis location when the stenosis degree is corrected by angioplasty. The treatment reduces the $\overline{WSS}$ values to nearly physiological values. However, the angioplasty treatment does not modify the $\overline{WSS}$ distribution within the AVF. This is coherent with the fact that it has a pure local effect at the level of the stenosis, as shown in section 3.2.1.

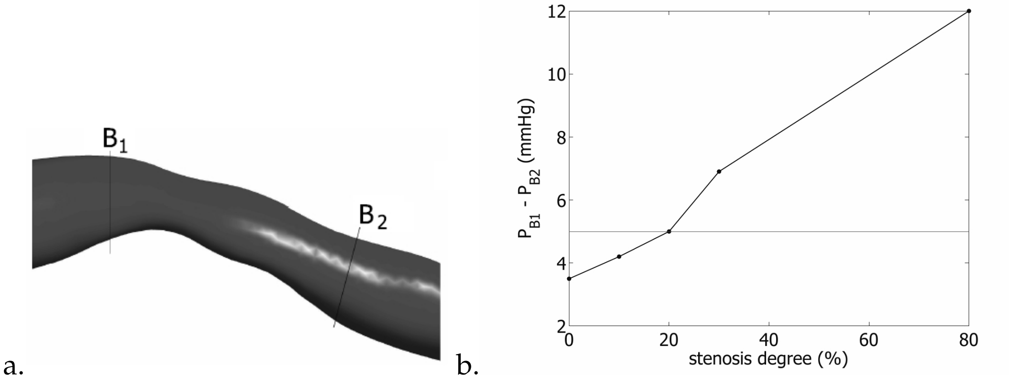

Figure 4.6: a) Location of planes B_1 and B_2. b) Stenosis pressure drop at the different degrees of residual stenosis. The horizontal line indicates the current clinical criterion, above which the lesion is treated by angioplasty.

3.2.3 Pressure drop across the stenosis

The pressure drop across the stenosis is evaluated as the difference in average pressure between plane B_1, located 1 mm upstream of the stenosis, and plane B_2, 1 mm downstream. The two planes are locally orthogonal to the main direction of the flow (figure 4.6a). Figure 4.6b shows the pressure drop $\overline{P}_{B_1}$ - $\overline{P}_{B_2}$ as a function of the degree of stenosis. The pressure drop across the stenosis increases almost linearly with the degree of stenosis. It is interesting to notice that a degree of stenosis below 20% needs to be reached to have a pressure drop below 5 mmHg.

3.3 Effect of the peripheral vascular boundary conditions on the hemodynamics inside the AVF

The effect of varying the mean arterial pressure is investigated by changing the values of the resistance and compliance at the arterial and venous boundary conditions (table 4.1). The values of resistance and compliance have been obtained maintaining the pulse pressure constant.

In table 4.2 we compare the most important quantitative parameters: the value of the time-averaged venous blood flow, which is an indicator of the flow split between the distal artery and the vein, the peak systolic velocity at the stenosis and the pressure drop across the stenosis. We observe

Table 4.2: Comparison of the time-averaged venous blood flow $\overline{Q}_v$ at S_v^o, peak systolic velocity v_s and stenosis pressure drop in the patient-specific geometry, when the peripheral R and C values are modified.

$\overline{\boldsymbol{P}}_a^i$ (mmHg)	**55**	**70**	**90**
$\overline{\boldsymbol{Q}}_v$ $(ml.min^{-1})$	750	752	754
v_s $(m.s^{-1})$	2.20	2.20	2.20
$\overline{\boldsymbol{P}}_{B_1}$ - $\overline{\boldsymbol{P}}_{B_2}$ (mmHg)	12.1	12	12

that none of the quantities are affected by the mean arterial pressure. The results therefore do not depend on the values set to the R and C constants in the Windkessel model.

4 Discussion and conclusions

We have analyzed the effects of an arterial stenosis affecting an arteriovenous fistula on the blood flow. We have simulated numerically the hemodynamics in a patient-specific AVF with an 80% stenosis along the afferent artery. The originality of the study is to model the removal of the stenosis by balloon-angioplasty through an implicit numerical simulation. The balloon is considered to be cylindrical when unloaded. The post-treatment geometry of the vessel is efficiently computed by mimicking the viscoplastic behavior of the arterial wall in the simulation. Since the stenosis removal is rarely complete in clinical practice, we have investigated different degrees of residual stenosis ranging from 30% to 0%. It is the range of stenosis correction that is considered as successful clinically.

To evaluate the influence of the arterial stenosis on the hemodynamics, we have compared the flow field within the patient-specific and treated geometries. Windkessel models are set as boundary conditions at the two outlets of the AVF to recreate physiological flow conditions. Different couples of R and C values have been imposed to investigate whether a different time-averaged inlet pressure might influence the hemodynamics within the fistula. The flow distribution across the branches of the fistula is not influenced by the mean arterial pressure, which is not surprising as the inlet pressure can be seen as the reference pressure.

We have shown that the arterial stenosis has no significant effect on the general hemodynamics within the AVF, leaving unchanged the blood flow split between the distal artery and the vein. This is coherent with a recent study that showed that arterial stenoses only affect the arterial outflow when they are located within 5 mm from the anastomosis [75]. Our result explains why the fistula of the patient under study was still functioning despite the presence of an 80% stenosis: having no effect on the venous flow rate, the stenosis did not impact the efficiency of the hemodialysis treatment.

The hemodynamic effect of the stenosis remains therefore purely local. A complete removal of the stenosis causes a 15%-decrease of the velocity amplitude at the throat, as indicated by the evolution of the systolic and diastolic velocities in figure 4.4c. If one calculates the corresponding pulsatility index (PI) according to equation (4.5), one can notice that it remains constant ($PI = 0.3$) regardless of the presence of the stenosis. It falls inside the physiological range [23] both before and after the balloon-angioplasty treatment. This index, introduced by clinicians to detect venous stenosis [26], therefore has no relevance in the case of arterial stenoses.

Quantifying the wall shear stresses WSS shows the drastic effect of the stenosis on the stenosis neck. At this location, the time-averaged stress $\overline{WSS}$ is 5 times larger than in the fully corrected case (0%-stenosis) - see figure 4.5c. Singh *et al.* [212] have shown that a time-averaged stress of 15 Pa is the threshold, above which the endothelial cells are irremediably damaged and atherosclerotic plaques might form. The present study indicates that the stenosis needs to be corrected with a degree of residual stenosis below 20% for the WSS to be below the threshold value of 15 Pa at the neck.

But the most direct effect that the arterial stenosis has on the hemodynamics is undoubtedly on the pressure drop. The pressure drop can be considered as its hemodynamic signature, i.e. the index that signifies its presence. This concept was already put forward by Young [213] for arterial stenoses in general. For the patients, an increase in pressure drop in the afferent artery leads to an increase in the cardiac work. The problem is that hemodialysis patients already have an increased cardiac work because of the very presence of the AVF (the fistula decreases the downstream vascular resistance). So it appears that the presence of an arterial stenosis further increases the risk of premature cardiac diseases and failure, which is already high in this patient population [41, 40]. In particular heart failure and sudden cardiac death are the critical events with the largest incidence and not myocardial infarction as for the rest of the population [42].

In clinics, a stenosis is currently treated when the pressure drop across the lesion is above 5 mmHg [59]. This criterion, originally set for venous stenoses, is used by default for arterial stenoses. We have found that a pressure drop of 5 mmHg corresponds to a 20% residual stenosis (figure 4.6b). Still stenosis degrees up to 30% are tolerated after angioplasty. The present study would therefore suggest that the criterion for stenosis treatment probably needs to be looked upon and adapted to the case of arterial stenosis, in order not to put patients at a higher risk of heart failure. It could also be worth including the peak $\overline{WSS}$ in the reflection. But more cases would need to be studied to check whether the present results hold on.

Another point that needs to be improved is the detection of arterial stenoses. We have seen that arterial stenoses cause an increase in pressure drop in the concerned artery, but such a quantity is difficult to measure clinically. It could be of interest to investigate whether the formation of an arterial stenosis is associated with an increase in systemic pressure. If so the monitoring of the blood pressure evolution could become indicative of the presence of a stenosis, if changes are looked for over long time periods.

Chapter 5

Simulation of the fluid-structure interactions after the endovascular treatment of a stenosed AVF

In this chapter study the effects of the endovascular treatment of a stenosed AVF by balloon-angioplasty with and without the positioning of a self-expandable stent. We transcribe the text as it has been submitted to the journal 'Journal of Biomechanical Engineering'.

1 Introduction

Hemodialysis is the therapy typically adopted for end-stage renal disease patients, while waiting for a kidney transplantation. It consists in supplying the kidney filtering function through a partial extracorporal circulation. Blood circulation to the hemodialyzer is achieved through a permanent vascular access. Various types of vascular access exist. One option is to create an arteriovenous fistula (AVF), which connects a vein onto an artery. AVFs have a low complication rate when compared to other options, such as grafts and central venous catheters [13, 14, 17, 15, 16]. But fistulas can be affected by different pathologies over time, one of them being the formation of stenoses.

Stenoses result in the reduction of the vascular lumen and lead to an increase in hydraulic resistance. They are typically caused by neo-intimal development or atherosclerotic plaque formation in regions of altered hemodynamics [11, 8, 56, 57]. Such flow conditions prevail, for instance, in the outflow vein of the fistula. But end-stage renal disease patients also present several comorbidities, such as hypertension and calcium-phosphate imbalance [214, 215]. These pathologies lead to a diffuse sedimentation of calcium ions at the vascular walls. The sedimentation generally develops in calcified atherosclerotic plaques. The combined effects of altered hemodynamics and vascular wall calcification explain why patients in hemodialysis may be affected by stenoses at multiple sites along the vascular tree.

Stenoses are typically treated, when they occlude more than 50% of the lumen [74] or when they induce a local pressure difference ΔP above 5 mmHg [59]. The most common treatment option is balloon-angioplasty. A balloon folded in a catheter is inserted endovascularly, guided across the vasculature up to the stenosis and inflated to restore the vessel lumen. Balloon-angioplasty has been proven to lengthen the period of fistula functionality [57, 60, 61, 59, 62, 63]. Ultra-high pressure balloons can be used for persistent stenoses [64].

Another endovascular treatment consists in deploying a stent across the lesion. Stenting usually follows the preliminary expansion of the stenosis by balloon-angioplasty. Two types of self-expandable stents are used to treat AVF stenoses: stents in Nitinol (e.g. SMART®, Cordis) or in stainless steel (e.g. Wallstent®, Boston Scientific) [65, 68]. The efficacy of stenting has been questioned since the late 80s [65] and it has only recently been proven to be more effective than balloon-angioplasty alone [62, 68].

Our present objective is to evaluate and compare the effects of both endovascular treatments on the hemodynamics and wall mechanics. We simulate the fluid-structure interactions (FSI) within the fistula before and after each treatment and compare them to the untreated case. For the stented vessel, we first simulate the opening of the vessel by balloon-angioplasty, where we position the stent inside the corrected geometry and deploy it. We then search for the mechanical behavior of the stented arterial section and determine its equivalent stiffness. We conduct the FSI simulation in the stented AVF geometry, modeling the presence of the stent by imposing the equivalent stiffness to the stented portion of the artery. The local influence of the presence of the stent struts is thus neglected. Details on the numerical methods are provided in section §2. The influence of the two treatments on the vessel shape, hemodynamics and internal stresses is described in section §3. The results and their clinical consequences are then discussed in section §4.

2 Material and methods

2.1 Geometry

We consider a patient-specific mature side-to-end radio-cephalic AVF presenting an 80% stenosis on the arterial side. The images have been obtained by computed tomography (CT) scan angiography at the Polyclinique St Côme (Compiègne, France) [170]. The data have been obtained in conformity with the ethical standard at the time of measurement. The geometry of the vascular lumen has been segmented and reconstructed. The vascular wall has then been extracted and divided into three zones, the healthy artery, the stenosed arterial portion and the vein, in order to impose different mechanical properties to each portion.

We model the angioplasty balloon as a cylindrical surface. The cylinder is created within ANSYS-Geometry (ANSYS, Inc.). Its length is 15 mm and its diameter 1 mm.

We simulate the stenting treatment with a stainless steel Wallstent® wirestent (Boston Scientific; Natik, MA, USA), which is one the most used to treat stenosed fistulas. It is a self-expandable braided stent. We model its geometry as a tubular shape made of sets of wires spiraling clockwise and anti-clockwise. The stent is created with the software PyFormex (copyright ©Benedict Verhegge). The stent has a length of 12 mm and a deployed diameter of 4.2 mm. It is composed of 24 separate wires.

2.2 Mesh

The lumen of the AVF is meshed in ANSYS T-Grid (ANSYS Inc.) by extrusion from the triangulation of the inflow lateral surface. The mesh is made of an hybrid grid of linear elements with prismatic elements in the boundary layer and tetrahedrons in the vessel core [201]. The vascular wall is meshed with a monolayer of shell elements starting from the nodes of the lateral surface of the AVF lumen. This condition ensures that the fluid and solid domains share the same nodes at the interface.

The balloon surface is meshed with linear triangular elements. The triangular elements are modeled as shell elements in ANSYS Workbench 13.0 (ANSYS, Inc.).

The stent is meshed in hexahedrons in Pyformex with the sweep method. The quality of the elements is, however, not sufficient for simulations in ANSYS. We therefore remesh the wires within ANSYS: we import each of the 24 wires within ANSYS-Structural, delete the existing mesh and mesh it with tetrahedrons with the default sweep patch-conforming algorithm.

2.3 Rheological and mechanical properties

Blood is assumed to be an isotropic, homogeneous, non-Newtonian fluid that follows Casson model. The apparent viscosity μ is given by

$$\sqrt{\mu} = \sqrt{\frac{\tau_0}{\dot{\gamma}}} + \sqrt{\kappa}, \tag{5.1}$$

where $\dot{\gamma}$ is the shear rate, τ_0 the yield stress and κ the consistency. The model parameters have been adjusted to fit experimental results at low shear rates: $\tau_0 = 4\times10^{-3}$ Pa, $\kappa = 3.2\times10^{-3}$ Pa·s [175]. Blood density is set to 1050 kg.m^{-3}.

Apart from the stenosed arterial region, we hypothesize that the vascular walls of the vein and artery are both made of a homogeneous, incompressible, hyperelastic material. They are assumed to follow the 3^{rd}-order Yeoh model [182] and the artery to be more compliant than the vein. Since no measurement of the wall mechanical properties has been conducted in an AVF, the law constants are chosen to best-fit experimental data obtained on a healthy artery and on a post-phlebitic vein (see [216] for more details). The stenosed part is modeled as viscoplatic with a Maxwell constitutive law. The law parameters are set to retrieve the same stiffness as the healthy arterial wall at small deformation and to fit the data of Maher *et al.* [185] at

Table 5.1: Values of the mechanical properties of the balloon and stent

	Balloon	**Stent**
ρ	1000 kg.m^{-3}	7999 kg.m^{-3}
E	9×10^{8} Pa	2×10^{9} Pa
ν	0.3	0.3

large deformation. This choice ensures continuity of the mechanical properties at the interface between the stenosed and non-stenosed segments.

The balloon and the stent are modeled with linear elastic material properties. The values of the density ρ, Young modulus E and Poisson coefficient ν are listed in Tab. 5.1.

2.4 Simulation of the endovascular treatment of the stenosis

2.4.1 Balloon-angioplasty

We simulate the opening of the balloon using ANSYS Structural (ANSYS Inc.). We first position the balloon unfolded across the arterial stenosis without any contact with the wall. It is inflated imposing a linearly increasing internal pressure with a maximum pressure of 5.1 bar. During opening, the balloon comes into contact with the artery. The contact is supposed to be frictionless [146] and solved using the augmented-Lagrange method.

At each instant of time, the structural simulation consists in finding the mechanical equilibrium between the deformable artery and the elastic balloon implicitly. When the maximum pressure is reached, the balloon is deflated with a linearly decreasing pressure. The degree of residual stenosis is equal to 20% after treatment.

2.4.2 Balloon-angioplasty followed with stent positioning

Stent deployment is modeled with ANSYS Structural (ANSYS Inc.) in a two-step implicit simulation. The balloon inflation is first simulated as described in section §2.4.1, while keeping the stent inactivated (i.e. transparent to the balloon and vessel). The stent is only activated at the end of this first step. During the second step, the balloon is deflated. The equilibrium shape of the artery is searched for, as the balloon recoils and the artery comes into contact with the elastic stent; it is function of the mechanical properties of the artery and stent. We define the contact between the artery and stent as frictional following the Coulomb theory. The friction coefficient is equal to 4.5×10^{-2}. Conversely, no contact is defined between the stent and the balloon.

2.5 Evaluation of the equivalent stiffness of the stented artery

We determine the equivalent stiffness of the stented artery following an inverse analysis approach using ANSYS-Structural. To do so, we set up two simulations of vessel inflation, both based on the geometry of the stented artery obtained following section §2.4.2. The difference is that the stent is only present in the first simulation (which is used as reference): the second simulation is conducted with a bare artery.

In the first simulation, we solve for the deformation of the stented artery imposing a linearly increasing pressure in the lumen in an implicit structural simulation. The contact between the artery and the stent is imposed to be bonded, which guarantees that the artery and stent deform together under the imposed pressure. We then simulate the inflation of the bare artery and search which mechanical properties need to be set to obtain the same deformation as for the stented artery.

2.6 Simulation of the fluid-structure interactions

We simulate implicitly the fluid-structure interactions in the geometries obtained after balloon-angioplasty with and without stenting. The numerical method has been described in details in [216]. Briefly, we couple implicitly the fluid and solid domains in ANSYS-Workbench (ANSYS, Inc.). The finite element structural solver uses a Lagrangian multiplier-based mixed u-P formulation. The simulation is performed assuming large displacements. The fluid solver is based on the Rhie-Chow interpolation method to calculate the fluid field solution implicitly [174]. We consider the atmospheric pressure as reference pressure and neglect gravity. The fluid-structure interactions are solved iteratively using the arbitrary Lagrangian-Eulerian formulation. Iterations are repeated within each time-step until all the field equations have converged and the coupling conditions are satisfied. Each FSI simulation is run over six consecutive cardiac cycles, with a time step equal to 5×10^{-3}s for both the fluid and the solid solver.

As boundary condition, we impose (*i*) 0-rotation and 0-translation at the vascular wall extremities; (*ii*) the time-dependent velocity profile measured on the patient at the inlet; (*iii*) the time-dependent pressure outlet profiles. The issue is that no patient pressure value is obtained *in vivo*, as pressure measurement is invasive. We therefore calculate the outlet pressures conducting a rigid-wall simulation in ANSYS CFX, applying Windkessel models at the two outlets. The constants of the Windkessel model are tuned following the method described in Decorato et al. [201]; they are obtained knowing from the measured value of the flow split between the arterial and venous outlets (30%-70% respectively) and prescribing an expected time-averaged inlet pressure.

3 Results

3.1 Post-treatment AVF geometry

A residual stenosis of 20% is achieved in both the stented and non-stented cases. Figure 5.1 shows the stenosed artery before treatment (a), after balloon-angioplasty (b) and after balloon-angioplasty plus stenting (c). The initial position of the balloon is indicated by the cylinder. Comparing Fig. 5.1 (b) and (c), one can observe that the geometry of the vessel is almost

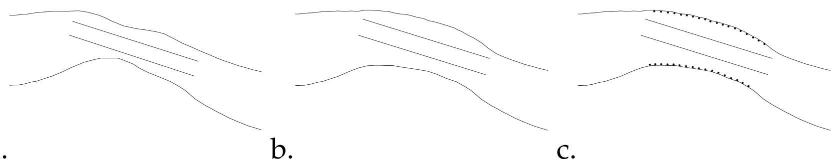

Figure 5.1: Geometry of the patient-specific afferent artery of the fistula (a) before treatment (b) after balloon-angioplasty and (c) after balloon-angioplasty with stenting. Both post-treatment cases present a residual stenosis equal to 20%.

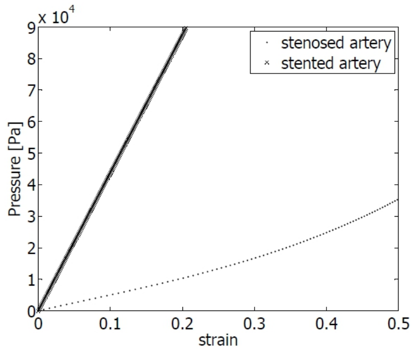

Figure 5.2: Pressure-strain relationship of the stented artery ('×' marks) as compared to the patient-specific non-treated case ('·' marks).

unchanged by the presence of the stent. No clear changes in the vessel curvature can be noticed.

3.2 Equivalent stiffness of the stented artery

Figure 5.2 compares the stress-strain curves for the stented and non-stented artery. It shows that the 'stented' region obeys to Hooke's law. The linear elastic mechanical behavior of the stent therefore prevails over the viscoplastic behavior of the vessel. The equivalent Young modulus E_{eq} of the stented artery is 437 MPa. The stented region results to be 8.7 times stiffer than the stenosed artery at small deformations. The Wallstent® therefore increases locally the vessel stiffness of the vessel after deployment. The equivalent stiffness of the stented artery E_{eq} is imposed to the stenosed region of the artery in the FSI simulation of the stented geometry.

3.3 Hemodynamics

Influence of balloon-angioplasty

In order to evaluate the influence of the stenosis treatment, we have detailed the values of a few key hemodynamic parameters provided by the FSI simulations (Tab. 5.2). Comparing the results before and after balloon-angioplasty, one can observe that the treatment has a significant effect in the stenosis region. It reduces the maximum velocity at the stenosis v_{max} by about 10%, which induces a 50% decrease in the wall shear stresses $\overline{WSS}_{stenosis}$.

Angioplasty also leads to a 60% decrease in the pressure difference across the stenosis ΔP (Tab. 5.2). For a residual degree of stenosis of 20%, the pressure difference is below 5 mmHg, indicated in the literature as the threshold value for treatment [59]. The treatment can thus be regarded as successful.

Table 5.2 shows that the venous flow rate Q_v remains unchanged. Indeed, we find that angioplasty hardly impacts the hemodynamics downstream of the stenosis (see also [201]).

Additional effect of stenting

The sole influence of stenting can be obtained by comparing the FSI results, when angioplasty is followed or not by stenting (Tab. 5.2). Hardly any difference can be noticed between the two treatments. They both lead to the same maximum velocity v_{max} and wall shear stresses $\overline{WSS}_{stenosis}$ at the stenosis. They engender the same flow distribution between the arterial and venous outlets, as shown by the similar values of venous flow rate Q_v. The pressure drop at the stenosis ΔP is neither affected by stent positioning: the treatment of the stenosis can be considered as successful in both cases, since ΔP remains each time below 5 mmHg.

3.4 Internal wall stresses

The local strain and internal wall stresses are evaluated after balloon-angioplasty with and without stent positioning and compared to the untreated case.

Table 5.2: Comparison of the most relevant hemodynamic parameters after balloon-angioplasty with and without stenting to the non-treated case.

	80%-stenosis	**angioplasty**	**angioplasty + stent**
v_{max} **(m.s^{-1})**	2.12	1.89	1.90
$\overline{WSS}_{stenosis}$ **(Pa)**	27	12	12.4
$\overline{Q}_v$ **(ml.min^{-1})**	779	772	772.2
ΔP **(mmHg)**	11.7	4.92	4.95

Table 5.3: Spatial-averaged values of the strain and normalized stresses at the stenosis at peak systole.

	80%-stenosis	**angioplasty**	**angioplasty + stent**
strain	15%	9%	3%
$\frac{\sigma_{max}}{\sigma_{art}}$	1.1	5	14

The internal stresses are evaluated using the maximum component of the Cauchy stress tensor σ_{max}. They are normalized by the mean stress in the healthy artery (σ_{art}). In Tab. 5.3, we compare the spatial-averaged strain and stresses provided by the three FSI simulations at peak systole in a region around the stenosis throat (10 mm in length). We observe that the maximum strain decreases by 40% after balloon-angioplasty and by 80% after balloon-angioplasty with stenting. Conversely, the normalized internal stress $\sigma_{max}/\sigma_{art}$ at the stenosis results to be 5 times larger after angioplasty alone and 14 times larger, when a stent is deployed.

In Fig. 5.3 we compare the time-averaged distribution of the normalized internal stress $\sigma_{max}/\sigma_{art}$ after the two treatments. After balloon-angioplasty, the stenosis region is subjected to an internal stress σ_{max}, which is up to 11 times larger than the baseline value σ_{art}. This residual stress is due to the

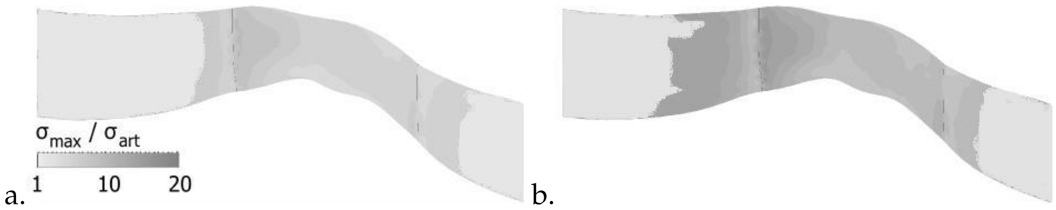

Figure 5.3: Time-averaged distribution of the maximum component of the Cauchy stress tensor σ_{max} normalized by the mean stress of the healthy artery at the stenosis post balloon-angioplasty (a) and post balloon-angioplasty with stent positioning (b).

permanent plastic deformations that occur within the vessel wall during balloon inflation. The positioning of a stent further increases the residual stress. The stress σ_{max} can be as large as 19 times the baseline value σ_{art} within the stented region. It is a consequence of the increase in vessel wall stiffness induced by the stent. Within the cephalic vein the stress distribution is the same before and after the treatment. It is about twice as large as σ_{art}.

Away from the stenosis, the stress σ_{max} decreases and regains the values observed in the healthy artery (σ_{art}). In the region upstream of the stenosis, the baseline stresses are completely recovered over a distance of 1.2 mm in the case of the simple balloon-angioplasty and of 2.5 mm in the case of stenting (Fig. 5.3). The mean gradient of the internal wall stresses is therefore only doubled following stenting: on average the stress gradient remains of the same order of magnitude as after balloon-angioplasty. The stent locally causes a larger stress gradient at the interface between the stented and non-stented portions of the artery: it is about 3.5 times larger after stent positioning. Downstream of the stenosis, the baseline stress values are recovered after a distance of 1.3 mm after both treatments. This implies that the mean spatial gradient of the internal wall stresses is 3 times larger after stent positioning than after the simple balloon-angioplasty.

4 Discussion

The results of this study show that positioning a self-expandable stent (e.g. Wallstent®) after balloon-angioplasty has a negligible effect on the vascular geometry. The shape and curvature of the vessel are hardly modified. The stent does not straighten the vessel, which indicates a small bending rigidity of the general structure. This is coherent with what has been found by Duerig and Wholey [217]. The wirestent device is designed to have a high radial stiffness to prevent the re-occlusion of the vessel and a large axial flexibility to follow the curvature of the vasculature after the deployment.

The inverse analysis provides a quantitative proof of what is guessed from the shape of the stented wall. The equivalent stiffness of the stented artery is only about 10 times larger than the bare artery (i.e. non-stented). This corroborates the *in vivo* results obtained by Vernhet *at al.* for Wallstent® stents implanted in the rabbit abdominal aorta [218]. The relatively small increase in the local vascular stiffness is due to the smaller rigidity of self-expandable stents as compared to balloon-expandable ones [217]. Self-expandable stents also have the advantage to subject the vascular wall to an expansion force sustained over time. They do not suffer from radial recoil, as it can be the case for balloon-expandable stents [217, 150]. Another advantage is the relatively small trauma caused to the endothelial cells by the stent deployment, in contrast to balloon-expandable stents [217].

The comparison of the results of the fluid-structure interaction simulations after balloon-angioplasty followed or not by stent positioning shows that, immediately after treatment, the two treatment options have equivalent effects on the hemodynamics both locally at the stenosis and globally in terms of distal flow split. These results are supported by recent clinical studies [62]. The hemodynamics is therefore hardly influenced by the local increase in stiffness of a portion of the vasculature.

The fact that the venous outflow $\overline{Q}_v$ keeps the value it had before treatment is particularly relevant for hemodialysis: the fistula remains functional despite the presence of an arterial stenosis. This is very different to the case of venous stenoses, which drastically reduce the venous outflow. Arterial stenoses, however, induce a large pressure drop in the afferent artery leading to an increase in the cardiac work. This issue is particularly critical for hemodialyzed patients, as they already have an increased cardiac work because of the very presence of the AVF [38]. The fistula indeed decreases the downstream vascular resistance, leading to an increase in cardiac output. So it appears that the presence of an arterial stenosis further increases the risk of premature cardiac disease and failure. It therefore seems crucial to treat arterial stenoses to reduce the pressure drop and thus the risk of heart failure [59, 12].

When considering the influence of the two treatments on the wall mechanics, we observe a larger difference than on the hemodynamics. The study has shown that residual stresses build up within the vascular wall following balloon-angioplasty: the internal wall stresses at the stenosis throat are, on average, five times the baseline value at peak systole (Tab. 5.3). Stenting causes an increase in the maximum internal wall stresses and in their spatial gradient, which is associated with the increase in vessel wall rigidity it brings. In the case of a Wallstent® stent, the increase is moderate (they are at maximum tripled). There should therefore be a limited risk of in-stent restenosis. Restenosis has been shown to mainly appear in the case of axially rigid balloon-expandable stents [104]: the latter can cause local alteration in wall shear stresses in the two regions upstream and downstream of the stent and endothelial damage, which are prone to neointima proliferation [104, 219]. But contrary to balloon-explandable stents, the self-expandable wirestent Wallstent® has a high axial flexibility.

In clinics it has been observed that balloon-angioplasty alone often fails because of the viscoelastic recoil of the vessel within 6-12 months after the treatment [62]. It has been proven recently that the additional use of stenting renders balloon-angioplasty more efficient, especially in the long term [62, 68]. From the present results, one can hypothesize that the stent enables to keep the vessel open. The beneficial impact of the stent is likely to be small immediately after treatment and to kick in in the months following the treatment, as the vessel recoils.

FSI simulations cannot model the viscoelastic recoil and predict the long-term response of the vascular wall. In the future it would be interesting to build a model of the evolution of the vessel, taking into account the endothelial response to hemodynamic solicitations as well as the wall response to altered internal stresses.

5 Conclusions

We have implicitly simulated the treatment of an AVF presenting an 80%-arterial stenosis by balloon-angioplasty with and without stent positioning. We have shown that implanting a self-expandable stent has the advantage of preserving the curvature of the treated vessel and causing a moderate increase in the local stiffness of the artery. Comparing the flow conditions predicted by the FSI simulations, we have found that the two treatments are equivalent. They preserve the functionality of the fistula, as none of them perturbs the flow distribution in the AVF; they both reduce the pressure difference across the stenosis below its critical value ($\Delta P \leq 5$ mmHg), which lowers the risk of heart complications in the long run. The comparison of the internal wall stresses after the two treatment options indicates that stent positioning leads to a maximum three-fold increase in the wall internal stress σ_{max} at the stenosis throat. This is moderate enough for in-stent restenosis to be unlikely to develop over time. The beneficial effect of stenting observed in clinics must come from the fact the the stent prevents the natural elastic recoil of the vessel after angioplasty and therefore the occurrence of restenosis.

Chapter 6

In vitro study of the hemodynamics in a patient-specific AVF

1 Introduction

Experimental Particle Image Velocimetry (PIV) is a valid tool for the study of the hemodynamics in complex vessels. It provides complementary results to numerical simulation techniques. A preliminary study has been conducted in a rigid-wall phantom that was the reproduction of the patient-specific AVF we considered for the numerical simulations. We have carried out the experiences in steady-state conditions. The CFD simulations have been computed to validate the experimental results.

2 Materials and methods

A flow inlet equal to 800 ml.min^{-1} is imposed at the arterial inlet S_a^i. At the boundary outlets of the numerical model we have imposed the same pressure values obtained in the experimental setup. The experiments are conducted assuming blood to be an isotropic, homogeneous, Newtonian fluid.

2.1 AVF geometry

A phantom made in poly(methyl methacrylate) (PMMA) is fabricated by rapid prototyping, as described in chapter 2, section 3.1. The CAD model of the geometry has been created by Innovaltech (IUT de l'Aisne, Saint-

Quentin, France) from the volume reconstruction of the AVF lumen is exported in STL file format. The vascular walls are generated with a thickness of 3 mm which is required for the rigidity of the mould. The phantom, when the fabrication ends, is rigid, and its transparency is sufficient to enable the measurement of the inner velocity field.

2.2 PIV: Principles and setup

Particle Image Velocimetry (PIV) is a technique that allows the estimation of the velocity field in a 3-dimensional flow by calculating the velocity vectors in a cut-plane. The typical PIV setup consists in a Charge Coupled Device (CCD) camera for image acquisition, a double pulsed laser for lighting the flow field seeded with particles and a PC for synchronization with the laser pulse and image recording. A software enables to control the laser and camera, determine the velocity field and post-process the data. The details of the principles for image capture and treatment have been described in chapter 2, section 3.2.

The experimental circuit has been installed in the Biomechanics and Bioengineering Laboratory (CNRS UMR 7338) at the Université de Technologie de Compiègne. We have used a steady-state pump (see chapter 2, section 3.3.1), the light source double laser Nano S PIV Pulsed Nd:Yag from the Litron Lasers (UK) provided in the pack LaVision Flowmaster PIV System (see chapter 2, section 3.3.3) and the Charged Coupled Device (CCD) camera Imager pro X 2M (LaVision) for image acquisition (see chapter 2, section 3.3.4). The protocol for image acquisition and post-treatment has been detailed in chapter 2, section 3.3.5. All the experiences have been conducted using an aqueous glycerine solution (see chapter 2, section 3.3.2). Its viscosity has been measured to be 3.75×10^{-3} Pa.s, and its density 1083.2 kg.m^{-3}. We seed the solution with lycopodium particles (Lycopodium, SIGMA-ALDRICH) with a concentration of 0.7 g.l^{-1}.

2.3 Results: comparison

We qualitatively compare the results obtained numerically and experimentally at three locations of interest in the AVF: the stenosis in the afferent radial artery, the anastomosis and the enlarged vein. Figures 6.1, 6.2 and 6.3 show the comparison between the experimental (a) and numerical (b) results in the three zones. A good qualitative agreement can be noticed. The same maximum velocity is measured with both techniques. A similar flow split between the distal artery and the cephalic vein is obtained by the experimental and numerical simulations.

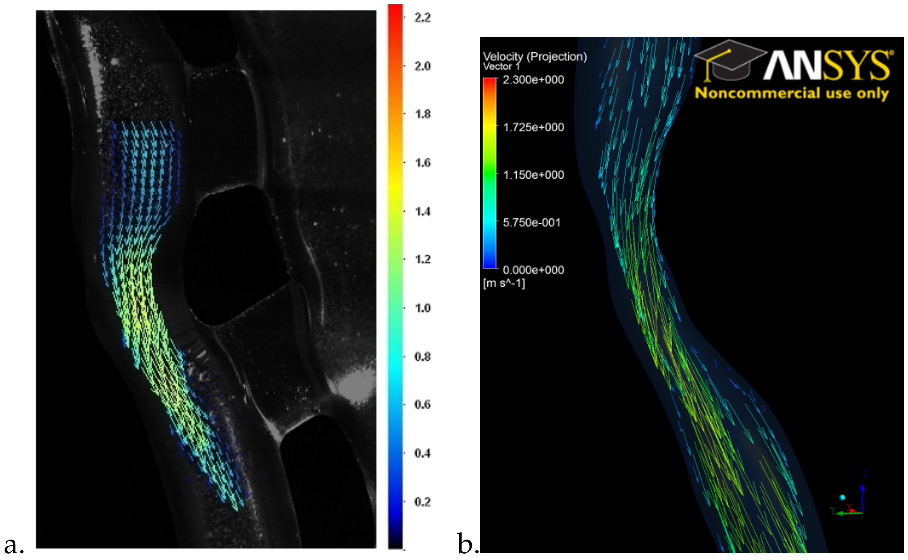

Figure 6.1: Qualitative comparison between the experimental (a) and the numerical velocity vectors field (b) at the stenosis in the proximal radial artery.

In order to quantitatively compare the results *in vitro* and *in silico*, we have extracted the velocity profile at defined cross-sectional diameters. Figures 6.4a, 6.5a and 6.6a show the cross-sectional planes A-A, B-B and C-C defined at the stenosis, at the anastomosis and in the enlarged vein respectively. In figures 6.4b, 6.5b and 6.6b we show the comparison between the numerical (CFX) and experimental (PIV) velocity profiles along the diameter in the chosen cross-sectional planes. We plot the velocity amplitude along the curvilinear abscissa x. The distance x has been normalized by the length of the diameter (D_{A-A} at the stenosis, D_{B-B} at the anastomo-

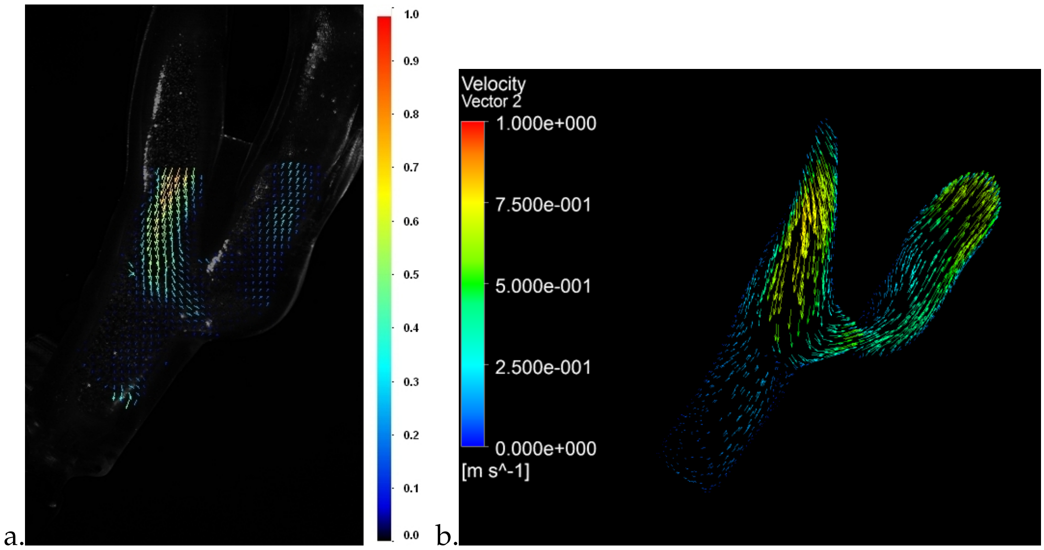

Figure 6.2: Qualitative comparison between the experimental (a) and the numerical velocity vectors field (b) at the anastomosis.

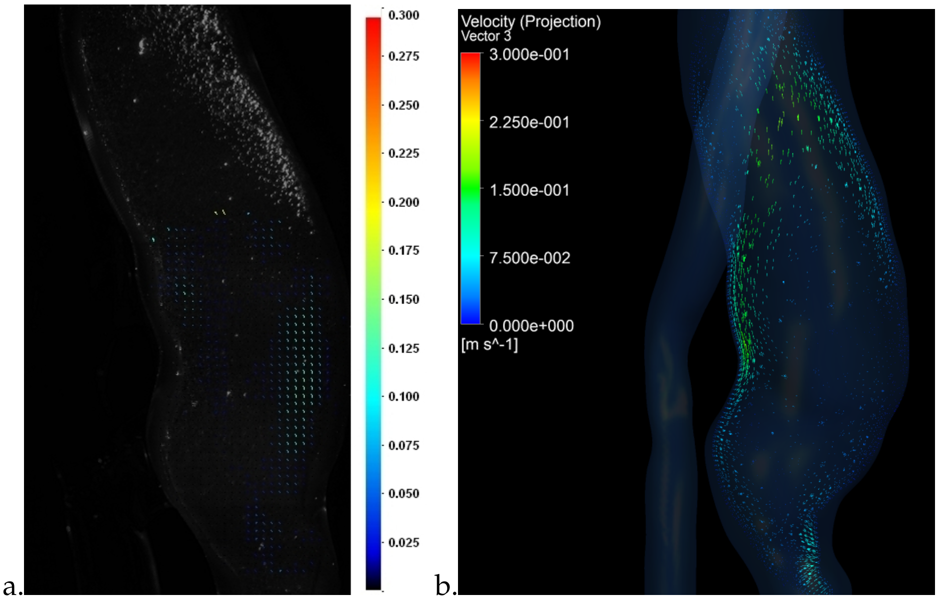

Figure 6.3: Qualitative comparison between the experimental (a) and the numerical velocity vectors field (b) at the enlarged vein.

sis and D_{C-C} at the enlarged vein). The curves representing the velocity profiles measured by PIV also show the standard deviation (black bars). One can notice a good agreement between the two profiles. The averaged relative difference has been found to be equal to 14% at the stenosis, 18% at the anastomosis and 22% at the enlarged vein. Figure 6.6 shows that the match between the two simulations is less perfect in the enlarged vein. The main reason is the extremely low amplitude of the velocities in the vein: such low velocity fields are always a challenge to measure experimentally. Another issue is the difficulty to identify the same exact cut plane in the numerical simulation as in the experiment. A small offset of the plane positioning can modify greatly the flow distribution, as the flow is highly perturbed in the vein enlarged region. PIV simulations, however, globally estimate velocity values which are lower than those calculated numerically. This evidence is coherent with what has been found by Ford *et al.* [84].

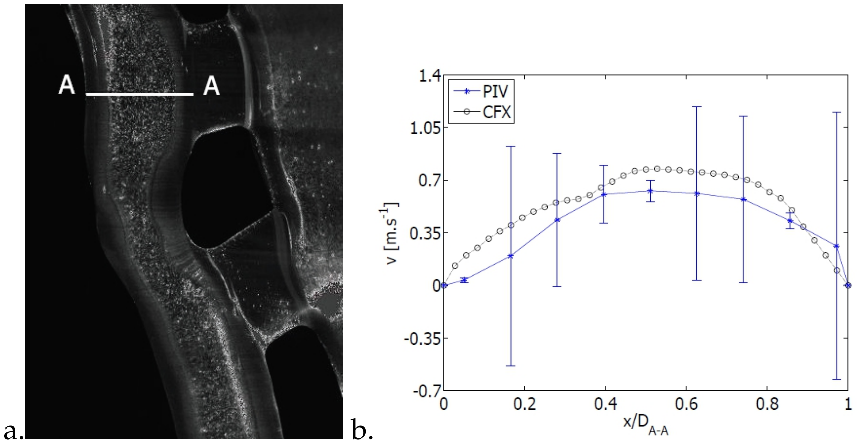

Figure 6.4: a) Cross-sectional diameter A-A defined at the stenosis. b) Comparison of the numerical (CFX) and experimental (PIV) velocity profiles extracted at the cross-sectional diameter A-A.

3 Discussion

The experimental and numerical results have shown a satisfactory agreement. With the PIV technique we correctly detect the major characteristics of the fluid dynamics within the fistula: the high velocity at the stenosis and flow recirculation at the anastomosis and inside the vein are correctly estimated. The objective is now to conduct the experiment under unsteady flow conditions. The analysis of the results has highlighted that it is difficult to extract the same plane from the experimental and numerical results to enable the quantitative comparison of the velocity magnitude. We

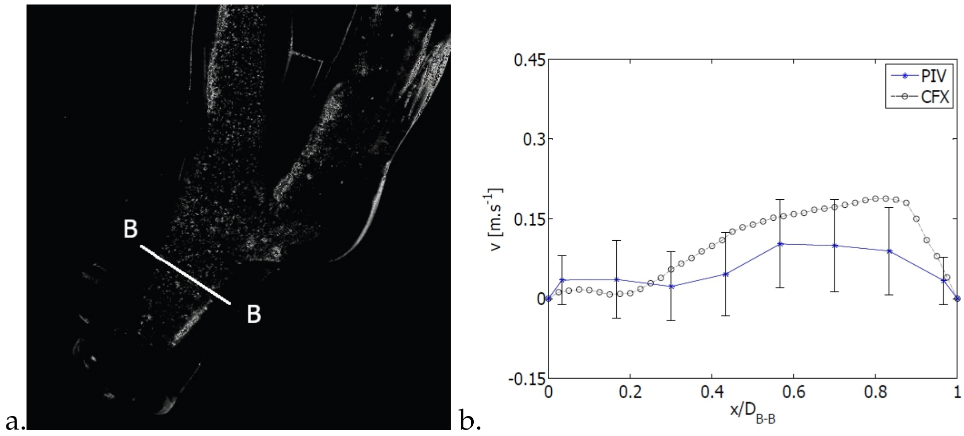

Figure 6.5: a) Cross-sectional diameter B-B defined at the anastomosis. b) Comparison of the numerical (CFX) and experimental (PIV) velocity profiles extracted at the cross-sectional diameter B-B.

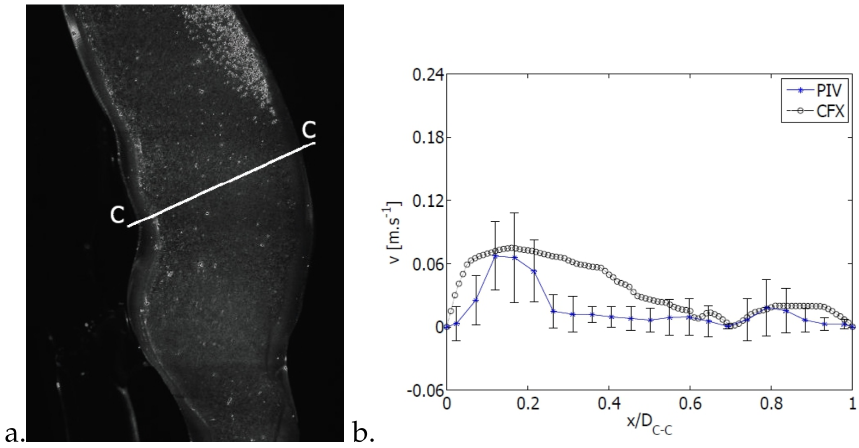

Figure 6.6: a. Cross-sectional diameter C-C defined at the vein. b) Comparison of the numerical (CFX) and experimental (PIV) velocity profiles extracted at the cross-sectional diameter C-C.

have in fact noticed that a small offset of the plane positioning can modify greatly the flow distribution, especially where the flow is highly perturbed (e.g. in the enlarged region within the vein). Despite the errors that are inevitably made in the plane determination, we find a more than satisfactory agreement between the PIV and CFD results.Comparing the velocity profiles at specific cross-sections we have also shown that PIV measurements globally underestimates the velocity values.This is coherent with previous results from literature [84].

In perspective, the same setup could be used for PIV measurements within a compliant phantom. In this case the first difficult is the fabrication of the phantom itself, especially if the mechanical properties of the different vessels need to be differenciated. Secondly, one needs to design a system for the positioning of the compliant phantom which prevents the fluttering of the phantom under the pulsating inner flow, as it would interfere with the measurements.

Chapter 7

Conclusions and perspectives

1 Main outcomes of the study

Clinical procedures for the treatment of AVF complications are today mainly based on empiric knowledge, since it is still difficult to obtain quantitative hemodynamic data from *in vivo* imaging exams. During the last 20 years, several *in vitro* and *in silico* models have been developed to investigate and better understand the hemodynamics within the AVF. None of these studies has however considered, to our knowledge, the vascular wall compliance.

During the first part of the study we have investigated the hemodynamics and wall mechanics in a mature AVF. We have modeled numerically the fluid-structure interactions in a patient-specific AVF geometry. The velocity profile measured on the patient is imposed at the arterial inlet. At the boundary outlets, we impose the time-variable pressure profiles obtained from a computational fluid-dynamic simulation in which the second-order Windkessel model has been implemented. It allows to take into account the resistances and compliances of the vessels downstream of the fistula. Blood is considered to behave as a non-Newtonian fluid because of the low shear rates observed within the vein. The results of FSI simulations show that the fistula is subjected to several regions of flow recirculation, especially within the enlarged vein. It directly affects the wall shear stresses, which are very low in the vein. In parallel, the oscillatory shear index increases. The venous wall also experiences large internal wall stresses, which are about twice the baseline value. Both the hemodynamic and wall stresses might therefore favour the remodeling of the venous wall.

The large computational cost of the fluid structure interaction simulation makes the transfer to clinicians difficult. It currently limits the use of numerical simulation as a diagnostic tool. We have therefore investigated whether the fully-coupled FSI could be simplified maintaining a sufficient accuracy in the evaluation of both the hemodynamics and wall mechanics. We have shown that fluid uncoupled simulation provides the time-evolution of the hemodynamic parameters in the AVF with 10-15% accuracy. The structural uncoupled simulation can provide the wall internal stresses with a greater accuracy, but only at one instant of time within the cardiac cycle. The FSI simulations have the advantage to provide the complete picture of the stresses acting in and on the vascular wall and to guarantee the equilibrium at the interface between the simulated blood flow and vascular wall at each time step, but they require longer computational times.

The considered patient-specific geometry presents an arterial stenosis. In literature, little is known about this kind of lesion, and its incidence on hemodialysis efficiency has only recently been assessed [72, 75]. However, the effects of the arterial stenoses on the hemodynamics in arteriovenous fistulas have not yet been investigated. In the second part of the study we have therefore focused our attention on the influence of the stenosis, and analyzed the hemodynamics in the stenosed fistula. We have then simulated numerically the endovascular treatment by balloon-angioplasty. Clinically, balloon-angioplasty rarely corrects the stenosis fully and a degree of stenosis remains after treatment. Residual degrees of stenosis below 30% are considered as successful. We have inflated the balloon with different pressures to simulate residual stenoses ranging from 0 to 30%. The results show that the arterial stenosis has little impact on the blood flow distribution: the venous flow rate remains unchanged and thus permits hemodialysis. The stenosis at the afferent artery, therefore, does not compromise the efficacy of the hemodialysis. This shows that arterial stenoses behave very differently to venous stenosis. Venous stenoses are known to significantly reduce the venous outflow. Clinicians therefore monitor and compare hemodynamic parameters that are related to the venous flow during the hemodialysis. Venous stenoses are suspected when a reduction in the venous flow is observed. Arterial stenoses must have remained unnoticed until recently, because they do not have the same complication on the hemodialysis treatment. Contrary to venous stenosis, arterial stenoses cause an increase in the local pressure difference, which can lead to an increase in cardiac work. We have quantified the local increase in pressure due to the stenosis, and calculated the pressure drop after treatment by balloon-angioplasty. We have questioned the criteria used in clinical practice for the evaluation of a successful balloon-angioplasty. We have shown that for the investigated case a 30% residual stenosis leads to a large local pressure drop, even if this degree of residual stenosis is considered successful in clinical practice. The current clinical criteria is therefore not universally valid. To guarantee a pressure drop below 5 mmHg, which is considered as the threshold stenosis pressure difference clinically [59], the residual stenosis degree must be 20% maximum.

Balloon-angioplasty is not the only endovascular treatment which can be adopted by clinicians. The use of stents has been introduced since late 80s [65], but for about 30 years the use of stent has been largely questioned. We have simulated numerically the balloon-angioplasty followed by the positioning of the self-expandable stent Wallstent® (Boston Scientific; Natik, MA, USA). Our results show that balloon-angioplasty with or without stent positioning have the same impact on the hemodynamics. The stent has only a local effect on the internal wall stresses at the stenosis, which are about 3.5 the stresses at the stenosed artery post balloon-angioplasty. Additionally, self-expandable stents hardly straighten the vascular geometry.

Stents are used when angioplasty does not succeed but or to prevent the viscoelastic recoil of the artery, occurring sometimes 6-12 months after the simple angioplasty [62]. But the large internal stresses observed after stent positioning might induce in-stent restenosis and cause the failure of the treatment. In the literature it has been shown that axially-flexible stents have a negligible effect for inducing neointima proliferation leading to in-stent restenosis [104]. If the restenosis is avoided, it is reasonable to conclude that the stent positioning might be more effective than the simple angioplasty in the long term. This conclusion is supported by recent clinical observations [62, 68].

The study we have carried out presents several aspects of novelty:

- The difference in mechanical properties of the vein and the artery have been taken into account;
- The imposed boundary conditions are directly measured (velocity inlet) or derived from pressure and flow information measured on the patient (Windkessel model);
- The impact of an arterial stenosis has been quantified;
- The endovascular treatments by balloon-angioplasty without/with stenting have been simulated implicitly;
- The impact of the two possible endovascular treatments are investigated, quantified and compared.

In the last part of the study we have also set up an the experimental bench for the evaluation of the hemodynamics within the AVF using PIV. The comparison between experimental and numerical results has shown a good agreement. The experimental setup is ready for further investigations, typically in unsteady flow conditions.

2 Perspectives

The numerical tool developed for the study of the fluid-structure interactions and the effect of the endovascular treatment of a stenosis offers many perspectives. In the next future, the simulations could be easily adapted to the new version of ANSYS-Workbench: ANSYS 14.5. This version is available since November 2012, and contains improvements in the coupling algorithm used to solve the fully-coupled FSI simulations. The use of parallel calculation has also been made more robust and effective. The increased computational robustness should significantly reduce the computational time. Moreover, improved meshing capabilities and robust automation tools are likely to reduce the time that the user spends preparing the model.

It would be interesting to apply the numerical FSI simulation we have developed to the study of the hemodynamics and wall mechanics within fistula geometries of **different patients**. This study might enable the identification and quantification of hemodynamic and wall mechanic parameters, both local and global, that are altered when compared to the physiological baseline. The clinical criteria for the evaluation of the functionality of the fistula might thus be improved.

Similarly, it would be interesting to compare the results of the simulations with the clinical **follow-up of patients**. Such an investigation should enable the refinement of the criteria today used to identify regions which are prone to neointima formation and wall remodeling. Moreover, it might enable researchers to understand how eventual systemic pathology of the patient might alter the vascular wall response to hemodynamic and mechanical solicitations.

Another possible perspective for the numerical simulations we developed is the simulation of the **treatment of other pathologies**. Similarly to what we have done for arterial stenoses, one might simulate numerically the treatment of other pathologies that affect fistulas. For instance, the reduction of the venous diameter in case of hyperflow could be simulated. The investigation of the effects on the hemodynamics of different final venous diameter might enable researchers to quantify the optimal diameter based on quantitative hemodynamic parameters. Similarly to what we did for the residual stenosis post balloon-angioplasty, the reduction of the venous diameter for the treatment of the hyperflow can be simulated. The venous diameter to be obtained after the treatment could therefore be optimized.

In our simulations we have used literature data for the mechanical properties of the healthy and stenosed artery as well as for the vein. Recently, high-resolution ultrasound techniques have been proven to be effective in the evaluation of the mechanical properties of the vessels of fistulas for hemodialysis *in vivo* [22]. The model of fluid-structure interaction simulation that we have developed should be adapted to the patient-specific case also in terms of wall mechanics.

Thanks to the more efficient and robust calculation algorithms, the remodeling of the vasculature under the hemodynamic and internal stresses conditions may be taken into account in a **multi-scale model** coupled to the FSI simulation. However, if multi-scale models which describe wall adaptations when subjected to non-physiological hemodynamic parameters are quite clear, less is known about the response to altered wall internal stresses. This type of model might help clinicians predict the evolution and adaptation of the vascular wall in response to the hemodynamic and mechanic stimuli.

Finally, the developed models might potentially be **introduced in clinical routine** as tools to help surgeons in the decision-making process. This step might require the automatic segmentation and volume reconstruction from patient-specific geometries. The setup of the patient-specific numerical simulation should also be automated, and the flow at the afferent artery as well as the time-varying pressure conditions at the arterial and venous outlets automatically set as boundary conditions. A clinical study that proves the efficacy of the use of numerical simulations as a predictive tool should be carried out. Once the efficacy is proven, numerical predictive tools could be used in clinical routine.

Appendix A

Pyformex

In order to reproduce the geometry of a typical wire stent which is used in case of stenoses in AVFs (Wallstent, Boston Scientific), we use the open-source code PyFormex (`http://www.nongnu.org/pyformex/`) [220]. The code can be divided in two main parts:

- The generation of the 3-dimensional geometry;
- The generation of the mesh;
- The export of the meshed geometry.

1 3-D geometry generation

The first part of the code consists in the definition of the variables that can be given as input by the user and the creation of the geometry. It is part of PyFormex software (copyright ©Benedict Verhegge). The code is commented in order to clarify what is done by each sequence of command lines.

```
#!/usr/bin/env pyformex --gui


# needed if we import this from another script
from formex import *
from plugins import curve
from plugins.trisurface import TriSurface
from plugins.fe_abq import *
import simple
```

```
class DoubleHelixStent:
    """Constructs a double helix wire stent.

    A stent is a tubular shape such as used for opening obstructed
    blood vessels. This stent is made from sets of wires spiraling
    in two directions.
    The geometry is defined by the following parameters:
      L  : approximate length of the stent
      De : external diameter of the stent
      D  : average stent diameter
      d  : wire diameter
      be : pitch angle (degrees)
      p  : pitch
      nx : number of wires in one spiral set
      ny : number of modules in axial direction
      ds : extra distance between the wires (default is 0.0 for
           touching wires)
      dz : maximal distance of wire center to average cylinder
      nb : number of elements in a strut (a part of a wire between two
           crossings), default 4
    The stent is created around the z-axis.
    By default, there will be connectors between the wires at each
    crossing. They can be switched off in the constructor.
    The returned formex has one set of wires with property 1, the
    other with property 3. The connectors have property 2. The wire
    set with property 1 is winding positively around the z-axis.
    """
    def __init__(self,De,L,d,nx,be,ds=0.0,nb=4,connectors=True):
        """Create the Wire Stent."""
        D = De - 2*d - ds
        r = 0.5*D
        dz = 0.5*(ds+d)
        p = math.pi*D*tand(be)
        nx = int(nx)
        ny = int(round(nx*L/p))  # The actual length may differ a bit from L
        # a single bumped strut, oriented along the x-axis
        bump_z=lambda x: 1.-(x/nb)**2
        base = Formex(pattern(’1’)).replic(nb,1.0).bump1(2,[0.,0.,dz],bump_z,0)
```

```
        # scale back to size 1.
        base = base.scale([1./nb,1./nb,1.])
        # NE and SE directed struts
        NE = base.shear(1,0,1.)
        SE = base.reflect(2).shear(1,0,-1.)
        NE.setProp(1)
        SE.setProp(3)
        # a unit cell of crossing struts
        cell1 = (NE+SE).rosette(2,180)
        # add a connector between first points of NE and SE
        if connectors:
            cell1 += Formex([[NE[0][0],SE[0][0]]],2)
        # create its mirror
        cell2 = cell1.reflect(2).translate([2.,2.,0.])
        base = cell1 + cell2
        # reposition to base to origin [0,0]
        base = base.translate(-base.bbox()[0])
        # Create the full pattern by replication
        dx,dy = base.bbox()[1][:2]
        F = base.replic2(nx,ny,dx,dy)
        # fold it into a cylinder
        self.F = F.translate([0.,0.,r]).cylindrical(dir=[2,0,1],scale=[1.,360./(nx*dx),p/nx/dy])
        self.ny = ny

    def getFormex(self):
        """Return the Formex with all bar elements.

        This includes the elements along all the wires, as well as the
        connectors between the wires.
        """
        return self.F

    def getWireAxes(self):
        """Return the wire axes as curves.

        The return value is two lists of curves (PolyLines), representing the
        individual wire axes for each wire direction.
        """
```

2 Generation of the mesh of the multi-wires stent

In the second part of the script, which we developed during the PhD, consists in the mesh creation through a sweep method on each wire and its export as an ABAQUS input file. The code is reported below. Comment lines are provided.

```
        import connectivity
        M = self.F.toMesh()
        ML = [ M.withProp(i) for i in [1,3] ]
        wires = [ connectivity.connectedLineElems(Mi.elems) for Mi in ML
            ]
        wireaxes = [ [ Formex(M.coords[wi]).toCurve() for wi in wiresi ]
            for wiresi in wires ]
        return wireaxes


if __name__ == "draw":

    # show an example

    wireframe()
    reset()

    res = askItems([
        ('L',80.,'',{'text':'Length of the stent'}),
        ('D',10.,'',{'text':'Diameter of the stent'}),
        ('n',2 ,'',{'text':'Total number of wires'}),
        ('b',30.,'',{'text':'Pitch angle of the wires'}),
        ('d',0.2,'',{'text':'Diameter of the wires'}),
        ])

    if not res:
        exit()

    globals().update(res)
    if (n % 2) != 0:
        warning('Number of wires must be even!')
        exit()

    H = DoubleHelixStent(D,L,d,n,b)
```

```
clear()
view('iso')
for w,c in zip(H.getWireAxes(),['black','magenta']):
  print 'w is :', w[1]
  print 'c is :', c
     #draw(w,color=c)

HH=H.getWireAxes()
clear()
draw(HH[1],color='red')    #HH[0] contains left-handed wires, HH[1]
    the right-handed


F = simple.sector(0.11,360.,8,8,h=0.0,diag='up')        #defines a
    circular face
CS = TriSurface(F)                           #meshes the face with
    triangles
```

3 Export for ANSYS environment

The last part of the script has been developed in order to export the meshed wires in a format readable within ANSYS Workbench. As explained in section 2.4.2 we however had to re-mesh the wires with a native mesh for ANSYS Structural simulations. Here below we report, commented, the part of the script developed for the export.

```
for i,x in zip(HH[0], range(n)):                  #iterates the
    components of HH (which are n) and the integer x from 0 to n-1
    increasing them conjointly
        pathi = i                        #the current wire is defined as
             path
        structure1i = CS.sweep(pathi,normal=[0.,0.,1.],upvector
            =[1.,0.,0.])  #sweeps the circular meshed face CS along
            the current path
        elem1i = structure1i.eltype = 'C3D8'   #defines the element
            type
        export({'wireR':structure1i})
        ai = exportMesh(str(x)+'wireR.inp',structure1i)  #write the
            abaqus input file changing its name at each iteration
```

```

            '''the procedure is repeated for the left-handed wires'''
    for z,y in zip(HH[1], range(n)):
            pathz = z
            structure2z = CS.sweep(pathz,normal=[0.,0.,1.],upvector
                =[1.,0.,0.])
            elem12z = structure2z.eltype = 'C3D8'
            export({'wireL':structure2z})
            bz = exportMesh(str(y)+'wireL.inp',structure2z)

#End
```

Bibliography

[1] I vanTricht. *Hemodynamics of vascular access for hemodialysis*. PhD thesis, Gent University, 2005.

[2] WH Horl, KM Koch, C Ronco, and JF Winchester. *Replacement of Renal Function by Dialysis*. Kluwer Academic Publishers, 2004.

[3] Gail D. Baura. Chapter 9 - hemodialysis delivery systems. In *Medical Device Technologies*, pages 193 – 216. Academic Press, Oxford, 2012.

[4] H Wasse, N Kutner, R Zhang, and Y Huang. Association of initial hemodialysis vascular access with patient-reported health status and quality of life. *Clin J Am Soc Nephrol 708-714, 2007*, 2:708–714, 2007.

[5] G Brunori, A Bandera, F Valente, and A Laudon. Vascular access for dialysis in elderly: AVF versus permanent CVC. *G Ital Nefrol*, 25:614–618, 2008.

[6] SJ Schwab, GL Buller, RI McCann, RR Bollinger, and DL Stickel. Prospective evaluation of a dacron cuffed hemodialysis catheter for prolonged use. *Am J Kidney Dis*, 11:166–169, 1988.

[7] TN McAllister, M Maruszewski, SA Garrido, W Wystrychowski, N Dusserre, A Marini, K Zagalski, A Fiorillo, H Avila, X Manglano, J Antonelli, A Kocher, M Zembala, L Cierpka, LM de la Fuente, and N L'Heureux. Effectiveness of haemodialysis access with an autol-

ogous tissue-engineered vascular graft: a multicentre cohort study. *Lancet*, 373:1440–1446, 2009.

[8] I vanTricht, D DeWachter, J Tordoir, and P Verdonk. Hemodynamics and complications encountered with arteriovenous fistulas and grafts as vascular access for hemodialysis: a review. *Ann Biomed Eng*, 33:1142–1157, 2005.

[9] DW Windus. Permanent vascular access: a nephrologist's view. *Am J Kidney Dis*, 21:457–471, 1993.

[10] JP VanWaeleghem, MM Elseviers, and EJ Lindley. Management of vascular access in europe. part i: A study of centre based policies. *J Ren Care*, 26:28–33, 2000.

[11] K Konner, B Nonnast-Daniel, and E Ritz. The arteriovenous fistula. *J Am Soc Nephrol*, 14:1669–1680, 2003.

[12] SJ Schwab, M Saeed, SK Sussman, RL McCann, and DLStickel. Transluminal angioplasty of venous stenoses in polytetrafluoroethylene vascular access grafts. *Kidney Int*, 32:395–398, 1987.

[13] TS Huber, JW Carter, RL Carter, and JM Seeger. Patency of autogenous and polytetrafluoroethylene upper extremity arteriovenous hemodialysis accesses: a systematic review. *J Vasc Surg*, 38:1005–1011, 2003.

[14] K Konner. History of vascular access for haemodialysis. *Nephrol Dial Transplant*, 20:2629–2635, 2005.

[15] M Malovrh. How to increase the use of native arteriovenous fistulae for haemodialysis. *Prilozi*, 32:53–65, 2011.

[16] M Torreggiani, ML Scaramuzzi, A Manini, F Castoldi, N Serpieri, N Maggi, G Sileno, C Migotto, V Esposito, F Montagna, and C Esposito. Hemodialysis vascular access: everything you always wanted to know about it (but were afraid to ask). *J Nephrol*, 19:Epub ahead of print, 2012.

[17] J Tordoir, B Canaud, P Haage, K Konner, A Basci, D Fouque, J Kooman, A Martin-Malo, L Pedrini, F Pizzarelli, J Tattersall, M Vennegoor, C Wanner, P ter Wee, and R Vanholder. EBPG on vascular access. *Nephrol Dial Transplant*, Suppl 2:ii88–ii117, 2007.

[18] MJ Brescia, JE Cimino, K Appel, and BJ Hurwich. Chronic hemodialysis using venipuncture and a surgically created arteriovenous fistula. *N Engl J Med*, 275:1089–1092, 1966.

[19] B Ene-Iordache and A Remuzzi. Disturbed flow in radial-cephalic arteriovenous fistulae for haemodialysis: low and oscillating shear stress locates the sites of stenosis. *Nephrol Dial Transplant*, 27:358–368, 2012.

[20] Z Kharboutly. *Etude de l'ï£¡coulement sanguin dans des fistules arterio-veineuses reconstruites ï£¡ partir d'images mï£¡dicales*. PhD thesis, Universitï£¡ de Technologie de Compiï£¡gne, 2007.

[21] LEM Duijm, EH Overbosch, YS Liem, RN Planken, JHM Tordoir, PWM Cuypers, P Douwes-Draaijer, and MW de Haan. Retrograde catheterization of haemodialysis fistulae and grafts: angiographic depiction of the entire vascular access tree and stenosis treatment. *Nephrol Dial Transplant*, 24:539–547, 2009.

[22] R Biswas, P Patel, DW Park, TJ Cichonski, MS Richards, JM Rubin, J Hamilton, and WF Weitzel. Venous elastography: validation of a novel high-resolution ultrasound method for measuring vein compliance using finite element analysis. *Semin Dial*, 233:105–109, 2010.

[23] S Sivanesan, TV How, RA Black, and A Bakran. Flow patterns in the radiocephalic arteriovenous fistula: an in vitro study. *J Biomech*, 32:915–925, 1999.

[24] C Moquet, MO Bitker, O Bailliart, J Rottembourg, F Clergue, LS Montejo, JP Martineaud, and P Viars. Anesthesia for creation of a forearm fistula in patients with endstage renal failure. *Anesthesiology*, 70:909–914, 1989.

[25] S Sivanesan, TV How, and A Bakran. Characterizing flow distributions in AV fistulae for hemodialysis access. *Nephrol Dial Transplant*, 13:3108–3110, 1998.

[26] R Albayrak, S Yuksel, M Colbay, B Degirmenci, G Acarturk, and A Haktanirand O Karaman. Hemodynamic changes in the cephalic vein of patients with hemodialysis arteriovenous fistula. *J Clin Ultrasound*, 135:133–137, 2007.

[27] BS Dixon. Why don't fistulas mature? *Kidney Int*, 70:1413–1422, 2006.

[28] JM Corpataux, E Haesler, P Silacci, HB Ris, and D Hayoz. Low-pressure environment and remodelling of the forearm vein in Brescia-Cimino haemodialysis access. *Nephrol Dial Transplant*, 17:1057–1062, 2002.

[29] MA Yerdel, M Kesence, KM Yazicuoglu ans Z Doseyen, AG Turkcapar, and E Anadol. Effect of hemodynamic variables on surgically created arteriovenous fistula flow. *Nephrol Dial Transplant*, 12:1684–1688, 1997.

[30] M Kosch, A Levers, M Barenbrock, F Matzkies, RM Schaefer, K Kisters, KH Rahn, and M Hausberg. Acute effects of haemodialysis on endothelial function and large artery elasticity. *Nephrol Dial Transplant*, 16:1663–1668, 2001.

[31] SB Leapman, M Boyle, MD Pescovitz, ML Milgrom, RM Jindal, and RS Filo. The arteriovenous fistula for hemodialysis access: gold standard or archaic relic? *Am Surg*, 62:652–656, 1996.

[32] E Wijnen, N Planken, X Keuter, JP Kooman, JHM Tordoir MW de-Haan, KML Leunissen, and F van der Sande. Impact of a quality improvement programme based on vascular access flow monitoring on costs, access occlusion and access failure. *Nephrol Dial Transplant*, 21:3514–3519, 2006.

[33] R Bellazzi, L Sacchi, E Caffi, A de Vincenzi, M Nai, F Manicone, C Larizza, and R Bellazzi. Implementation of an automated system for monitoring adherence to hemodialysis treatment: A report of seven years of experience. *Int J Med Inform*, 81:320–331, 2012.

[34] F Gotch. The basic, quantifiable parameter of dialysis prescription is Kt/V urea; treatment time is determined by the ultrafiltration requirement; all three parameters are of equal importance. *Blood Purif*, 25:18–26, 2007.

[35] B Charra, M Calemard, and G Laurent. Importance of treatment time and blood pressure control in achieving long-term survival on dialysis. *Am J Nephrol*, 16:35–44, 1996.

[36] MR Marshall, BG Byrne, PG Kerr, and SP McDonald. Associations of hemodialysis dose and session length with mortality risk in Australian and New Zealand patients. *Kidney Int*, 69:1229–1236, 2006.

[37] O Ifudu. The concept of 'dry weight' in maintenance hemodialysis: flaws in clinical application. *Int J Artif Organs*, 19:384–386, 1996.

[38] AD Menno, J Zizzi, J Hodson, and J McMahon. An evaluation of the radial arterio-venous fistula as a substitute for the quinton shunt in chronic hemodialysis. *Trans Am Soc Artif Intern Organs*, 13:62–67, 1967.

[39] S Isoda, H Kajiwara, J Kondo, and A Matsumoto. Banding ahemodialysis arteriovenous fistula to decrease blood flow and resolve high output cardiac failure: report of a case. *Surg Today*, 24:734–736, 1994.

[40] MJ Sarnak. Cardiovascular complications in chronic kidney disease. *Am J Kidney Dis*, 41:11–17, 2003.

[41] C Baigent, K Burbury, and D Wheeler. Premature cardiovascular disease in chronic renal failure. *Lancet*, 356:147–152, 2000.

[42] BC Fellstrï£¡m, AG Jardine, RE Schmieder, H Holdaas, K Bannister, J Beutler, D-W Chae, A Chevaile, SM Cobbe, C Grï£¡nhagen-Riska, JJ De Lima, R Lins, G Mayer AW McMahon, H-H Parving, G Remuzzi, O Samuelsson, S Sonkodi, G Sï£¡leymanlar, D Tsakiris, V Tesar, V Todorov, A Wiecek, RP Wï£¡thrich, M Gottlow, E Johnsson, and F Zannad. Rosuvastatin and cardiovascular events in patients undergoing hemodialysis. *N Engl J Med*, 360:1395–1407, 2009.

[43] CL Wixon, JD Hughes, and JL Mills. Understanding strategies for the treatment of ischemic steal syndrome after hemodialysis access. *J Am Coll Surg*, 191:301–310, 2000.

[44] RA Mactier, WK Stewart, DM Parham, and JA Tainsh. Acral gangrene attributed to calcific azotaemic arteriopathy and the steal effect of an arteriovenous fistula. *Nephron*, 54:347–350, 1990.

[45] MK Lazarides, DN Staamos, GN Panagopoulos, VD Tzilalis, GJ Eleftheriou, and JN Dayantas. Indications for surgical treatment of angioaccess-induced arterial 'steal'. *J Am Coll Surg*, 187:422–426, 1998.

[46] P Kinnaert, J Struyven, J Mathieu, PVereerstaeten, C Toussaint, and J vanGerrstruyden. Intermittent claudication of the hand after creation of an arteriovenous fistula in the forearm. *Am J Surg*, 139:838–843, 1980.

[47] L Burrows, K Kwun, H Schanzer, and M Haimov. Hemodynamic dangers of high flow arteriovenous fistulas. *Proc Eur Dial Transplant Assoc*, 16:686–687, 1979.

[48] RC Knox, SS Berman, JD Hughes, AT Gentile, and JL Mills. Distal revascularization-interval ligation: a durable and effective treatment for ischemic steal syndrome after hemodialysis access. *J Vasc Surg*, 36:250–256, 2002.

[49] A Natï£¡rio, L Turmel-Rodrigues, M Fodil-Cherif, G Brillet, A Girault-Lataste, G Dumont, and A Mouton. Endovascular treat-

ment of immature, dysfunctional and thrombosed forearm autogenous ulnar-basilic and radial-basilic fistulas for haemodialysis. *Nephrol Dial Transplant*, 25:532–538, 2010.

[50] WA Dossert-Martin. Review of microsurgery and arteriovenous fistulae for hemodialysis. *Microsurgery*, 26:122–125, 2006.

[51] K Woo, PR Cook, J Garg, RJ Hye, and TG Canty. Midterm results of a novel technique to salvage autogenous dialysis access in aneurysmal arteriovenous fistulas. *J Vasc Surg*, 51:921–925, 2010.

[52] P Simon. *Dialyse renale*. Abreges, 1996.

[53] RR Quinn, DL Lamping, CE Lok, RA Meyer, JA Hiller, J Lee, EP Richardson, A Kiss, and MJ Oliver MJ. The vascular access questionnaire: assessing patient-reported views of vascular access. *J Vasc Access*, 9:122–128, 2008.

[54] S Najibi, RL Bush, TT Terramani, EL Chaikof, AB Gunnoud, AB Lumsden, and VJ Weiss. Covered stent exclusion of dialysis access pseudoaneurysms. *J Surg Res*, 106:15–19, 2002.

[55] AN Keeling, PA Naughton, FP McGrath, PJ Conlon, and MJ Lee. Successful endovascular treatment of a hemodialysis graft pseudoaneurysm by covered stent and direct percutaneous thrombin injection. *Semin Dial*, 21:553–556, 2008.

[56] T Lee and P Roy-Chaudhury. Advances and new frontiers in the pathophysiology of venous neointimal hyperplasia and dialysis access stenosis. *Adv Chronic Kidney Dis*, 16:329–338, 2009.

[57] U Ozyer, A Harman, E Yildirim, C Aytekin, F Karakayali, and F Boyvat. Long-term results of angioplasty and stent placement for treatment of central venous obstruction in 126 hemodialysis patients: a 10-years single-center experience. *AJR Am J Roentgenol*, 193:1672–1679, 2009.

[58] LEM Duijm, RHH van der Rijt, PWM Cuypers, AV Tielbeek, KJG Receveur, P Douwes-Draaijer, and J Buth. Outpatient treatment of arterial inflow stenoses of dysfunctional hemodialysis access fistulas by retrograde venous access puncture and catheterization. *J Vasc Surg*, 47:591–598, 2008.

[59] A R Forauer, E K Hoffer, and K Homa. Dialysis access venous stenoses: Treatment with balloon angioplasty - 1-versus 3-minute inflation times. *Radiology*, 249:375–381, 2008.

[60] YC Kim, JY Won, SY Choi, HK Ko, KH Lee, DY Lee, BC Kang, and SJ Kim. Percutaneous treatment of central venous stenosis in hemodialysis patients: long-term outcomes. *Cardiovasc Intervent Radiol*, 32:271–278, 2009.

[61] K Nael, ST Kee, H Solomon, and SG Katz. Endovascular menagement of central thoracic veno-occlusive diseases in hemodialysis patients: a single institutional experience in 69 consecutive patients. *J Vasc Interv Radiol*, 20:46–51, 2009.

[62] MR Chan, S Bedi, RJ Sanchez, HN Young, YT Becker, PS Kellerman, and AS Yevzlin. Stent placement versus angioplasty improves patency of arteriovenous grafts and blood flow of arteriovenous fistulae. *Clin J Am Soc Nephrol*, 3:699–705, 2008.

[63] M Gupta, DK Rajan, KT Tan, KW Sniderman, and ME Simons. Use of expanded polytetrafluoroethylene-covered Nitinol stents for the salvage of dysfunctional autogenous hemodialysis fistulas. *J Vasc Interv Radiol*, 19:950–954, 2008.

[64] SO Trerotola, SW Stavropoulos, R Shlansky-Goldberg, CM Tuite, S Kobrin, and MR Rudnick. Hemodialysis-related venous stenosis: treatment with ultrahigh-pressure angioplasty balloons. *Radiology*, 231:259–262, 2004.

[65] CL Zollikofer, F Antonucci, G Stuckmann, P Mattias, WF Brï£¡hlmann, and EK Salomonowitz. Use of the wallstent

in the venous system including hemodialysis-related stenoses. *Cardiovasc Intervent Radiol*, 15:334–341, 1992.

[66] MR Chan, HN Young, and AS Yevzlin. The effect of in-stent restenosis on hemodialysis access patency. *Hemodial Int*, 13:250–256, 2009.

[67] MG Chan, FJ Miller, K Valji, and MD Kuo. Evaluation of expanded polytetrafluoroethylene-covered stents for the treatment of venous outflow stenosis in hemodialysis access grafts. *J Vasc Interv Radiol*, 22:647–653, 2011.

[68] S Hatakeyama, T Toikawa, A Okamoto, H Yamamoto, K Imanishiand T Okamoto, N Tokui, Y Suzuki, N Sugiyama, A Imai, Y Hashimoto, S Kudo, T Yoneyama, T Koie, N Kamimura, H Saitoh, T Funyu, and C Ohyama. Efficacy of SMART stent placement for salvage angioplasty in hemodialysis patients with recurrent vascular access stenosis. *Int J Nephrol*, 2011:464735, 2011.

[69] P Haage, D Vorwerk, JE Wildberger, W Piroth, K Schï£¡rmann, and RW Ogden Gï£¡nther. Percutaneous treatment of thrombosed primary arteriovenous hemodialysis access fistulae. *Kidney Int*, 57:1169–1175, 2000.

[70] DD Oakes, JP Sherck, and LF Cobb. Surgical salvage of failed radiocephalic arteriovenous fistulae: techniques and results in 29 patients. *Kidney Int*, 53:480–487, 1998.

[71] R Ponikvar. Surgical salvage of thrombosed native arteriovenous fistulas for hemodialysis by interventional nephrologists. *Ther Apher Dial*, 13:340–344, 2009.

[72] A Asif. Endovascular procedures. *Contrib Nephrol*, 161:30–38, 2008.

[73] LEM Duijm, YS Liem R, van der Rijt, FJ Nobrega, HCM van der Bosch, P Douwes-Draaijer, PWM Cuypers, and AV Tielbeek. Inflow stenoses in dysfunctional hemodialysis access fistulas and grafts. *Am J Kidney Dis*, 48:98–105, 2006.

[74] A Asif, FN Gadalean, D Merrill, G Cherla, CD Cipleu, DL Epstein, and D Roth. Inflow stenosis in arteriovenous fistulas and grafts: a multicenter, prospective study. *Kidney Int*, 67:1986–1992, 2005.

[75] J Swinnen. Duplex ultrasound scanning of the autogenous arterio venous hemodialysis fistula: a vascular surgeon's perspective. *AJUM*, 14:17–23, 2011.

[76] L Salman, M Ladino, M Alex, R Dhamija, D Merrill, O Lenz, G Contreras, and A Asif. Accuracy of ultrasound in the detection of inflow stenoses of arteriovenous fistulae: results of a prospective study. *Semin Dial*, 23:117–121, 2010.

[77] CK Zarins, DP Giddens, BK Bharadvaj, VS Sottiurai, RF Mabon, and S Glagov. Carotid bifurcation atherosclerosis. Quantitative correlation of plaque localization with flow velocity profiles and wall shear stress. *Circ Res*, 53:502–514, 1983.

[78] DN Ku, DP Giddens, CK Zarins, and S Glagov. Pulsatile flow and atherosclerosis in the human carotid bifurcation. Positive correlation between plaque location and low oscillating shear stress. *Atherosclerosis*, 5:293–302, 1985.

[79] JE Jr Moore and DN Ku. Pulsatile velocity measurements in a model of the human abdominal aorta under resting conditions. *J Biomech Eng*, 116:337–346, 1994.

[80] CJ Elkins and MT Alley. Magnetic resonance velocimetry: applications of magnetic resonance imaging in the measurement of fluid motion. *Exp Fluids*, 43:823–858, 2007.

[81] S Ahn, D Shin, S Tateshima, K Tanishita, F Vinuela, and S Sinha. Fluid-induced wall shear stress in anthropomorphic brain aneurysm models: MR phase-contrast study at 3 T. *J Magn Reson Imaging*, 25:1120–1130, 2007.

[82] RD Keane and RJ Adrian. Theory of cross-correlation analysis of PIV images. *Applied Scientific Research*, 49:191–215, 1992.

[83] A-V Salsac. *Evolution des contraintes hemodynamiques lors de la croissance des anevrismes aortiques abdominaux*. PhD thesis, Ecole Politechnique, 2005.

[84] MD Ford, HN Nikolov, JS Milner, SP Lownie, EM Demont, W Kalata, F Loth, DW Holdsworth, and CA Steinman. PIV-measured versus CFD-predicted flow dynamics in anatomically realistic cerebral aneurysm models. *J Biomech Eng*, 130:021015, 2008.

[85] Y Hoi, SH Woodward, M Kim, DB Taulbee, and H Meng. Validation of CFD simulations of cerebral aneurysms with implication of geometric variations. *J Biomech Eng*, 128:844–851, 2006.

[86] J Seong, AK Wakhloo, and BB Lieber. In vitro evaluation of flow divertors in an elastase-induced saccular aneurysm model in rabbit. *J Biomech Eng*, 129:863–872, 2007.

[87] HB Kim, J Hertzberg, C Lanning, and R Shandas. Noninvasive measurement of steady and pulsating velocity profiles and shear rates in arteries using echo PIV: in vitro validation studies. *Ann Biomed Eng*, 32:1067–1076, 2004.

[88] J Charonko, S Karri, J Schmieg, S Prabhu, and P Vlachos. In vitro, time-resolved PIV comparison of the effect of stent design on wall shear stress. *Ann Biomed Eng*, 37:1310–1321, 2009.

[89] J Charonko, S Karri, J Schmieg, S Prabhu, and P Vlachos. In vitro comparison of the effect of stent configuration on wall shear stress using time-resolved particle image velocimetry. *Ann Biomed Eng*, 38:889–902, 2010.

[90] CN Ionita, Y Hoi, H Meng, and S Rudin. Particle image velocimetry (PIV) evaluation of flow modification in aneurysm phantoms using asymmetric stents. *Proc Soc Opt Instrum Eng*, 5329:295, 2004.

[91] C Guivier-Curien, V Deplano, and E Bertrand. Validation of a numerical 3-D fluid-structure interaction model for a prosthetic valve based on experimental PIV measurements. *Med Eng Phys*, 31:986–993, 2009.

[92] A Lï£¡pez-Zazueta, R Ledesma-Alonso, JE Guzman, and R Zenit. Study of the velocity and strain fields in the flow through prosthetic heart valves. *J Biomech Eng*, 133:121003, 2011.

[93] T Akutsu and A Matsumoto. Influence of three mechanical bileaflet prosthetic valve designs on the three-dimensional flow field inside a simulated aorta. *J Artif Organs*, 13:207–2017, 2010.

[94] B-K Lee. Computational fluid dynamics in cardiovascular disease. *Korean Circ J*, 41:423–430, 2011.

[95] K Govindaraju, IA Badruddin, GN Viswanathan, SV Ramesh, and A Badarudin. Evaluation of functional severity of coronary artery disease and fluid dynamics' influence on hemodynamic parameters: A review. *Phys Med*, Epub ahead of print, 2012.

[96] LD Jou, HM Shaltoni, H Morsi, and ME Mawad ME. Hemodynamic relationship between intracranial aneurysm and carotid stenosis: review of clinical cases and numerical analyses. *Neurol Res*, 32:1083–1089, 2010.

[97] PR Hoskins and D Hardman. Three-dimensional imaging and computational modelling for estimation of wall stresses in arteries. *Br J Radiol*, 82 Spec No 1:S3–S17, 2009.

[98] KH Fraser, ME Taskin, BP Griffith, and ZJ Wu. The use of computational fluid dynamics in the development of ventricular assist devices. *Med Eng Phys*, 33:263–280, 2011.

[99] R Hose and MM Black. Prosthetic heart valves-the integration of analysis with design. *J Heart Valve Dis*, 4 Suppl 1:S50–S54, 1995.

[100] L Punnoose, D Burkhoff, S Rich, and EM Horn. Right ventricular assist device in end-stage pulmonary arterial hypertension: insights

from a computational model of the cardiovascular system. *Prog Cardiovasc Dis*, 55:234–243, 2012.

[101] Y Qiu and JM Tarbell. Numerical simulation of pulsatile flow in a compliant curved tube model of coronary artery. *J Biomed Eng*, 122:77–85, 2000.

[102] SD Ramaswamy, SC Vigmostad, A Wahle, YG Lai, ME Olszewski, KC Braddy, TM Brennan, JD Rossen, M Sonka, and KB Chandran. Fluid dynamic analysis in a human left anterior descending coronary artery with arterial motion. *Ann Biomed Eng*, 32:1628–1641, 2004.

[103] GD Giannoglou, JV Soulis, TM Farmakis, GA Giannakoulas, GE Parcharidis, and GE Louridas. Wall pressure gradient in normal left coronary artery tree. *Med Eng Phys*, 27:455–464, 2005.

[104] JF Jr LaDisa, LE Olson, HA Douglas, DO Warltier, JR Kersten, and PS Pagel. Alterations in regional vascular geometry produced by theoretical stent implantation influence distributions of wall shear stress: an-alysis of a curved coronary artery using 3D computational fluid dynamics modeling. *Biomed Eng Online*, 16:40, 2006.

[105] MI Papafaklis, CV Bourantas, PE Theodorakis, CS Katsouras, DI Fotiadis, and LK Michalis. Association of endothelial shear stress with plaque thickness in a real three-dimensional left main coronary artery bifurcation model. *Int J Cardiol*, 115:276–278, 2007.

[106] BK Lee, JY Lee, BK Hong, BE Park, DS Kim, DY Kim, YH Cho, SJ Yoon, YW Yoonand HM Kwon, HW Roh, I Kim, HW Park, SM Han, MT Cho, SH Suh, and HS Kim. Hemodynamic analysis of coronary circulation in angulated coronary stenosis following stenting. *Yonsei Med J*, 43:590–600, 2002.

[107] SD Ramaswamy, SC Vigmostad, A Wahle, YG Lai, ME Olszewski, KC Braddy, TM Brennan, JD Rossen, M Sonka, and KB Chandran. Comparison of left anterior descending coronary artery hemodynamics before and after angioplasty. *J Biomech Eng*, 128:40–48, 2006.

[108] M Sankaranarayanan, LP Chua, DN Ghista, and YS Tan. Computational model of blood flow in the aorto-coronary bypass graft. *Biomed Eng Online*, 4:14, 2005.

[109] SW Lee, L Antiga, JD Spence, and DA Steinman. Geometry of the carotid bifurcation predicts its exposure to disturbed flow. *Stroke*, 39:2341–2347, 2008.

[110] SE Lee, SW Lee, PF Fischer, HS Bassiouny, and F Loth. Direct numerical simulation of transitional flow in a stenosed carotid bifurcation. *J Biomech*, 41:2251–2261, 2008.

[111] XJ Xue, PY Gao, Q Duan, Y Lin, and CB Dai. Preliminary study of hemodynamic distribution in patient-specific stenotic carotid bifurcation by image-based computational fluid dynamics. *Acta Radiol*, 49:558–565, 2009.

[112] S Morlacchi and F Migliavacca. Modeling stented coronary arteries: Where we are, where to go. *Ann Biomed Eng*, page [Epub ahead of print], 2012.

[113] T Frauenfelder, M Lotfey, T Boehm, and S Wildermuth. Computational fluid dynamics: hemodynamic changes in abdominal aortic aneurysm after stent-graft implantation. *Cardiovasc Intervent Radiol*, 29:613–623, 2006.

[114] E Boutsianis, M Guala, U Olgac, S Wildermuth, K Hoyer, Y Ventikos, and D Poulikakos. CFD and PTV steady flow investigation in an anatomically accurate abdominal aortic aneurysm. *J Biomech Eng*, 131:011008, 2009.

[115] KM Tseand, P Chiu, HP Lee, and P Ho. Investigation of hemodynamics in the development of dissecting aneurysm within patient-specific dissecting aneurismal aortas using computational fluid dynamics (CFD) simulations. *J Biomech*, 44:827–836, 2011.

[116] JR Cebral, F Mut, J Weir, and C Putman. Quantitative characterization of the hemodynamic environment in ruptured and unruptured brain aneurysms. *AJNR Am J Neuroradiol*, 32:145–151, 2011.

[117] S Omodaka, S Sugiyama, T Inoue, K Funamoto, M Fujimura, H Shimizu, T Hayase, A Takahashi, and T Tominaga. Local hemodynamics at the rupture point of cerebral aneurysms determined by computational fluid dynamics analysis. *Cerebrovasc Dis*, 34:121–129, 2012.

[118] S Omodaka, T Inoue, K Funamoto, S Sugiyama, H Shimizu, T Hayase, A Takahashi, and T Tominaga. Influence of surface model extraction parameter on computational fluid dynamics modeling of cerebral aneurysms. *J Biomech*, 45:2355–2361, 2012.

[119] JJ Schneiders, HA Marquering, L Antiga, R van den Berg, E Vanbavel, and CB Majoie. Intracranial aneurysm neck size overestimation with 3D rotational angiography: The impact on intra-aneurysmal hemodynamics simulated with computational fluid dynamics. *AJNR Am J Neuroradiol*, 2012.

[120] EL Bove, MR de Leval, F Magliavacca, G Guadagni, and G Dubini. Computational fluid dynamics in the evaluation of hemodynamic performance of cavopulmonary connections after the Norwood procedure for hypoplastic left heart syndrome. *J Thorac Cardiovasc Surg*, 126:1040–1047, 2003.

[121] S Pittaccio, F Migliavacca, G Dubini, E Koï£¡yildirim, and MR de Leval MR. On the use of computational models for the quantitative assessment of surgery in congenital heart disease. *Anadolu Kardiyol Derg*, 5:202–209, 2005.

[122] A Hager, S Fratz, M Schwaiger, R Lange, J Hess, and H Stern. Pulmonary blood flow patterns in patients with Fontan circulation. *Ann Thorac Surg*, 85:186–191, 2008.

[123] AF Corno, C Vergara, C Subramanian, RA Johnson, T Passerini, A Veneziani, L Formaggia, N Alphonso, A Quarteroni, and JC Jarvis. Assisted Fontan procedure: animal and in vitro models and computational fluid dynamics study. *Interact Cardiovasc Thorac Surg*, 10:679–684, 2010.

[124] Y Qian, JL Liu, K Itatani, K Miyaji, and M Umezu. Computational hemodynamic analysis in congenital heart disease: Simulation of the Norwood procedure. *Ann Biomed Eng*, 38:2302–2313, 2010.

[125] K Perktold and G Rappitsch. Computer simulation of local blood flow and vessel mechanics in a compliant carotid artery bifurcation model. *J Biomech*, 28:845–856, 1995.

[126] J-F Gerbeau, M Vidrascu, and P Frey. Fluid structure interaction in blood flow on geometries based on medical images. *Comput Struct*, 83:155–165, 2005.

[127] Y Bazilevs, VM Calo, Y Zhang, and TJR Hughes. Isogeometric fluid-structure interaction analysis with applications to arterial blood flow. *Comput Mech*, 38:310–322, 2006.

[128] B Wolters, MCM Rutten, GWH Schurink, U Kose, J deHart, and FN van de Vosse. A patient-specific computational model of fluid-structure interactions in abdominal aortic aneurysm. *Med Eng Phys*, 27:871–883, 2005.

[129] CS Peskin. The immersed boundary method. *Acta Numer*, 11:479–517, 2002.

[130] JD Lemmon and AP Yoganathan. Computational modeling of left hearth diastolic function: examination of ventricular dysfunction. *J Biomech Eng*, 122:297–303, 2000.

[131] PN Watton, XY Luo, X Wang, GM Bernacca, P Molloy, and DJ Wheatley. Dynamic modelling of prosthetic chorded mitral valves using the immersed boundary method. *J Biomech*, 40:613–626, 2007.

[132] CS Peskin. The immersed boundary method. *Acta Numer*, 11:479–517, 2003.

[133] R Glowinski, TW Pan, and J Periaux. A Lagrange multiplier/fictious domain method for the numerical simulation of incompressible viscous flow around moving rigid bodies: (I) case where the rigid body motion are known a priori. *C R Acad Sci Ser I Math*, 324:361–369, 1997.

[134] J DeHart, GWM Peters, PJG Schreurs, and FPT Baaijens. A three-dimensional computational analysis of fluid-structure interaction in the aorticvalve. *J Biomech*, 36:103–112, 2003.

[135] J DeHart, GWM Peters, PJG Schreurs, and FPT Baaijens. Collagen fibers reduce stresses and stabilize motion of aorticvalve leaflets during systole. *J Biomech*, 37:303–311, 2004.

[136] TE Tezduyar, M Behr, and S Mittal. A new strategy for finite element computations involving moving boundaries and interfaces - the deforming-spatial-domain/space-time procedure: II. Computation of free-surface flows, two-liquid flows, and flows with drifting cylinders. *Comput Meth Appl Mech Eng*, 94:353–371, 1992.

[137] R Torii, M Oshima, T Kobayashi, K Takagi, and TE Tezduyar. Computer modeling of cardiovascular fluid-structure interactions with the deforming-spatial-domain/stabilized space-time formulation. *Comput Methods Appl Mech Eng*, 195:1885–1895, 2006.

[138] R Torii, NB Wood, N Hadjiloizou, AW Dowsey, AR Wright, AD Hughes, J Davies, DP Francis, J Mayet, GZ Yang, SA McG Thom, and XY Xu. Fluidï£¡structure interaction analysis of a patient-specific right coronary artery with physiological velocity and pressure waveforms. *Int j numer method biomed eng*, 25:565–580, 2009.

[139] CA Figueroa, IE Vignon-Clementel, KE Jansen, TJR Hughes, and CA Taylor. A coupled momentum method for modeling blood flow in three-dimensional deformable arteries. *Comput Meth Appl Mech Eng*, 195:5685–5706, 2006.

[140] IE Vignon-Clementel, CA Figueroa, KE Jansen, and CA Taylor. Outflow boundary conditions for three-dimensional finite element modeling of blood flow and pressure in arteries. *Comput Met*, 195:3776–3796, 2006.

[141] HJ Kim, CA Figueroa, TJR Hughes, KE Jansen, and CA Taylor. Augmented lagrangian method for constraining the shape of velocity profiles at outlet boundaries for three-dimensional finite element simulations of blood flow. *Comput Methods Appl Mech Eng*, 198:3551–3566, 2009.

[142] GA Holzapfel, CAJ Schulze-Bauer, and M Stadler. Mechanics of angioplasty: wall, balloon and stent. *Mech in Biology*, 242:141–156, 2000.

[143] GA Holzapfel, TC Gasser, and M Stadler. A structural model for the viscoelastic behavior of arterial walls: Continuum formulation and finite element analysis. *European Journal of Mechanics - A/Solids*, 21:441–463, 2002.

[144] GA Holzapfel, TC Gasser, and RW Ogden. Comparison of a multi-layer structural model for arterial walls with a fung-type model, and issues of material stability. *J Biomech Eng*, 126:264–275, 2004.

[145] GA Holzapfel and TC Gasser. Computational stress-deformation analysis of arterial walls including high-pressure response. *Int J Cardiol*, 116:78–85, 2007.

[146] TC Gasser and GA Holzapfel. Finite element modeling of balloon angioplasty by considering overstretch of remnant non-diseased tissues in lesions. *Comput Mech*, 40:47–60, 2007.

[147] DE Kiousis, TC Gasser, and GA Holzapfel. Changes in the mechanical environment of lesions due to stent-artery interaction–a computational analysis. *J Biomech*, 39:S403–S403, 2006.

[148] DE Kiousis, AR Wulff, and GA Holzapfel. Experimental studies and

numerical analysis of the inflation and interaction of vascular balloon catheter-stent systems. *Ann Biomed Eng*, 37:315–320, 2009.

[149] F Gervaso, C Capelli, L Petrini, S Lattanzio, L Di Virgilio, and F Migliavacca. On the effects of different strategies in modelling balloon-expandable stenting by means of finite element method. *J Biomech*, 41:1206–1212, 2008.

[150] C Capelli, F Gervaso, L Petrini, G Dubini, and F Migliavacca. Assessment of tissue prolapse after balloon-expandable stenting: Influence of stent cell geometry. *Med Eng Phys*, 31:441–447, 2009.

[151] C Chiastra, S Morlacchi, S Pereira, G Dubini, and F Migliavacca. Computational fluid dynamics of stented coronary bifurcations studied with a hybrid discretization method. *Eur J Mech B Fluids*, page article in press, 2012.

[152] TJ Gundert, AL Marsden, W Yang, and JF Jr LaDisa. Optimization of cardiovascular stent design using computational fluid dynamics. *J Biomech Eng*, 134:011002, 2012.

[153] DS Molony, A Callanan, EG Kavanagh, MT Walsh, and TM McGloughlin. Fluid-structure interaction of a patient-specific abdominal aortic aneurysm treated with an endovascular stent-graft. *Biomed Eng Online*, 6:8–24, 2009.

[154] AR Williams, B-K Koo, TJ Gundert, PJ Fitzgerald, and JF LaDisa Jr. Local hemodynamic changes caused by main branch stent implantation and subsequent virtual side branch balloon angioplasty in a representative coronary bifurcation. *J Appl Physiol*, 109:532–540, 2010.

[155] H Hayase, K Tokunaga, T Nakayama, K Sugiu, A Nishida, S Arimitsu, T Hishikawa, S Ono, M Ohta, and I Date. Computational fluid dynamics of carotid arteries after carotid endarterectomy or carotid artery stenting based on postoperative patient-specific computed tomography angiography and ultrasound flow data. *Neurosurgery*, 68:1096–1101, 2011.

[156] W Huberts, AS Bode, W Kroon, RN Planken, JHM Tordoir, and FN van de Vosse. A pulse wave propagation model tu support decision-making in vascular access planning in the clinic. *Med Eng Phys*, 34:233–248, 2012.

[157] D Bessems, CG Giannopapa, MCM Rutten, and FN van de Vosse. Experimental validation of a time-domain-based wave propagation model of blood flow in viscoelastic vessels. *J Biomech*, 41:284–291, 2008.

[158] M Ojha, CR Ethier, KW Johnston, and RSC Cobbold. Steady and pulsatile flow fields in an end-to-side arterial anastomosis model. *J Vasc Surg*, 12:747–753, 1990.

[159] RS Keynton, SE Rittgers, and MCS Shu. The effect of angle and flow rate upon hemodynamics in distal vascular graft anastomoses: an in vitro model study. *ASME J Biomech Eng*, 133:458–463, 1991.

[160] M Hofer, G Rappitsch, K Perktold, and W Trubel ansd H Schima. Numerical study of wall mechanics and fluid dynamics in end-to-side anastomoses and correlation to intima hyperplasia. *J Biomech*, 29:1297–1308, 1996.

[161] PE Hughes and TV How. Effects of geometry and flow division on flow structures in models of the distal end-to-side anastomosis. *J Biomech*, 29:855–872, 1996.

[162] CR Ethier, DA Steinman, X Zang, SR Karpik, and M Ojha. Flow waveform effects on end-to-side anastomotic flow patterns. *J Biomech*, 31:609–617, 1998.

[163] XM Li and SE Rittgers. Hemodynamic factors at the distal end-to-side anastomosis of a bypass graft with different POS:DOS flow ratios. *J Biomech Eng*, 123:270–276, 2001.

[164] M Jackson, NB Wood, S Zhao, A Augst, JH Wolfe, , WMW Gedroyc, AD Hughes, SAMcG Thom, and XY Xu. Low wall shear stress pre-

dicts subsequent development of wall hypertrophy in lower limb bypass grafts. *Artery Research*, 3:32–38, 2009.

[165] Z Kharboutly, V Deplano, E Bertrand, and C Legallais. Numerical and experimental study of blood flow through a patient-specific arteriovenous fistula used for hemodialysis. *Med Eng Phys*, 32:111–118, 2010.

[166] B Ene-Iordache, L Mosconi, G Remuzzi, and A Remuzzi. Computational fluid dynamics of a vascular access case for hemodialysis. *J Biomech Eng*, 123:284–292, 2001.

[167] I vanTricht, D De Wachter, J Tordoir, and P Verdonck. Comparison of the hemodynamics in 6mm and 4-7 mm hemodialysis grafts by means of CFD. *J Biomech*, 39:226–236, 2006.

[168] K van Canneyt, T Pourchez, S Eloot, C Guillame, A Bonnet, P Segers, and P Verdonck. Hemodynamic impact of anastomosis size and angle in side-to-end arteriovenous fistulae: a computer analysis. *J Vasc Access*, 11:52–58, 2010.

[169] Z Kharboutly, JM Treutenaere, I Claude, and C Legallais. Arteriovenous fistula: two cases realistic numerical blood flow simulations. In *Conf Proc IEEE Eng Med Biol Soc*, 2007.

[170] Z Kharboutly, M Fenech, JM Treutenaere, I Claude, and C Legallais. Investigations into the relationship between hemodynamics and vascular alterations in an established arteriovenous fistula. *Med Eng Phys*, 29:999–1007, 2007.

[171] AK Niemann, S Thrysoe, JV Nygaard, JM Hasenkam, and SE Petersen. Computational fluid dynamics simulation of a-v fistulas: From MRI and ultrasound scans to numeric evaluation of hemodynamics. *J Vasc Access*, 24:ahead of print, 2011.

[172] K van Canneyt, RN Planken, S Eloot, P Segers, and P Verdonck. Experimental study of a new method for early detection of vascular

access stenoses: pulse pressure analysis at hemodialysis needle. *Artif Organs*, 34:113–117, 2010.

[173] *ANSYS Academic Research, Release 13.0, Help System, Advice on flow modelling, time-step controls*. ANSYS, Inc., 2010.

[174] CM Rhie and WL Chow. Numerical study of the turbulent flow past an airfoil with trailing edge separation. *AIAA Journal*, 21:1525–1532, 1983.

[175] EW Merril and GA Pelletier. Viscosity of human blood: transition from Newtonian to non-Newtonian. *J Appl Physiol*, 23:178–182, 1967.

[176] F Kabinejadian and DN Ghista. Compliant model of a coupled sequential coronary arterial bypass graft: Effects of vessel wall elasticity and non-newtonian rheology on blood flow regime and hemodynamic parameters distribution. *Med Eng Phys*, 34:860–872, 2011.

[177] N Westerhof, F Bosman, CJ De Vries, and A Noordergraaf. Analog studies of the human systemic arterial tree. *J Biomech*, 2:121–143, 1969.

[178] P Molino, C Cerutti, C Julien, G Cusinaud, MP Gustin, and C Paultre. Beat-to-beat estimation of windkessel model parameters in conscious rats. *Am J Physiol Heart Circ Physiol*, 274:H171–H177, 1998.

[179] LWJ Bogert and JJ vanLieshout. Non-invasive pulsatile arterial pressure and stroke volume changes from the human finger. *Exp Physiol*, 90:437–448, 2005.

[180] M Ismail, WA Wall, and MW Gee. djoint-based inverse analysis of windkessel parameters for patient-specific vascular models. *J Comp Phys*, in press, 2012.

[181] JJ Chiu and S Chien. Effects of disturbed flow on vascular endothelium: pathophysiological basis and clinical perspectives. *Physiol Rev*, 91:327–387, 2011.

[182] OH Yeoh. Some forms of the strain energy function for rubber. *Rubber Chem Technol*, 66:754–771, 1993.

[183] KC McGilvray, R Sarkar, K Nguyen, and CM Puttlitz. A biomechanical analysis of venous tissue in its normal and post-phlebitic conditions. *J Biomech*, 43:2941–2947, 2010.

[184] PJ Prendergast, C Lally, S Daly, A J Reid, TC Lee, D Quinn, and F Dolan. Analysis of prolapse in cardiovascular stents: a constitutive equation for vascular tissue and finite-element modelling. *J Biomech Eng*, 125:692–699, 2003.

[185] E Maher, A Creane, S Sultan, N Hynes, C Lally, and DJ Kelly. Inelasticity of human carotid atherosclerotic plaque. *Ann Biomed Eng*, 39:2445–2455, 2011.

[186] KT Christensen, SM Soloff, and RJ Adrian. PIV sleuth: Integrated particle image velocimetry (PIV) interrogation/validation software. Technical report, Technical Report 943, Department of Theoretical and Applied Mechanics, University of Illinois at Urbana-Champaign, 2000.

[187] *LaVision FlowMaster 7.0 Product-Manual (LaVision GMBH.; Goettingen, Germany).*

[188] M Allon and ML Robbin. Increasing arteriovenous fistulas in hemodialysis patients: problems and solutions. *Kidney Int*, 62:1109–1124, 2002.

[189] K Kian and J A Vassalotti. The new arteriovenous fistula: the need for earlier evaluation and intervention. *Semin Dial*, 18:3–7, 2005.

[190] M Wan, X Gong, and M Qian. In vivo hemodynamic evaluation based on transverse doppler measurements of blood velocities and vessel diameter. *IEEE Trans Biomed Eng*, 46:1074–1080, 1999.

[191] J Chen, S Wang, G Ding, X Yang, and H Li. The effect of aneurismal-wall mechanical properties on patient-specific hemodynamic simulations- two clinical case reports. *Acta Mech Sin*, 25:677–688, 2009.

[192] YH Kim, JE Kim, Y Ito, AM Shih, B Brott, and A Anayiotos. Hemodynamic analysis of a compliant femoral artery bifurcation model using a fluid structure interaction framework. *Ann Biomed Eng*, 36:1753–1763, 2008.

[193] Z Li and C Kleinstreuer. Fluid-structure interaction effects on sac-blood pressure and wall stress in a stented aneurysm. *J Biomech Eng*, 127:662–671, 2005.

[194] D Tang, C Yang, S Kobayashi, J Zheng, P K Woodard, Z Teng, K Billiar, R Bach, and DN Ku. 3D MRI-based anisotropic FSI models with cyclic bending for human coronary atherosclerotic plaque mechanical analysis. *J Biomech Eng*, 131:061010, 2009.

[195] TE Tezduyar, S Sathe, M Schwaab, and BS Conklin. Arterial fluid mechanics modeling with the stabilized spaceï£¡time fluidï£¡structure interaction technique. *Int J Numer Meth Fluids*, 57:601–629, 2008.

[196] D Tang, C Yang, S Mondal, F Liu, G Canton, TS Hatsukami, and C Yuan. A negative correlation between human carotid atherosclerotic plaque progression and plaque wall stress: In vivo MRI-based 2D/3D FSI models. *J Biomech*, 41:727–736, 2008.

[197] CA Taylor and CA Figueroa. Patient-specific modeling of cardiovascular mechanics. *Annu Rev Biomed Eng*, 11:109–134, 2009.

[198] G Xiong, CA Figueroa, N Xiao, and CA Taylor. Simulation of blood flow in deformable vessels using subject-specific geometry and spatially varying wall properties. *Int J Numer Method Biomed Eng*, 27:1000–1016, 2011.

[199] J F Rodrï£¡guez, C Ruiz, M Doblarï£¡, and G A Holzapfel. Mechanical stresses in abdominal aortic aneurysms: influence of diameter, asymmetry, and material anisotropy. *J Biomech Eng*, 2:021023, 2009.

[200] MA Gutierrez, PE Pilon, SG Lage, L Kopel, RT Carvalho, and SS Fu-

ruie. Automatic measurement of carotid diameter and wall thickness in ultrasound images. *Comput Cardiol*, 29:359–362, 2002.

[201] I Decorato, A-V Salsac, C Legallais, M Ali-Mohammadi, V Diaz-Zuccarini, and Z Kharboutly. Numerical simulation of the treatment of an arterial stenosis in an arteriovenous fistula by balloon-angioplasty. *CVET*, [submitted], 2012.

[202] JR Womersley. Method for the calculation of velocity, rate of flow and viscous drag in arteries when the pressure gradient is known. *J Physiol*, 28:553–563, 1955.

[203] M Ojha. Wall shear stress temporal gradient and anastomotic intimal hyperplasia. *Circ Res*, 74:1227–1231, 1994.

[204] M Markl, F Wegent, T Zech, S Bauer, C Strecker, M Schumacher, C Weiller, J Hennig, and A Harloff. In vivo wall shear stress distribution in the carotid artery: effect of bifurcation geometry, internal carotid artery stenosis, and recanalization therapy. *Circ Cardiovasc Imaging*, 3:647–655, 2010.

[205] A Rachev. Theoretical study of the effect of stress-dependent remodeling on arterial geometry under hypertensive conditions. *J Biomech*, 30:819–827, 1997.

[206] S Glagov, CK Zarins, N Masawa, CP Xu, H Bassiouny, and DP Giddens. Mechanical functional role of non-atherosclerotic intimal thickening. *Front Med Biol Eng*, 5:37–43, 1993.

[207] P Fridez, M Zulliger, F Bobard, G Montorzi, H Miyazaki, K Hayashi, and N Stergiopulos. Geometrical, functional, and histomorphometric adaptation of rat carotid artery in induced hypertension. *J Biomech*, 36:671–680, 2003.

[208] A Rachev, N Stergiopulos, and J-J Meister. Theoretical study of dynamics of arterial wall remodeling in response to changes in blood pressure. *J Biomech*, 29:635–642, 1996.

[209] LA Martinez-Lemus, MA Hill, and GA Meininger. The plastic nature of the vascular wall: a continuum of remodeling events contributing to control of arteriolar diameter and structure. *Physiology*, 24:45–57, 2009.

[210] EP Kritharis, JD Kakisis, AT Giagini, T Manos, N Stergiopulos, S Tsangaris, and DP Sokolis. Biomechanical, morphological and zero-stress state characterization of jugular vein remodeling in arteriovenous fistulas for hemodialysis. *Biorheology*, 47:297–319, 2010.

[211] C Butler and NL Tilney. *Replacement of Renal Function by Dialysis. Section II: Hemodialysis Access Part B - Permanent.* Kluwer Academic Publishers, 1996.

[212] PK Singh, A Marzo, C Staicu, MG William, I Wilkinson, PV Lawford, DA Rufenacht, P Bijlenga, AF Frangi, R Hose, UJ Patel, and SC Coley. The effects of aortic coarctation on cerebral hemodynamics and its importance in the etiopathogenesis of intracranial aneurysms. *J Vasc Int Neurol*, 3:17–30, 2010.

[213] DF Young. Fluid mechanics of arterial stenoses. *J Biomech Eng*, 101:157175, 1979.

[214] J Braun, M Oldendorf, W Moshage, R Heidler, E Zeitler, and FC Luft. Electron beam computed tomography in the evaluation of cardiac calcifications in chronic dialysis patients. *Am J Kidney Dis*, 27:394–401, 1996.

[215] V Perkovic, D Hunt, SV Griffin, M du Plessis, and GJ Becker. Accelerated progression of calcific aortic stenosis in dialysis patients. *Nephron Clin Pract*, 94:c40–c45, 2003.

[216] I Decorato, Z Kharboutly, C Legallais, J Penrose, and A-V Salsac. Numerical simulation of the fluid structure interactions in a compliant patient-specific arteriovenous fistula. *Int J Num Meth Biomed Eng*, 2012.

[217] TW Duerig and M Wholey. A comparison of balloon- and self-expanding stents. *Min Invas Ther & Allied Technol*, 11:173–178, 2002.

[218] H Vernhet, J-M Juan, R Demaria, M-C Oliva-Laurairea, J-P Senac, and M Dauzat. Acute changes in aortic wall mechanical properties after stent placement in rabbits. *J Vasc Int Rad*, 11:634–638, 2000.

[219] C Rogers, DY Tseng, JC Squire, and ER Edelman. Balloon-artery interactions during stent placement: a finite element analysis approach to pressure, compliance, and stent design as contributors to vascular injury. *Circ Res*, 84:378–383, 1999.

[220] M DeBeule. *Finite element stent design*. PhD thesis, Ghent University, 2008.